NTNU – Trondheim
Norwegian University of
Science and Technology

Pd-based Membranes for Hydrogen Separation - Membrane Structure and Hydrogen Sorption and Permeation Behavior

Live Nova Næss

Abstract

Efficient separation of hydrogen from gas mixtures is a truly enabling technology for hydrogen as an energy carrier. Palladium(Pd)-based membranes are 100% selective to hydrogen, but need to be made thin, yet without defects in order for the technology to be applicable. The motivation for this work has been to examine solubility properties and surface topography for Pd-based membranes, and further elucidate the influence these parameters have on the overall hydrogen permeation capabilities. Extremely thin, defect-free Pd-alloy membranes supplied by SINTEF Materials and Chemistry were investigated in this study.

Thin Pd/Ag23wt.% free standing films of thickness 4 μm and 8 μm were investigated before and after heat treatment in air at 300 °C. A revealing trend of increased flux resulting from this heat treatment was observed. Surface topography studies by atomic force microscopy (AFM) showed a correlating increase in surface roughness as a result of the heat treatment. In addition, surface topography investigation was performed on a hydrogen stabilized 8 μm thick Pd/Ag23wt.% membrane. High increase in roughness was detected on feed side whereas minimal roughness alteration was observed on permeate side of the membrane.

Equilibrium sorption measurements of H_2 in Pd/Ag23wt.% films of various thicknesses (2.2-10 μm) were performed at 300 °C, 350 °C and 400 °C to the measure the film's solubility properties. A pronounced temperature dependence was observed for all membranes, that is, high solubility at low temperatures and vice versa for high temperatures. This is consistent with theory and previously reported solubility results. A thickness dependence for the H_2 solubility was observed in the equilibrium sorption results. Thinner membranes showed better solubility capabilities than the thicker ones. Surface characterization showed increasing surface roughness on growth side on these as-grown films in correspondence with augmentation in film thickness. The correlative surface roughness and solubility alterations related to thickness indicate a plausible membrane bulk structural dependence of the solubility.

Finally, sorption equilibrium measurements on very thin Pd alloy films, ∼2 μm, of Pd/Ag23wt.%, Pd/Au5at.% and Pd/Y5at.% were carried out at 300 °C, 350 °C and 400 °C. All three palladium-alloys showed decreasing solubility properties for increasing temperature. The Pd/Ag23wt.% membrane showed the highest solubility capabilities, succeeded closely by the Pd/Y5at.% membrane, while the Pd/Au5at.% membrane was not comparably capable to ad-/absorb H_2 gas. This is concluded as a result of unequal lattice expansion effects the different alloying elements exert in a pure Pd lattice.

The hydrogen permeation is a complex function of many parameters. In this work parameters such as, hydrogen pressure, temperature, material composition, membrane thickness and surface structure have demonstrated their influence on the membranes solubility and/or permeation abilities.

Sammendrag

Effektiv separasjon av ren hydrogen fra en gassblanding er en teknologi som baner vei i utviklingen av hydrogen som en energibærer. Palladium(Pd)baserte membraner er 100% selektive for hydrogen, men må lages tynne og uten defekter for at teknologien skal være anvendbar. Motivasjonen bak dette arbeidet har vært å undersøke løselighetsegenskaper og overflatetopografi av Pd-baserte membraner, og videre belyse innvirkningen disse parameterene har på hydrogenpermeasjonsevnene til membranen. Ekstremt tynne, defektfrie Pd-legeringsmembraner levert av SINTEF Materialer og Kjemi ble undersøkt i dette arbeidet.

Tynne Pd/Ag23wt.% frittstående filmer av tykkelse 4 μm og 8 μm undersøkt før og etter varmebehandling i luft ved 300 °C. Det ble observert en klar trend på økt fluks som resultat av denne varmebehandlingen. Undersøkelser av overflatetopografi med atomær kraft mikroskopi (AFM) viste en korrelerende økning i overflateruhet som et resultat av varmebehandlingen. En sådan undersøkelse ble i tillegg utført på en 8 μm tykk Pd/Ag23wt.% membran som hadde blitt stabilisert ved hydrogenpermeasjon. Denne membranen viste økt ruhet på "feed"-siden mens minimal endring i ruhet ble observert på "permeate"-siden av membranen.

Likevektsorpsjonsmålinger av H_2 i Pd/Ag23wt.% filmer av ulike tykkelser (2.2-10 μm) ble utført ved 300 °C, 350 °C og 400 °C for å måle løselighetsegenskapene til filmen. En tydelig temperaturavhengighet ble observert for alle membranene. Den viste høy løselighet ved lave temperaturer og motsatt ved høye temperaturer. Disse funn stemmer overens med tidligere rapporterte løselighetshypoteser og resultat.

En tykkelseavhengighet for løselighet av H_2 ble observert i resultatene av likevektsorpsjonsmålinger. Tynnere membraner viste bedre løselighetsevner enn tykke membraner. Overflatekarakteristikk viste økende ruhet på overflaten som funksjon av membrantykkelse. Samsvarende endringene av ruhet på membranoverflaten og løselighet relatert til tykkelse, indikerer en plausibel membranstrukturavhengighet for løselighet.

Likevektsorpsjonsmålinger av H_2 i svært tynne Pd-basertefilmer, $\sim$2 μm, Pd/Ag23wt.%, Pd/Au5at.% og Pd/Y5at.% ble gjennomført ved 300 °C, 350 °C og 400 °C. Alle de Pd-legeringsmembranene viste synkende løselighetsegenskaper ved økende temperatur. Pd/Ag23wt.% membranen hadde best løselighetsevner tett påfulgt av Pd/Y5at.%, mens Pd/Au5at.% membranen ikke var i stand til å ad-/absorbere hydrogen i sammenlignbare mengder. Dette kommer trolig av ulik gitterutvidelse legeringselementene påfører et rent Pd-gitter.

Preface

This Master's thesis is submitted as the final part of the Master of Science Degree in Applied Physics and Mathematics (MTFYMA) at the Norwegian University of Science and Technology (NTNU). The thesis gives 30 credits and is a part of the Applied Physics specialization Programme in Department of Physics, NTNU, Trondheim. It is the result of scientific work carried out over 20 weeks and completed in January 2013.

The experimental works presented in this thesis are based on hydrogen permeation measurements of PdAg membranes, solubility measurements and surface characterization on Pd-based membranes. Permeation and solubility measurements have been performed in the Department of Chemical Engineering, NTNU. The experimental investigations on surface topography analysis were conducted in the AFM lab in Department of Electronics and Telecommunications, NTNU.

Trondheim, January 2013

Live Nova Næss

List of symbols and abbreviations

Ag	Silver
Ar	Argon
AFM	Atomic force microscopy
at.%	Atomic percent
atm	atmosphere pressure (1 atm = 101325 Pa)
Au	Gold
°C	Degree centigrade
H	Hydrogen
HS	Hydrogen stabilization
HTA	Heat treatment in air
K	Kelvin
K_S	Sieverts' constant
M	Metal
mmHg	millimeter of mercury (1 mmHg = 133.3 Pa)
N	Nitrogen
nm	nanometer (1 nm = 10^{-9}m)
Pa	Pascal
Pd	Palladium
PO	Pulled-off
R	Universal gas constant
RMS	Root mean square
Si	Silicon
Sorption	Collective notion for adsorption and absorption
WLI	White light interferometry
wt.%	Weight percent
Y	Yttrium
μm	Micrometer (1 μm = 10^{-6}m)

Contents

Chapter 1

Introduction

An increasing demand for alternative fuels has contributed to extensive studies on how Pd membranes can be used to purify hydrogen. Hydrogen can be utilized in both small-scale and large-scale applications and is currently regarded as one of the most important chemicals in the industry. Concerning large-scale applications, hydrogen is used for e.g. producing ammonia, processing petroleum and reducing processes in metallurgy [1, 2, 3]. Furthermore, hydrogen has good prospective for being a future energy carrier since the energy stored in the molecule efficiently can be converted into electric energy in a fuel cell. The polymer electrolyte membrane (PEM) fuel cell represents such a converter and is much used in small- as well as medium-scale applications (e.g. automotive industry, household power supply). By using pure hydrogen as fuel which reacts with oxygen, the emissions are only water. This is one of the benefits of PEM fuel cell technology in a time where climate change and pollution caused by the use of fossil fuels are large concerns [4]. Unfortunately, hydrogen is not available in nature, so it must be produced from other sources. For a low-emission production, renewable energy sources can be used as an alternative to fossil fuel. Still, large scale hydrogen production from natural gas is today preferred from a cost and efficiency prospective [1].

There are different requirements to hydrogen purity or hydrogen gas mixture composition exist depending on the application. Different production and separation technologies may therefore be applied. To improve the hydrogen production efficiency, palladium-based membranes are developed for use in various chemical reactions. A defect-free Pd membrane will only permeate atomic hydrogen. In addition, Pd exerts good catalytic activity towards hydrogen which makes it favourable from other metals [5]. Applying these membranes in a membrane reactor, where they will be exposed to a gas mixture, will enhance the conversion of equilibrium limited reactions by removing products (H_2). This so-called shift reaction can increase product yield or lower operating temperatures [6]. Furthermore, palladium-based membranes can combine chemical reaction and gas separation in one system which is economically favorable and especially important - produce a pure hydrogen gas.

To commercialize Pd-membranes, some limiting factors need to be reviewed. It is known that pure palladium suffers from embrittlement when exposed to hydrogen as the temperature goes below a critical temperature and pressure [5, 7]. Such embrittlement leads to unfavorable effects e.g. distortion, dislocation multiplication and hardening, which can result in premature fracture in the membrane [5]. Another concern is how carbon compounds affect the membrane in gas-mixtures [8, 9, 10], but this will not discussed any further in this work. Finally, the cost of palladium is a drawback that needs to be taken into consideration.

SINTEF has developed a magnetron sputtering technique to produce thin (1-10 μm) and dense palladium-based membranes [11, 12] which can be used as free-standing films. With no support, possible disturbing effects from porous support can be eliminated during experimental investigation. These membranes are investigated in this work.

Palladium alloys

The combination of good selectivity, high permeability and solubility [13] to hydrogen makes Pd membranes suitable for production and purification of pure hydrogen. As mentioned prevenient, unwanted distortion in the membrane arise at temperatures below a critical temperature (298 °C) and pressure (20 atmospheres) due to formation of hydride phases. Absorption relationship in the palladium-hydrogen system is shown in figure 1.1.
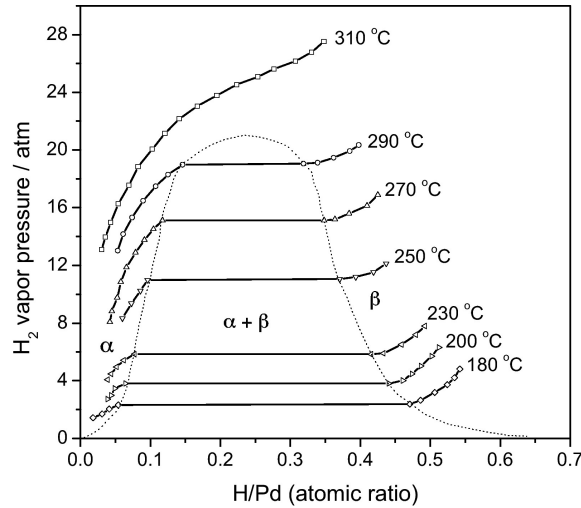
Figure 1.1: Absorption relationship in the palladium-hydrogen system. The hydrogen vapor pressure as a function of H/Pd ratio is shown[14].

Below this critical temperature, the lattice is in α-phase for low hydrogen content, in $\alpha+\beta$ co-existence phase (the miscibility gap) and in β-phase for high hydro-

gen content. The β-phase lattice constant is considerably expanded compared to the lattice constant in α-phase, which lead to severe strain in the material in the co-existence phase. Previous studies show that by alloying palladium with other elements may lower the critical temperature[15, 16] and pressure[17]. This is a result of remarkable lattice change occurring. The palladium silver alloy has shown increased hydrogen permeability compared to pure palladium as well as it ensures dimensional stability by suppressing the $\alpha \rightarrow \beta$ transition[5, 18]. The solubility increases with the amount of silver (up to a certain point), whereas the diffusion of hydrogen decreases. An optimum is found for an alloy composition of 77/23wt.% Pd/Ag[19]. Additionally, palladium silver alloys exhibit improved mechanical properties matched with pure palladium[18].

Scope of work

For optimization of hydrogen permeability in palladium-based membranes, a thorough comprehension of influential factors as solubility and diffusivity is required. Former investigations on thin membranes fabricated by SINTEF have been focused on permeation measurements. The motivation for this work has been to examine the solubility properties for these membranes, which has never been done before. In addition, an objective has been to explore the relation between permeation ability, solubility and surface topography. Parameters as membrane thickness and heat treatment of membrane can significantly alter the performance and has been investigated. In conclusion the results were compared to literature.

Chapter 2

Theory

2.1 Hydrogen permeation process

Hydrogen permeation through a Pd membrane can be represented in the following steps from the high partial pressure side to the low partial pressure side [20]:

1. Molecular transport from the bulk to the gas layer adjacent to the surface

2. Dissociative adsorption onto the surface

3. Transition of atomic H from the bulk metal

4. Atomic diffusion through the bulk metal

5. Transition from the bulk metal to the surface on the low partial pressure side

6. Recombinative desorption from the surface

7. Gas transport away from the surface to the bulk gas

The rate of permeation depends on each of these steps.

The hydrogen flux (J) in mol/s m^2 through the membrane is given by Fick's law [21]:

$$J = \frac{N}{A} = -D_H \frac{dC}{dx} \tag{2.1}$$

where N is the flow of hydrogen through the membrane, A is the membrane area, D_H is the diffusion coefficient and dC/dx is the hydrogen concentration gradient through the membrane. By integrating over the thickness, t, the flux takes a new form:

$$J = \frac{D_H}{t}(C_1 - C_2) \tag{2.2}$$

where C_1 and C_2 is the concentration of hydrogen at the feed (high pressure) and permeate (low pressure) side respectively. When equilibrium is reached between the H_2 molecules in the gas phase and hydrogen atoms at the gas/solid interphase, the hydrogen concentration, C_H (mol/m^3), is proportional to the square root of H_2 pressure in the gas phase. In this case, bulk diffusion is the rate-limiting step. This is expressed by Sieverts' law:

$$C_H = K_S p_{H_2}^{0.5} \qquad (2.3)$$

where K_S (mol/m^{3}Pa$^{0.5}$) is the Sieverts' constant assuming dilute solution and minimal interaction of hydrogen atoms. Sieverts' constant[1] gives an estimate on the solubility of atomic hydrogen in the metal lattice [22]. Substituting for the concentration in equation 2.2 gives:

$$J = \frac{D_H K_S}{t}(p_1^n - p_2^n) \qquad (2.4)$$

where p_1 is the partial pressure on the high pressure side and p_2 is the partial pressure on the low pressure side of the membrane. The permeability, $P = D_H K_S$, is often replaced with the diffusion coefficient and Sieverts' constant. The rate-limiting step is specified by the exponent n in the flux equation. Both diffusion of hydrogen atoms through the membrane and the surface reactions can limit the flux. If bulk diffusion is the rate-limiting step, the n-value will be set to 0.5 [20]. This is the case for relative thick membranes. For thinner membranes, surface-reactions will be the rate-limiting step and the n-value will increase towards 1 [20]. The diffusion coefficient is expressed by:

$$D_H = D_0 \exp(-E/RT) \qquad (2.5)$$

where D_0 is a vibrational diffusion term, E is the activation energy for diffusion and T the temperature in Kelvins [23, 20]. The diffusion coefficient depends exponentially with temperature.

2.2 Thermodynamics

Thermodynamic relations for hydrogen on metal surface and in the bulk material are shown in this theory section.

2.2.1 Thermodynamics for hydrogen adsorption

The thermodynamic reaction between hydrogen and palladium is related to the adsorption/desorption of hydrogen on the metal surface. When a hydrogen molecule

---

[1]The constant description may be perceived as paradoxical since the "constant" depends on parameters as temperature and pressure. The terminology will still be used in this work as it is used in other works [22, 7].

hits the metal surface it may dissociate into two atoms and create a chemical bond with the palladium. An energy barrier needs to be overcome to break the interatomic bond in hydrogen molecule, thus this reaction often happens at higher temperatures. The dissociation process can be written as:

$$2Pd_{surf} + H_{2(g)} \leftrightarrow 2(Pd-H)_{surf} \tag{2.6}$$
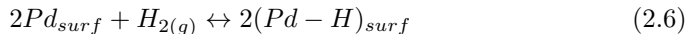
The enthalpy change for this process is written[24]:

$$\Delta H_{ad} = D_{H_2} - 2\chi \tag{2.7}$$

where D_{H_2} is the hydrogen dissociation energy and χ is the strength of the Pd-H surface bond. For a reaction to be spontaneous, the change in Gibb's free energy, ΔG, needs to be negative. Gibb's free energy can be expressed:

$$\Delta G = \Delta H - T\Delta S \tag{2.8}$$

Here the temperature, T, is constant and ΔS is the change in entropy. As a hydrogen molecule adsorbs on a surface, the molecule is limited to two dimensions and one motional degree of freedom will be lost. This usually leads to a decrease in entropy, which is shown with a negative change in ΔS. If the dissociation process is to be spontaneous after assuming negative ΔS, ΔH has to be negative (exothermic reaction). This requirement, $\Delta H_{ad}<0$, gives a new requirement:

$$\chi > \frac{D_{H_2}}{2} \tag{2.9}$$

This indicates that the strength of the Pd-H surface bond needs to be higher than the half of the dissociation energy for an adsorption process to occur. The Pd-H bond energy varies from site to site on the palladium surface. Different surface planes of the same metal may therefore show considerable differences in reactivity.

Once the gas has been adsorbed with a favorably enthalpy change, the van't Hoff equation,

$$\frac{d(\ln K)}{dT} = \frac{\Delta H}{RT^2} \tag{2.10}$$

suggests that high temperatures is required to remove it. Here K is the equilibrium constant, R the gas constant, ΔH the enthalpy change and T the temperature. For high temperatures the equilibrium constant will decrease in exothermic reaction pursuant to Le Châteliers principle. As the equilibrium constant decreases, the reaction will be reversed.

2.2.2 Thermodynamics of dissolved hydrogen

The hydrogen solubility in Pd can be derived using the hydrogen chemical potential [25]. The temperature dependence of Sieverts' constant can be presented in a simple model using the molar enthalpy of desorption, ΔH^0, and the standard molar entropy of desorption, ΔS^0. The equation assumes very low hydrogen content in the metal lattice [26, 27]:

$$\ln K_S = -\frac{\Delta H^0}{2RT} + \frac{\Delta S^0}{2R} \qquad (2.11)$$

A more specific equation for the Sieverts' constant is derived by Fowler et al. [28] and converted by Sonwane et al. [29]. In this equation there is no hydrogen content restriction and K_S decreases for higher temperatures. In order to compare the Sieverts' constants found in this work as a function of temperature, this latter equation is utilized for comparison.

2.3 Thin-film formation

From previous research [30, 31, 32, 33, 34] there is reason to believe that the lattice structure and defects in lattice, affect the solubility and diffusivity properties of a metal. The lattice structure in a thin film depends on the formation process and film deposition process. Grain structure developed in a given deposition process is usually strongly influenced by what happens during nucleation and subsequent growth. Deposition processes as physical vapor deposition and chemical vapor deposition, are used to create thin films. In general, the objective of physical deposition method is to controllably transfer atoms from source to substrate where the film formation and growth proceed atomistically. In chemical vapor deposition on the other hand, a volatile compound that is to be deposited, reacts chemically with other gases. A nonvolatile solid is produced by this reaction and will further deposit atomistically on a substrate. The two most used physical vapor deposition processes are evaporation and sputtering. In this work sputtering was used to create thin films and this process will be explained more carefully in section 3.2 [35].

2.3.1 Nucleation and growth

Thin-film formation involves processes as nucleation and growth. Nucleation is a result of phase (gas, liquid, solid) change. When a system goes from one phase to another, nucleation forms nucleus which are a small ensemble of atoms/molecules in this new phase. If a nucleus will grow depends on the total free-energy change (ΔG) in forming the nucleus [35]:
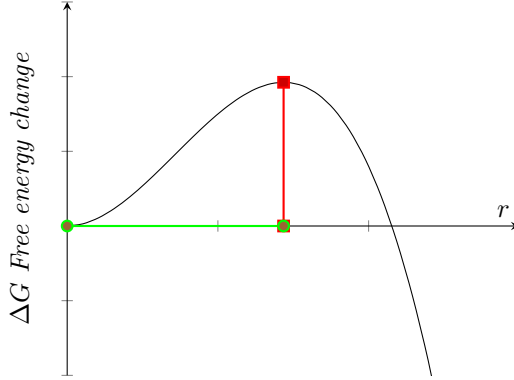
Figure 2.1: Change in Gibb's free energy (ΔG) as a function of nucleus size. The green line represents $r^* =$ critical nucleus size and the red line $\Delta G^* =$ critical free-energy barrier for nucleation.

$$\Delta G = \frac{4}{3}\pi r^3 \Delta G_V + 4\pi r^2 \gamma \qquad (2.12)$$

Here r is the radius of the nucleus, ΔG_V the change in chemical free energy per unit volume and γ the surface energy per unit area. The first term in equation 2.12 describes free-energy change related to volume while the second term relates to area change. To achieve the energy barrier for the nucleation process the equation is differentiated with respect to r.

$$\frac{d\Delta G}{dr} = 0 \longrightarrow r^* = -\frac{2\gamma}{\Delta G_V} \qquad (2.13)$$

r^* is the critical nucleus size. Substituting this expression in equation 2.12 gives:

$$\Delta G^* = \frac{16\pi\gamma^3}{3(\Delta G_V)^2} \qquad (2.14)$$

which is illustrated in figure 2.1.

Since ΔG<0 for spontaneous reactions, the cluster of atoms will shrink for $r < r^*$ and grow for $r > r^*$. For $r > r^*$ the cluster has surmounted the nucleation energy barrier and is thus stable. After this follows growth.

2.3.2 Nucleation and growth on substrate

Nucleation and growth on a substrate succeed as follows. It starts with the first vapor atoms condensing on the substrate and establishing a permanent attachment.

As more and more vapor atoms reach the substrate, a uniform distribution of small islands are formed. Formation of islands develops when the deposited atoms have stronger bonds to each other than to the substrate. These islands grow in size and the density of them increases as more and more atoms condense on substrate. The next stage is merging of the islands. Coalescence occurs when islands collide with each other due to the random motion they execute. A schematic presentation of islands formation is shown in figure 2.2.
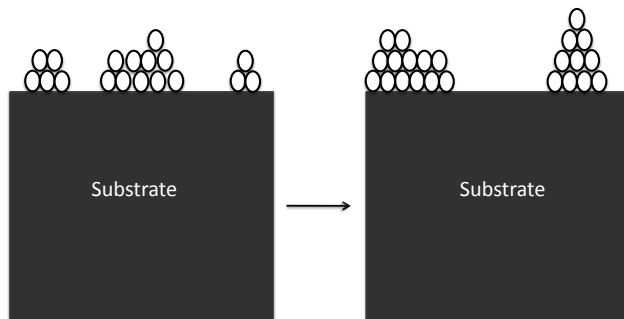
Figure 2.2: Schematic presentation island formation on a substrate.

Each island formed has a specific crystallographic orientation and facet. Two neighbor islands are not necessarily having the same orientation and facets. Under coalescence of islands, the orientation and facets are frequently preserved on islands and at the interfaces between them. With further deposition, all the islands are connected and a continuous film is formed.

2.3.3 Grain boundaries

Grain boundaries are surface or area defects present at the interface between two single-crystal grains of different crystallographic orientation. The atoms in this interface are more loosely bound than the atoms in the bulk. Like atoms on surfaces, they are more energetic than within the grain interior. This favors various atomic reactions and processes as solid-state diffusion, precipitation and impurity segregation. The fraction of atoms associated with grain boundaries is approximately [35]:

$$\frac{3a}{l} \tag{2.15}$$

where a is the atomic dimension and l the grain size.

Grain boundaries arise when islands with different crystallographic orientation meet and coalesce. As the membrane gets thicker, the coalescence processes lead to alterations in the crystallographic orientation in islands. A nuclei with a well defined crystallographic facet may become rounded. Also, a composite island will with time re-assume a crystallographic shape. When two islands with different orientation coalesce, the smaller one will assume the orientation of the larger one. In this process the number of randomly oriented islands will decrease along with the grain boundaries.

2.3.4   Dislocations

Dislocations are line defects that has a definite crystallographic relationship to the lattice. There are two fundamental kinds of dislocations - edge and screw dislocation. The edge dislocation appear when an extra row of atoms is wedged into the lattice. The screw dislocation requires cutting and shearing of the perfect crystal lattice [35]. A distortion on the original cubic cells occurs due to internal stress around each dislocation. The stresses differ around edge and screw dislocation because the lattice distortion differs. Furthermore, the stresses decrease according to a $1/r$ dependence, where r is the distance from the dislocation.

Most metals have dislocations in their as-grown state, mainly as a result of stresses (e.g. mechanical, thermal) associated with the forming process. Dislocations in thin films may occur due to mismatch between the lattice parameters of the film and substrate. In very thin films the lattice would have to be elastically strained to obtain the same lattice parameter as the substrate.

Chapter 3

Materials and methods

3.1 Palladium alloy membranes

Palladium alloys of various composition and thickness were investigated in this work. All membranes were made by SINTEF Materials and Chemistry in Oslo with a magnetron sputtering technique [12, 11]. Primarily as-grown membranes, which were pulled-off original Si-wafer before investigation, were examined. The thickness of the membranes stated in this work are nominal based on approximate sputtering times and previous experience by the manufacturer. The real thickness is expected to be slightly larger.

Furthermore, it is planned to perform white light interferometry (WLI) to obtain the real thickness of these membranes as a follow-up to this work.

In this work samples will be referred to as:

1. **Pulled-off sample (PO)**. As-grown sample removed from Si-wafer.

2. **Heat treated in air (HTA)**. This heat treatment refers to a membrane pretreatment in air at $300\,^\circ$C followed by H_2-reduction at $300\,^\circ$C.

3. **Hydrogen stabilized sample (HS)**. Pre-treatment of hydrogen exposure on membrane.

The pre-treatment/hydrogen stabilization and heat treatment in air are described in section 4.2.5 and 4.2.4, respectively.

3.1.1 Palladium-silver membrane

An alloy composition of 23wt.% consisted for all palladium-silver membranes used in this work. The membranes had different thickness and are listed in table 3.2.

Composition	Condition	Thickness	Sample
Pd/Ag23wt.%	PO	2.2 μm	A1
Pd/Ag23wt.%	PO	4 μm	A2
Pd/Ag23wt.%	PO	6 μm	A3
Pd/Ag23wt.%	PO	8 μm	A4
Pd/Ag23wt.%	PO	10 μm	A5
Pd/Ag23wt.%	HTA	4 μm	B1
Pd/Ag23wt.%	HTA	8 μm	B2
Pd/Ag23wt.%	HS	8 μm	C1

Table 3.1: Pd23wt.%Ag samples investigated.

3.1.2 Other palladium alloy membranes

Two other alloys were also examined in addition to the palladium-silver membranes.

Composition	Condition	Thickness	Sample
Pd/Au5at.%	PO	$\sim$2 μm	D1
Pd/Y5at.%	PO	$\sim$2 μm	D2

Table 3.2: Additional palladium alloy samples investigated.

The thicknesses of these membranes were not given. The sputtering time was 2 hours and 32 minutes and 2 hours and 30 minutes for the palladium-gold membrane and the palladium-yttrium membrane, respectively. The 4 μm palladium-silver membrane has a sputtering time of 5 hours, which helps estimating the thicknesses of these two other alloys. An estimate of approximately 2 μm would be probable.

Supplementary information is needed for the palladium-gold membrane. This membrane had a tinge of a matte surface, which might be a result of a large grain composition. A qualitative evaluation is done in section 5.1.1.

3.2 Sputtering of membranes

Sputtering is a technique used for growing thin films. There are several techniques, whereas magnetron sputtering is presently the most practiced sputtering method. The membranes used in this work are made by magnetron sputtering. Magnetron sputtering is an ion beam sputtering technique where ions are accelerated towards the material to be deposited. A schematic presentation of this is shown in figure 3.1. Inert gas, e.g. Ar-gas, is ionized and used to collide with the target. This leads to ejection of atoms in the target material. Target atoms will further condense on a substrate facing the target. On this substrate the target atoms nucleate to form

islands at first and later create a continuous film. One of the main claims for this type of process is that higher quality of the deposits can be obtained on lower surface temperatures, thus avoiding large scale diffusion on surface which occurs at high temperature processing [36, 37].
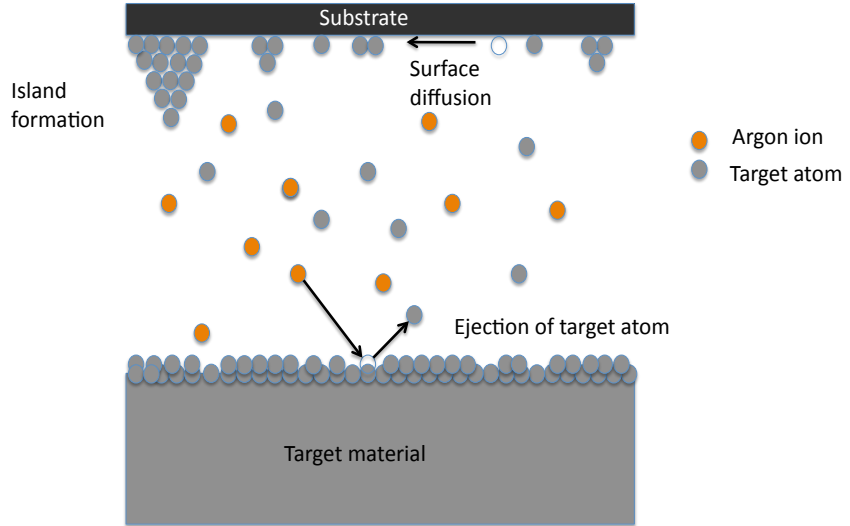

Figure 3.1: Schematic presentation of ion beam sputtering.

In order to maintain the same composition in the film as in the target source, sputtering is a preferred technique in alloy thin film creation. During sputtering there is minimal solid-state diffusion of the atoms in the target material, so the mixed composition in the surface does not alter in the process. This way the mixed composition remains also in the new made thin-film [35].

3.3 Atomic force microscopy

The main principle behind atomic force microscopy (AFM), is to measure the attractive or repulsive forces between a tip and the surface of a sample [38]. If the forces are repulsive or attractive, depend on the distance from tip to surface. Repulsive forces are measured in AFM when the tip is very close to the surface. The

repulsion comes from the electron clouds surrounding the atoms constituting the sample and tip. The forces measured in AFM include mechanical contact forces, van der Waals forces, capillary forces, chemical bonding forces and electrostatic forces to mention some. The tip is attached to a cantilever and scans the surface of the sample under investigation. When the tip approaches the surface of the sample, forces between tip and sample lead to a deflection of the cantilever. Knowing the spring constant, k (N/m), of the cantilever, Hooke's law (3.1) gives the linear relation between the deflection x (m) and the interacting forces F (N) between tip and surface.

$$F = kx \tag{3.1}$$

The AFM uses a laser beam to convert the mechanically induced cantilever deflection to an electric signal. This detection system is based on a laser beam reflected on the top of the cantilever before it hits a photodiode. The photodiode is position sensitive. The laser will hit the photodoide at different positions depending on the deflection of the cantilever. A schematic representation of the AFM is shown in figure 3.2.
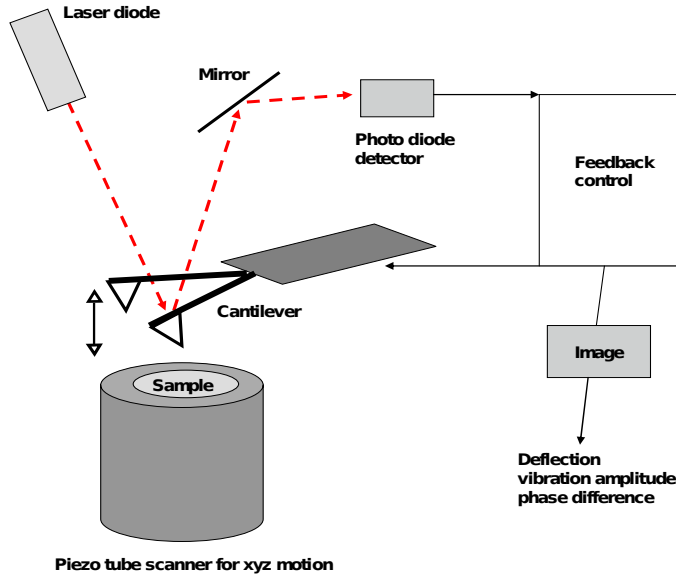

Figure 3.2: Schematic representation of an AFM [39].

As operating signal, either constant force or constant height between sample and tip can be chosen. In the case of constant height, the feed back controllers will

detect the cantilever's deflection. The controllers tell the the piezo tube scanner to adjust so requested height again is reached. The scanners movement is registered and an image of the surface topography may be created.

There are different modes of utilization of AFM. Contact mode, non-contact mode and tapping mode are used depending on the sample. In contact mode the tip is in direct contact with the sample while in non-contact mode the tip and sample are separated with over 100 Ångstrøm. Tapping mode, which is the mode used in this work, is the most common mode and lies between contact and non-contact mode. This oscillating mode starts with the cantilever at its resonant frequency placed above the surface. The tip only taps the surface for a small fraction of its oscillation period. As the tip approaches the surface, the oscillations become damped due to the tip-sample repulsion and the amplitude decreases. Likewise, when the tip approaches a depression in the surface, the repulsion forces are smaller, which leads to an increased oscillation giving a larger oscillation amplitude. To maintain the resonance frequency amplitude, the feedback system move the piezoelectric scanner in z-direction. These changes in oscillation provide information about how the sample surface looks. Tapping mode can be used at soft samples to avoid destruction of sample surface [40].

3.4   Microchannel membrane module

A microchannel membrane module is used to measure the hydrogen flow directly. By varying the pressure on the retentate side of the membrane, the hydrogen flow through the Pd membrane will alter. The microchannel configuration, described in section 4.2.1, is known to help the membrane withstand high differential pressures compared with self-supported configuration [41]. In order to monitor the temperature of the membrane, a thermocouple is connected to the membrane setup. A picture of the furnace utilized in the setup is shown in figure 3.3. Furthermore, a detailed scheme of the microchannel membrane setup can be found in appendix B.
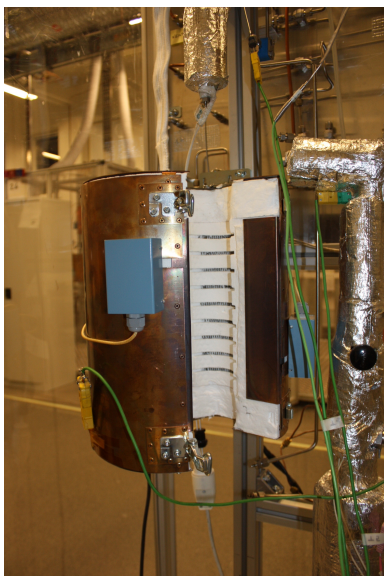
Figure 3.3: The furnace housing used during hydrogen permeation measurements. On the picture the furnace housing is empty. During measurements, the furnace housing is closed and the membrane is placed in the middle.

3.5   Chemisorption

In adsorption based separation processes, an interesting factor is how well pure and mixed gases adsorb on surfaces and absorb in the bulk of solids. Knowing the equilibrium data for a broad range of temperatures and pressures can improve the comprehension of a given process. These data are decisive when it comes to selection of type, size and number of adsorption reactors at given gas feed, product specifications and environmental conditions. Various techniques are used for sorption measurements, thereof gravimetric analysis and volumetric analysis. Gravimetric analysis is based upon the measurement of mass, whereas the volumetric analysis is based on volume. In this work the very light H_2 gas is ad-/absorbed, hence the weight analysis is not ideal. The volumetric analysis method is explained, as this is the method utilized in this work.

3.5.1   Volumetric equilibrium sorption

This equilibrium sorption technique is used to investigate adsorption and absorption of gas on a sample. The amount of gas ad-/absorbed on sample is measured for increasing pressures while the sample is maintained at constant temperature.

The temperature is measured with a thermocouple attached outside the glass reactor close to the sample, see figure 4.6. In volumetric gas adsorption an analysis manifold with known temperature and volume is filled with adsorptive gas. By using the universal gas law shown in equation 3.2 and measuring the pressure, the amount of gas, n (mole), in the manifold is estimated.

$$n = \frac{PV}{RT} \tag{3.2}$$

Here P represents the pressure in the manifold (Pa), V the volume (m^3) of gas , R is the ideal gas constant with value 8.314 (J/mole K) and T is the temperature (K), all in SI-units. A valve connects the analysis manifold and the sample tube of known free-space. Inert gas as helium is used to estimate this free-space volume in the sample tube before measurements. By allowing gas into the sample tube, the gas will adsorb on sample surface and absorb in bulk of the sample, and thereby removed from the gas phase. The pressure is monitored until equilibration is reached and then recorded. A stepwise increase in pressure and subsequent equilibrium pressure recording, give data for the ad-/absorbed amount of gas. The equilibrium pressure is the pressure in the sample tube when equilibrium is reached between H$_2$ molecules in gas phase and hydrogen atoms at the gas/solid interphase. An illustration of the process is shown in figure 3.4.
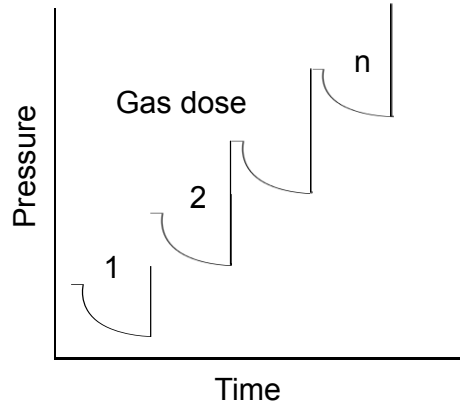

Figure 3.4: Illustration of pressure as a function of time in sorption equilibrium measurements. Incremental doses are inserted into sample tube. The pressure is monitored until equilibrium pressure is reached

Chapter 4

Experimental

4.1 AFM apparatus and parameters

AFM imaging was performed on several samples to determine the topography of the sample surfaces. The objective for this examination was to see to what extent the surface topography correlated with the solubility and permeability properties of the membrane. Bruker Multimode AFM with a Veeco Multimode V controller was utilized carrying out the measurements. Where the sample plate, with prepared sample attached, is located in the AFM apparatus, is shown in figure 4.1a and the specific cantilever and tip used in these measurements for tapping mode is shown in figure 4.1b.
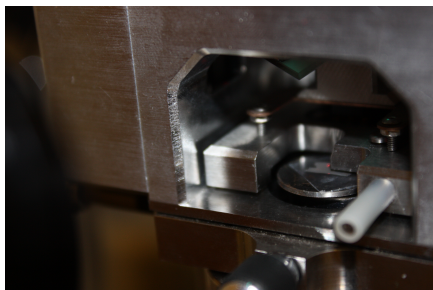
(a) Image of membrane sample in AFM dur-
ing measurement.
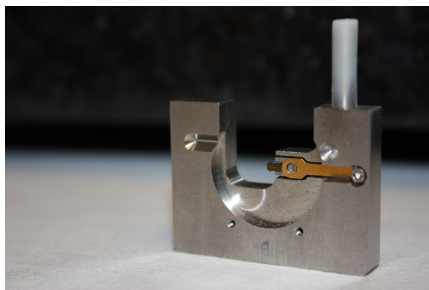
(b) Cantilever and tip utilized in AFM tap-
ping mode.
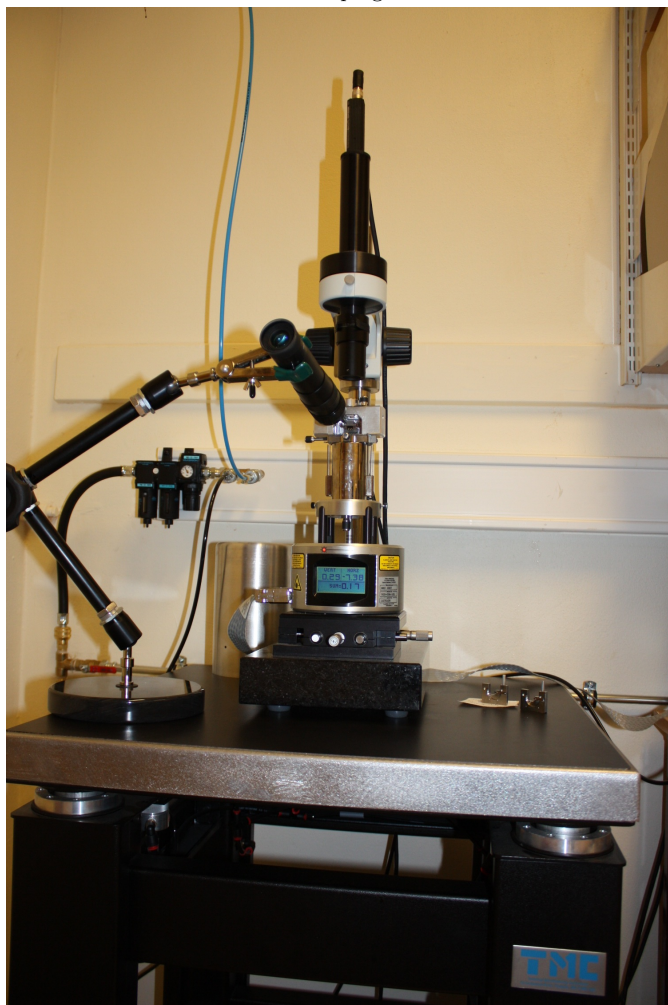
(c) AFM apparatus in full size.

Figure 4.1: Pictures of various parts of the AFM apparatus.

4.1.1 AFM imaged samples and sample preparation

Samples described in section 3.1, except sample D2, were examined with AFM. Both growth/feed-side and substrate/permeate-side were investigated for all samples. All the samples were cut with a scalpel still lying on wafer and pulled-off. The small membrane was further transported from the wafer to a circular sample plate, which was cleaned with ethanol in advance. A double sided adhesive tape was placed on top of the metal piece to keep the membrane sample in place on top of the sample plate, see figure 4.2. Then the sample plate, with sample on, was inserted into the AFM-instrument.

Figure 4.2: Picture of a prepared membrane sample on sample plate.

Roughly 10 different areas were measured. Only 5 areas were measured on sample A5 and C1 due to limited time. These areas were randomly chosen across the sample. For sample B1, B2 and C1, the growth-side was the one facing the feed/retentate-side in the membrane module and substrate side was facing the permeate side, during permeation.

4.1.2 AFM parameters and analyzing tools

The resonance frequency of the tip, was calibrated by the instrument in advance of the scans. This frequency was converted to voltage which varied between 0 - 100 mV. Further this was used as an estimate of how used the tip was. If the resonance frequency exceeded 100 mV, the tip needed to be changed. An unused tip gave clearer imaging than a well used tip.

Three area scan sizes were used for AFM imaging; 1 μm x 1 μm, 5 μm x 5 μm and 10 μm x 10 μm. When imaging substrate sides for the pulled-off samples 1 μm x 1 μm areas were measured. For samples with very large grains the area of 1 μm x 1 μm was excluded.

Analyzing tools were provided by the AFM-instrument software (Nanoscope Software Version 7.2, Veeco) [42]. The *first flattening order* command was performed on all images prior to other analyzing commands. This was used to eliminate noise and tilt that may appear in image. The first flattening order command centers data and removes tilt on each data line.

To evaluate the roughness of the sample surface, the *root mean square* (RMS) command was utilized. The value represents the standard deviation of the z-values from the mean data plane within the image and is calculated with equation 4.1.

$$RMS = \sqrt{\frac{\sum (Z_i)^2}{N}} \qquad (4.1)$$

Here Z_i is the current Z-value and N is the number of points within the image.

To estimate the uncertainty of the RMS-value of an image, 10 images were taken in the same location. A small drift usually occurred during the measurements, which could be seen by a steady relocation of specific protrusions in the image. An area, which was present in all 10 images, was elected and the RMS-value for this area was measured in all 10 images. The average of these RMS-values were calculated. Furthermore, the RMS-value deviating the most from this average value was chosen as uncertainty. This could only be done on images where recognizable protrusions were observed, e.g. the 1 μm x 1 μm areas.

Parameters defining the grains on the membrane surface were estimated using the *particle analysis* command. This command was designed for analyzing well isolated particles. Particles in this context, are co-joined pixels above a given threshold height. In this work the threshold height was set to the top of the height histogram curve, see figure 6.5a found in discussion. The software estimated the location of this height automatically when starting the command. The higher the threshold height, the fewer (the highest) particles are included in the analysis as shown in figure 4.3. The threshold height is used to differentiate particle boundaries.

Output parameters as averages of density, height, area and diameter are used to characterize the particles. Also the appurtenant standard deviations is calculated. The parameter *boundary particles* was chosen in this work.
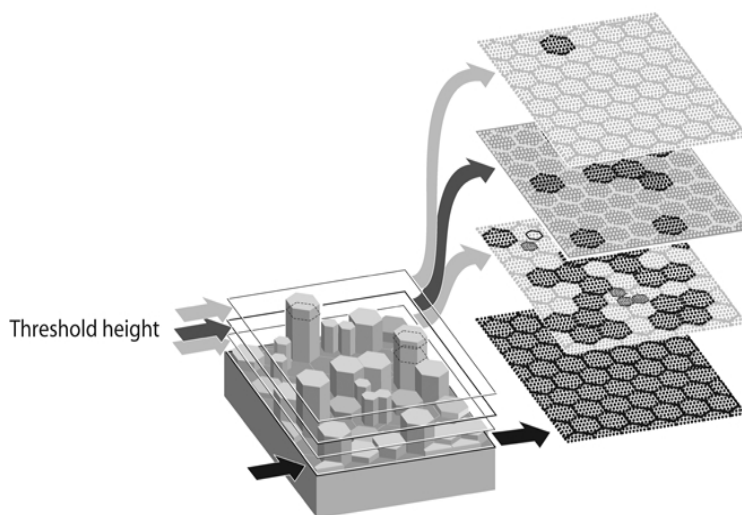
Figure 4.3: Schematic presentation of threshold height used in the particle analysis command [42].

4.2 Microchannel membrane module

To relate permeation behaviour to changes in surface topography, selected permeation measurements were performed. Furthermore, permeation measurements were performed to quantify the change in permeability in the membranes due to heat treatment in air. My contribution to these permeation measurements consisted of doing some stabilization measurements on the membranes after heat treatment in air. The rest was performed by Ph.D candidate Nicla Vicinanza. I also contributed in mounting one of the membranes for permeation measurements.

4.2.1 Membrane configuration

The membrane is placed between two stainless steel metal housings and a polished stainless steel plate. Leakage is prevented with a copper gasket in between the perforated steel plate and the permeate housing. The steel plate had openings that corresponded with the channels on the module giving a total active surface area of 0.78 cm^2. Hydrogen flows along the channels on the feed side, exiting through the retentate channels. Permeated hydrogen flows out of the module on the permeate side. In Figure 4.4, the membrane configuration is shown.
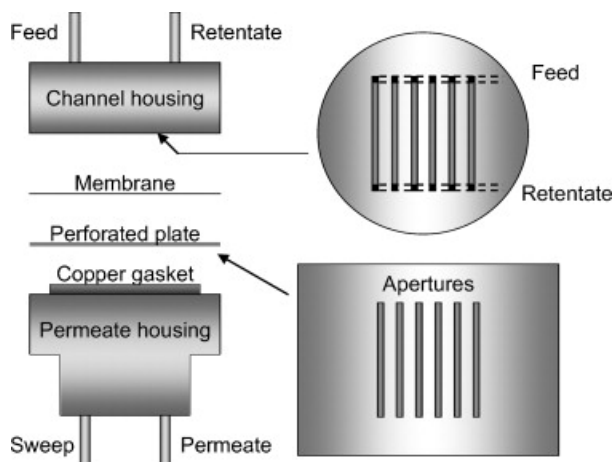
Figure 4.4: Sketch of the microchannel configuration [43]

4.2.2 Mounting of the membrane

The membrane was placed between a feed channel housing and a stainless steel plate. Both were polished and cleaned with acetone in an ultrasonic bath before mounting. The membrane was cut and pulled off the support with an adhesive tape. It was placed on the plate and the other metal housing was placed on top. Eight screws were used to hold the module together, with the membrane in the middle. Further the membrane was placed in the middle of the furnace. The growth side from the sputtered membrane was always facing the feed side of the system.

4.2.3 Procedure measurements

When experiments were performed, the hydrogen flowed towards the membrane on feed side. What did not permeate the membrane went out on the retentate side. The hydrogen that did permeate the membrane, continued out on the permeate side. No sweep gas was used throughout the experiments. By turning a pressure valve, the pressure on the retentate side could be adjusted. The pressure on the permeate side stayed fixed. Measurements with certain pressure drops from the retentate side to the permeate side were selected. The actual measurement of the hydrogen flow was performed using a film flow meter, see figure 4.5. After the hydrogen had permeated the membrane, the flow continued through a glass tube where measuring marks of volume were printed. In the bottom of the glass tube a soap dispenser was placed. By pressing the dispenser, soap film was generated and carried up with the hydrogen. A stopwatch was used to take the time between measurement marks. From these values the flow and flux could be calculated in (ml/min) and (ml/min cm^2), respectively. This was further converted to flux in new units (mol/s m^2) utilizing the ideal gas law. In the conversion, a temperature

of T=293 K (room temperature) and pressure P= 1 atm were applied.

Figure 4.5: Picture of film flow meter.

4.2.4 Heat treatment in air

This heat treatment was executed in the following order:

1. Temperature in oven was set to 300 °C.

2. H_2 flow was put to zero ml/min and 50 ml/min N_2 flow and 50 ml/min Ar flow was injected into the feed channel and sweep channel, respectively. The flows were on for 30 minutes.

3. The feed channel and the permeate channel were removed manually so air could flow into the oven. The membrane was exposed to air at 300 °C for 1 hour before the channels were put back on.

4. To remove air, the module was flushed with 50 ml/min flow of N_2 and 50 ml/min flow of Ar for 30 minutes.

5. H_2 was further injected to stabilize the membrane.

The following permeation measurements consisted of stabilizing the membrane at 300 °C, 350 °C and 400 °C.

4.2.5 Pre-treatment/hydrogen stabilization

The main objective to perform hydrogen stabilization treatment on this 8 μm Pd/Ag23wt.% membrane was to investigate how the surface structure alters from HS treatment to HTA treatment and how this is linked to permeation ability.

The procedure for hydrogen stabilization was carried out in the following way after the membrane was mounted:

1. Temperature in oven was put to $300\,^\circ$C. The heating rate was set to $2\,^\circ$C/min.

2. Simultaneously, 50 ml/min N_2 flow and 50 ml/min Ar flow was injected into the feed channel and sweep channel, respectively. The flows were on until the temperature was reached.

3. Flow of H_2 was injected into the channels.

4. The N_2 and Ar flow were removed.

5. H_2 flow was further injected to stabilize the membrane.

The membrane was left under hydrogen flow with 1 bar pressure on retentate/feed side during night to help the stabilization process. Stabilization at $300\,^\circ$C, $350\,^\circ$C and $400\,^\circ$C was performed.

4.3 Sorption experiments

The equilibrium sorption measurements were carried out using a ASAP 2020 Chemisorption Analyzer produced by Micromeritics Instrument Corporation. The measurements were performed for all as-grown membranes (2.2 μm - 10 μm).

4.3.1 Sample preparation

Membranes used for equilibrium sorption measurements, were removed from the substrate they were originally attached to with a scalpel and tweezers. In the case for the 2μm thick Pd/Ag23wt.% membrane, sample remains stored in closed boxes were used.

The sample was weighted carefully with a Mettler Toledo AG204 Delta Range Analytical Balance or a Mettler Toledo XA204 Delta Range Analytical Balance. In every measurement a sample weight close to 0.1 grams was desired in order to compared to published work on this topic [22]. A glass reactor was used carrying out the experiment. The membrane sample was pressed together and inserted into the glass reactor. Quartz wool was placed beneath and above the sample in the reactor, see figure 4.6. After measurements, the glass reactor was again weighted to correct for possible sample weight change.

4.3.2 H$_2$ equilibrium sorption procedure

The procedure for this sorption experiment was based on an article by Zhang et al. [22]. The sorption experiments were performed on all the as-grown samples described in section 3.1. The membranes were examined at 300 °C, 350 °C and 400 °C. The pressure range was put to 0.15 - 680 mmHg. Three sequences were made, one for each of the different temperature analysis. Table 4.1, Table 4.2 and Table 4.3 represent the sequence to 300 °C, 350 °C and 400 °C, respectively.

Task	Gas	Temperature (°C)	Rate (°C/min)	Time (min)
Evacuation	Helium	100	10	30
Evacuation	Helium	300	10	15
Evacuation		300	10	120
Leak test		300	10	-
Evacuation		300	10	60
Analysis	H$_2$	300	10	-

Table 4.1: Sequence performed at 300 °C.

Task	Gas	Temperature (°C)	Rate (°C/min)	Time (min)
Evacuation	Helium	100	10	30
Evacuation	Helium	300	10	15
Evacuation		300	10	120
Leak test		300	10	-
Evacuation		300	10	60
Flow	H$_2$	300	10	15
Analysis	H$_2$	350	10	-

Table 4.2: Sequence performed at 350 °C.

Task	Gas	Temperature (°C)	Rate (°C/min)	Time (min)
Evacuation	Helium	100	10	30
Evacuation	Helium	300	10	15
Evacuation		300	10	120
Leak test		300	10	-
Evacuation		300	10	60
Flow	H$_2$	300	10	15
Analysis	H$_2$	400	10	-

Table 4.3: Sequence performed at 400 °C.

The palladium membranes were weighted before and after the experiment. Helium

was chosen to be present under heating to prevent embrittlement occurring during absorption of hydrogen [5]. Hydrogen adsorption on palladium is an exothermic reaction which creates heat [44]. Hence to easier achieve stable analyzing temperature at $350\,°C$ and $400\,°C$, a flow of hydrogen was started at $300\,°C$. At each temperature, the experiment was performed twice. Sieverts' constant was calculated using equation 2.3. Performing the measurements twice resulted in two Sieverts' constants per temperature. As a final result, the average of these constants was calculated.

Figure 4.6: Palladium alloy membrane in a glass reactor between quartz wool. On the end of the thin black metal bar seen behind the glass reactor, the thermocouple is localized which is in proximity of the membrane.

Chapter 5

Results

In this chapter all results from the experimental work are presented. The first section (5.1) contains the topographic results from AFM investigation, in the second section (5.2) the permeation results are shown and in the final section (5.3) the solubility results for the sorption measurements are presented.

5.1 Surface topography results

The motivation behind surface topography investigation was to see if there was any correlation between changes in permeation properties over time due to different exposures, and changes in surface structure. Investigating sample D1 (PdAu) with AFM, was done to verify unusual large grain size on growth side of the membrane.

5.1.1 AFM image results

The presentation of the AFM results is divided into two parts. First, AFM images of the pulled-off membranes are presented succeeded by the membranes which have been exposed to different treatments. The growth side is always placed towards feed side and substrate side towards permeate side in the membrane microchannel module. Feed and permeate is added to the surface description when the membranes have been exposed to treatment (HTA or HS). Only some images have been selected from the results to emphasize the alterations in surface structure. The image area size is chosen in regard to size of protrusions. To make surface structure development visible, an area size that makes this possible is required. Finally, all images can be found in appendix A where they are presented in both 2D and 3D.

Surface topography of pulled-off membranes:

Growth side of 2.2-10 μm Pd/Ag23wt.% (Sample A1-A5)

Figure 5.1 shows how the surface topography alters with thickness. Larger lateral size of protrusions as well as height increase are observed for increasing film thickness. This correlates with anticipated development of grain growth described in 2.3.1. It seems like sample A5 deviates from this trend, which will be discussed later. Density of protrusions decreases with increasing film thickness, which can be understood as a natural consequence of coalescence of smaller grains. This development correlates with the roughness value estimations for each membrane, which are listed in table 5.1.

(a) Growth side of 2.2 μm thick Pd/Ag23wt.% membrane (A1)

(b) Growth side of 4 μm thick Pd/Ag23wt.% membrane (A2)

(c) Growth side of 6 μm thick Pd/Ag23wt.% membrane (A3)

(d) Growth side of 8 μm thick Pd/Ag23wt.% membrane (A4)

(e) Growth side of 10 μm thick Pd/Ag23wt.% membrane (A5)
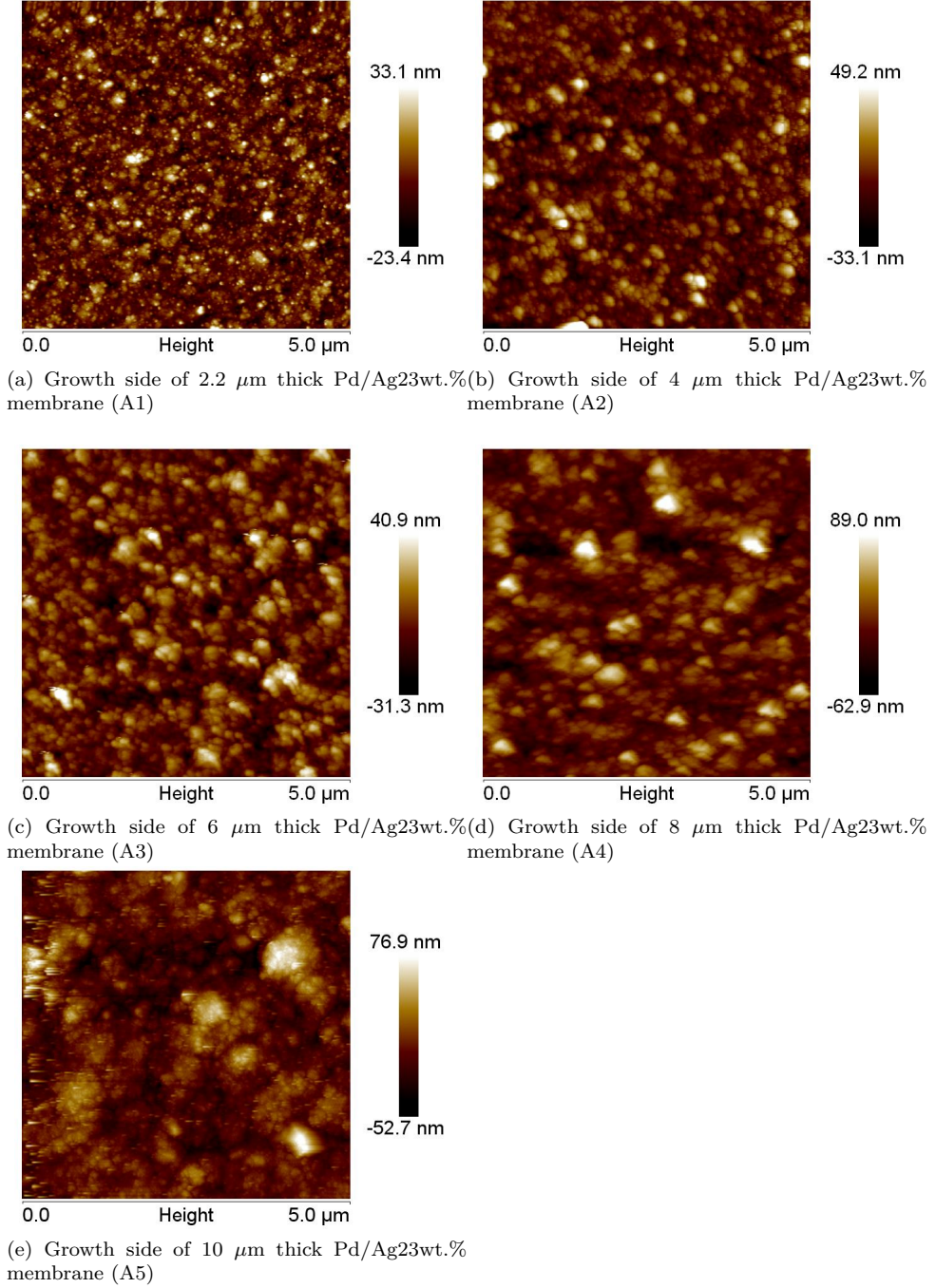
Figure 5.1: Images of 2.2-10 μm Pd/Ag23wt.% pulled-off membranes growth side. An image size area of 5x5 μm^2 is used for all images so one easier can detect the surface structure development.

Growth side of Pd/Au5at.% (Sample D1)

The images for this sample, shown in figure 5.2, confirms the suspicion of anomalous grain growth on this pulled-off membrane. The protrusion heights are large and the protrusion density differs vastly from what is observed for the samples with resembling thickness (2.2 μm thick Pd/Ag23wt.%).

(a) Growth side of 2.2 μm thick Pd/Ag23wt.% (Sample A1) (b) Growth side of $\sim$1.5 μm thick Pd/Au5at.% (Sample D1)
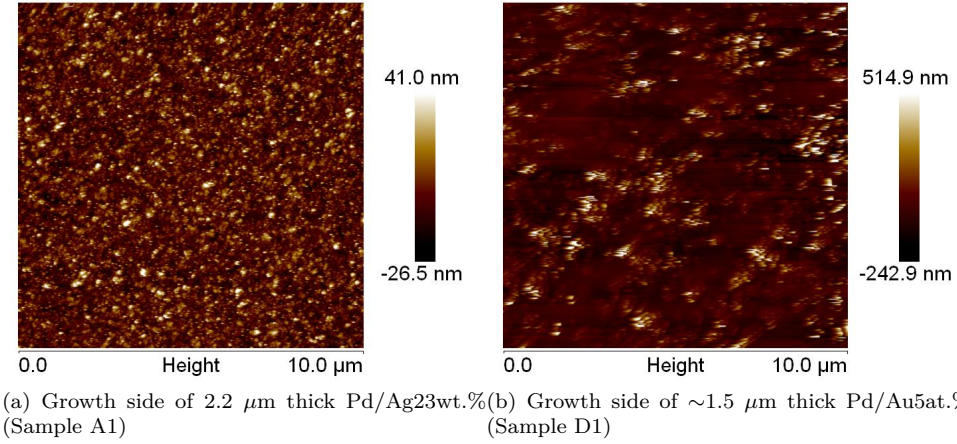
Figure 5.2: $\sim$2 μm thick Pd/Au5at.% compared with 2.2 μm thick Pd/Ag23wt.%. An area size of 10x10 μm^2 is chosen.

Substrate side for Pd/Ag23wt.%

Little difference can be observed on substrate side of the pulled-off Pd/Ag23wt.% membranes. Small height variation for the protrusions and images which are hard to distinguish from each other, indicates quite similar substrate surface for all these pulled-off samples. Noteworthy is the observation of the low height for these grains which points out how flat these surfaces are. Image of the substrate side of 2.2 thick μm Pd/Ag23wt.% (Sample A1), 6 thick μm Pd/Ag23wt.% (Sample A3) and 10 thick μm Pd/Ag23wt.% (Sample A5) are selected to emphasize the approximately non-existing changes in surface structure, see figure 5.3. The remaining images can be found in appendix A.

(a)   2.2 μm   thick
Pd/Ag23wt.%   (Sample
A1)

(b) 6 μm thick Pd/Ag23wt.%
(Sample A3)

(c) 10 μm thick Pd/Ag23wt.%
(Sample A5)
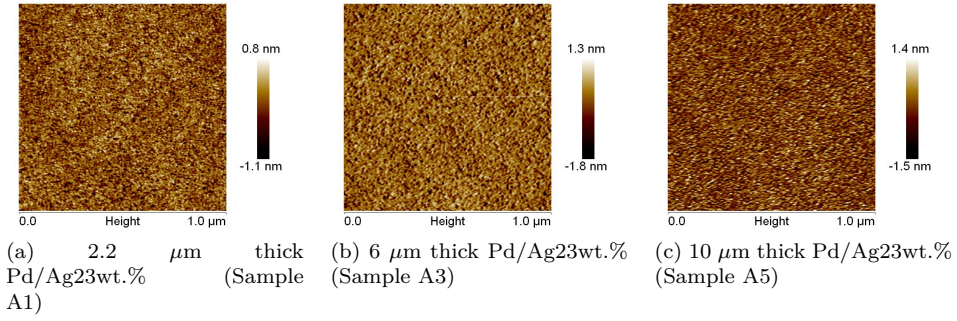
Figure 5.3: Images of the substrate side of 2.2 μm thick Pd/Ag23wt.% (Sample A1),
6 μm thick Pd/Ag23wt.% (Sample A3) and 10 μm thick Pd/Ag23wt.% (Sample
A5). All images are shown with area size 1x1 μm^2.

Surface topography of the heat treated membranes:

Growth/feed side of heat treated membranes

Relative large grains can be observed for the 4 μm Pd/Ag23wt.% membrane after
heat treatment in air. Compared to the pulled-off sample with same composition
and thickness (sample A2) the height of protrusions are larger, hence the grains on
the heat treated sample have grown. Furthermore, the protrusion density is lower
after heat treatment than before which is a result of larger grains. The comparison
of the two membranes before and after HTA is shown in figure 5.4.

(a) Growth side of 4 μm thick Pd/Ag23wt.%
membrane (Sample A2)

(b) Growth/feed side of 4 μm Pd/Ag23wt.% after
heat treatment in air (Sample B1)
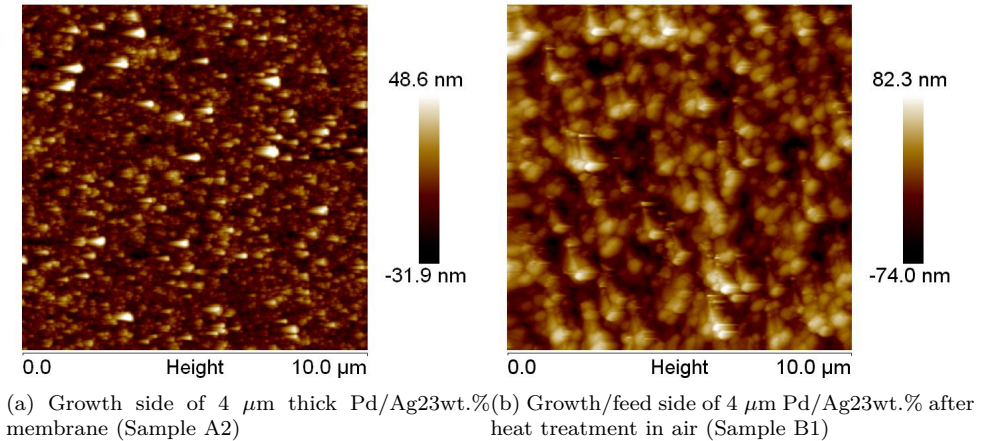
Figure 5.4: Image of 4 μm thick Pd/Ag23wt.% membrane before and after HTA.
An image size area of 10x10 μm^2 is chosen to show the alteration.

The same alteration in grain growth is observed on the 8 μm thick Pd/Ag23wt.% membrane (sample B2), which also has been exposed to HTA. Before a membrane is heat treated in air, the hydrogen flux through the membrane is stabilized. How the surface topography looks after such hydrogen stabilization is shown in figure 5.5b. This is placed in the middle of the pulled of membrane and the heat treated membrane to show the grain growth development, see figure 5.5. The growth/feed surface exposed to HS shows protrusions with similar height as the protrusions on the membrane of equal thickness exposed to HTA (figure 5.5c). However, larger lateral grain sizes are observed for the membrane exposed to HS. Deviation in the shape of protrusions is also detected.

(a) Growth side of 8 μm thick Pd/Ag23wt.% membrane (Sample A4)

(b) Growth/feed side of 8 μm thick Pd/Ag23wt.% membrane after hydrogen stabilization (Sample C1)

(c) Growth/feed side of 8 μm thick Pd/Ag23wt.% membrane after heat treatment in air (Sample B2)
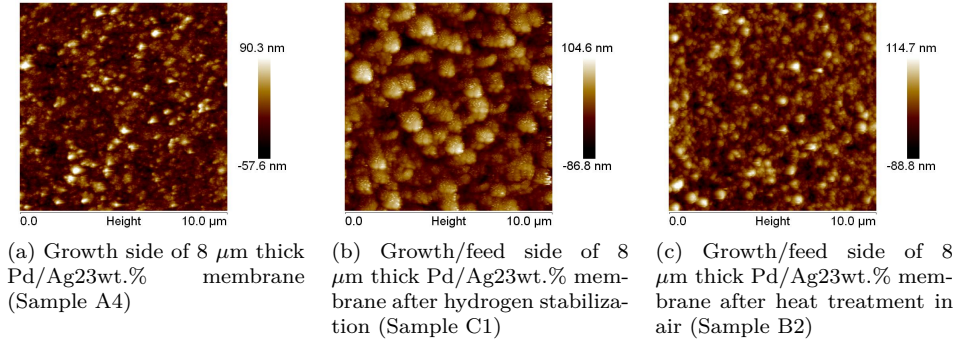
Figure 5.5: Image of 8 μm thick Pd/Ag23wt.% membrane before and after HS/HTA. An image size area of 10x10 μm^2 is presented to illustrate the change.

Substrate/permeate side of heat treated membranes

In figure 5.6, the substrate side of the 4 μm thick Pd/Ag23wt.% shows grain growth as a result of HTA compared with the 4 μm thick pulled-off membrane. From having a approximately flat surface before HTA there is a vast change in surface structure. This is also indicated by the protrusion height.

(a) Substrate side of 4 μm thick Pd/Ag23wt.% (Sample A2). 1x1 μm^2

(b) Substrate/permeate side of 4 μm thick Pd/Ag23wt.% after heat treatment in air (Sample B1). 5x5 μm^2
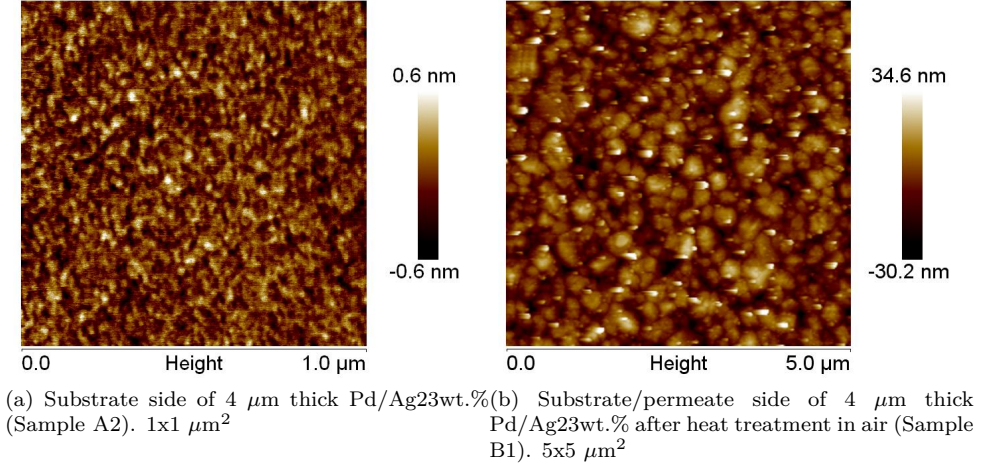
Figure 5.6: A comparison of 4 μm thick Pd/Ag23wt.% substrate/permeate side before and after heat treatment in air. The images are shown of different size areas which impede a direct comparison.

(a) Substrate side of 8 μm thick Pd/Ag23wt.% (Sample A4). 1x1 μm^2

(b) Substrate/permeate side of 8 μm thick Pd/Ag23wt.% after hydrogen stabilization (Sample C1). 1x1 μm^2

(c) Substrate/permeate side of 8 μm thick Pd/Ag23wt.% after heat treatment in air (Sample B2). 5x5 μm^2
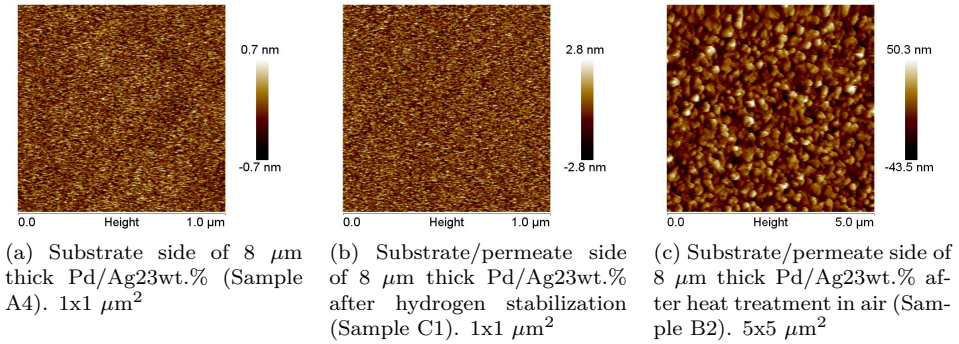
Figure 5.7: A comparison of 8 μm thick Pd/Ag23wt.% substrate/permeate side before and after HS/HTA. The images are shown of different size areas which impede a direct comparison.

As for growth side for the 8 μm thick Pd/Ag23wt.% membrane, the substrate side development is pictured in figure 5.7. Substrate side after hydrogen stabilization

(figure 5.7b) shows no significant change in surface structure. The height of protrusions is very small on both the pulled-off and hydrogen stabilized sample surface. From having a approximately flat surface after HS, a vast change in surface structure is observed as a result of HTA (figure 5.7c). Higher protrusions and decreased protrusion density are observed as a result of HTA.

5.1.2 RMS-values

To quantify the alterations in the surface, an estimation of the surface roughness was executed. The mean RMS values for growth side of the membranes are found in table 5.1 whereas the mean RMS values for the substrate side are found in table 5.2.

Growth side	Average RMS values		
Sample	1μm x 1μm	5μm x 5μm	10μm x 10μm
A1	7.1±0.2	8.4	9.5
A2	8.0±0.3	10.5	10.8
A3	8.2±0.2	10.6	11.3
A4	13.0±3.2	20.4±0.2	21.0
A5	8.5	15.4	21.1
B1	-	24.6	24.6
B2	-	26.9	27.3
C1	-	24.0	29.9
D1	-	33.1	64.9
D2	-	-	-

Table 5.1: Average RMS values on the membrane growth side.

In table 5.1, it can be seen that the average RMS value increases in general with increasing image area size. The alteration in average RMS values for the Pd/Ag23wt.% samples shows an increase from the thinnest to the thickest membrane, except for sample A5. Also, the roughness for the 4 and the 6 μm membranes do not seem to differ. The roughness decreases for the 10 μm thick membrane compared with the 8 μm thick membrane. This is all consistent with the qualitative observations in the images. The HTA samples (B1 and B2) show similar roughness for area size 5x5 μm^2. The RMS for B2 is slightly higher than for B1. Sample C1 has a roughness comparable to B1 and B2. There are larger deviations for the 10x10 μm^2 area for these three samples. In this area, the roughness of sample C1 is the largest.

The standard deviations in RMS-values were estimated for some of the membranes. These values are based on qualitative interpretation of the AFM-images, hence deviations will naturally occur if the estimations were to be reestimated by others. These estimates are comparable with previous work [45] for equal surface topographic investigation on similar membranes, and describe somehow the variation

of protrusion heights.

As expected, the RMS-value of the Pd/Au sample (sample D1) is much higher compared to the thinnest palladium-silver membrane (Sample A1). These RMS values are the highest found in this work. This can also be seen in the AFM images, see figure A.9.

Substrate side	Average RMS values		
Sample	$1\mu m$ x $1\mu m$	$5\mu m$ x $5\mu m$	$10\mu m$ x $10\mu m$
A1	0.29	0.21	-
A2	0.19	-	-
A3	0.38	-	-
A4	0.40	-	-
A5	0.21	-	-
B1	-	9.0	8.7
B2	-	14.3	13.5
C1	0.9	1.0	-
D1	0.17	-	-
D2	-	-	-

Table 5.2: Mean RMS values on the membrane substrate side.

Approximately equal roughness on substrate side for all pulled-off Pd/Ag membranes is registered. Here only the 1x1 μm^2 gave a reasonable result due to the flat surface. Sample B1 and B2 had visible grains on permeate side seen in the images, which supports the roughness found for these samples. The permeate/substrate surface for sample C1 shows very low roughness in the 5x5 μm^2 area compared to the HTA samples, which also supports image observations.

The RMS value for substrate side on sample D1 is in the same low range as for the other pulled-off membranes confirming a flat substrate-interface surface.

5.2 Permeation measurement results

Permeation measurements were executed to see how well hydrogen is transported through the membrane and how the permeation changes as a result of different treatments. Permeability and permeance were estimated for the investigated membranes. These quantitative values were later used when permeation abilities were compared to surface topography.

Permeation measurements were in total performed on four membranes; a 4 μm thick Pd/Ag23wt.% membrane (Sample B1), 8 μm thick Pd/Ag23wt.% membrane (Sample B2), 10 μm thick Pd/Ag23wt.% membrane (no sample name) and again 8 μm thick Pd/Ag23wt.% membrane (Sample C1). The latter 8 μm thick Pd/Ag23wt.%

membrane, only hydrogen stabilization was performed. The permeation measurements on the 8 μm thick Pd/Ag23wt.% membrane (Sample B2) and hydrogen stabilization procedure on the 8 μm thick Pd/Ag23wt.% membrane (Sample C1) were solely performed by Ph.D. candidate Nicla Vicinanza. The permeance results for these measurements are still included in table 5.3 to be able to relate the permeation results to the topography results of the membranes which is found in this study. Furthermore, measurements on the 10 μm thick Pd/Ag23wt.% were performed. Unfortunately a leakage was detected in the measurement setup for this membrane, thus the results are not included in table 5.3. The graphical presentation of the permeation results are still included in appendix C.

The permeation measurements of the 4 μm thick Pd/Ag23wt.% membrane, which can be seen in figure 5.8, are chosen as an example for how these measurements were plotted. The graphical presentation of the remaining permeation measurements are included in appendix C.
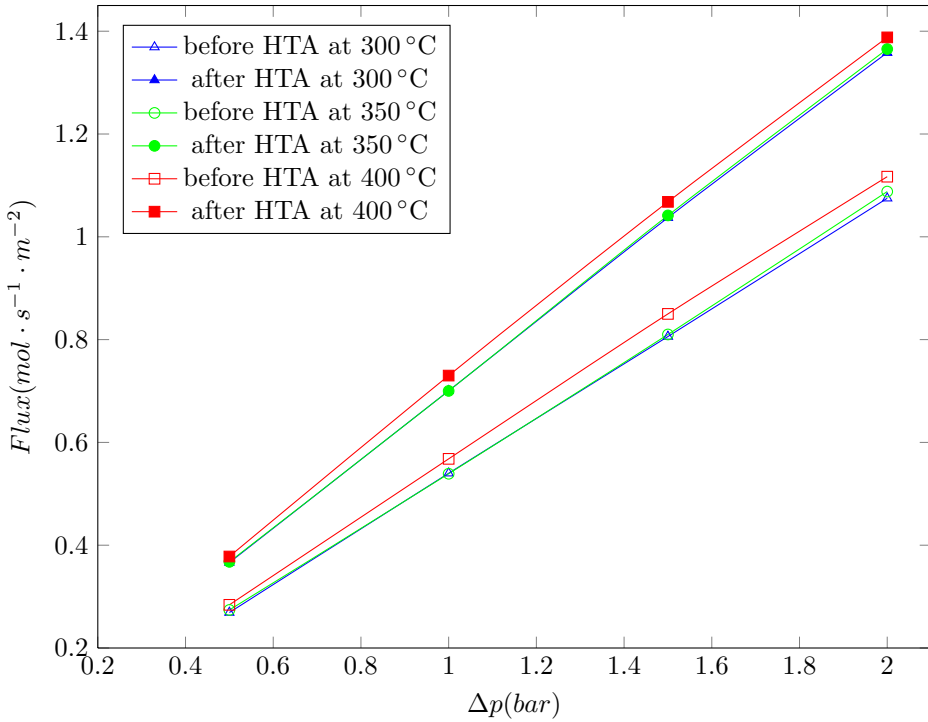
Figure 5.8: Results for 4 μm thick Pd/Ag23wt.% membrane (Sample B1) at 300 °C, 350 °C and 400 °C before and after HTA. Notice that the axes do not begin at 0.

The results of the flux (mol s^{-1} m^{-2}) as a function of differential pressure (bar) across the membrane are shown in figure 5.8. The experiment was performed at 300 °C, 350 °C and 400 °C. The flux stabilized at different values for each temperature and the stabilization process took $\sim$150 hours. The flux fluctuated before it

stabilized, however only the last measurement showing the stable flux is included in the figures. In figure 5.8 one can see how the flux increases linearly with pressure difference over the membrane in accordance with equation 2.4. In table 5.3 the flux is converted to permeance which represents the flux per square pressure in Pa. A temperature dependence can be observed for the permeance. For higher temperatures the permeance increases, which applies to all samples. In addition, the flux is higher at 400 °C than at lower temperatures. The effect of heat treatment in air resulted in higher flux for at all temperatures. Quantitative values for these changes are listed in table 5.3 in addition to the results for the 8 μm thick Pd/Ag23wt.% membranes being exposed to HTA and HS.

Sample	Temperature °C	Permeance $(mol/m^2sPa^{0.5})$x10^{-3}		Improvement in permeance (%)
		Before HTA	After HTA	
Sample B1	300	4.26	5.53	30
	350	4.29	5.55	29
	400	4.47	5.70	28
Sample B2	300	2.83	2.96	5
	350	2.87	3.03	6
	400	2.99	3.21	7
Sample C1	300	2.26	-	-
	350	2.29	-	-
	400	2.37	-	-

Table 5.3: Stabilized permeances (mol/m^{2}sPa$^{0.5}$) and improvement of permeance after HTA. For sample C1, the permeance after hydrogen stabilization is displayed.

Sample	Temperature °C	Permeability $(mol.m/m^2sPa^{0.5})$x10^{-8}	
		Before HTA	After HTA
Sample B1	300	1.7	2.2
	350	1.7	2.2
	400	1.8	2.3
Sample B2	300	2.3	2.4
	350	2.3	2.4
	400	2.4	2.6
Sample C1	300	1.8	-
	350	1.8	-
	400	1.9	-

Table 5.4: Permeability (mol.m/ m^{2}sPa$^{0.5}$) for membranes before and after heat treatment in air. For sample C1, the permeability after hydrogen stabilization is displayed.

In table 5.4 the permeability for the membranes exposed to treatment is shown.

This value is permeance multiplied with membrane thickness. The permeabilities have similar values before HTA (except sample B2) and after HTA.

Both surface topography as well as permeation measurements were performed on the three membranes; sample B1, sample B2 and sample C1. The permeation measurements of these membranes are therefore presented in table 5.3 and 5.4. The permeances of the membranes show a distinct thickness dependence. Before HTA the permeance for the 4 μm thick Pd/Ag23wt.% membrane (Sample B1) at 300 °C is a factor of 1.5 higher than the 8 μm thick membrane (Sample B2). The same comparison after HTA shows that the permeance increased with a factor of 1.84 at the same temperature. Furthermore, the permeance for the 4 μm thick Pd/Ag23wt.% membrane at 300 °C (Sample B1) before HTA is a factor of 1.89 higher than the 8 μm thick hydrogen stabilized membrane (Sample C1). The expected theoretical increase in permeance, given by equation 2.2, should be a factor of 2. The permeation measurements show an increase in flux after heat treatment in air at all temperatures. This relative increase is presented in table 5.3. The relative increase is higher for sample B1 than B2. Sample B1 showed that the permeance had increased close by a factor of 1.29 while for B2, only 1.06. For each membrane, there is not observed that the relative change depend on temperature. For both membranes the relative change is quite similar for all three temperatures.

The permeance after hydrogen stabilization (sample C1) is about 80 % of what was measured for sample B2 before heat treatment in air. These membranes are of equal composition and thickness, thus a similar permeance is expected.

5.3   Sorption results

It is known that both diffusion and solubility affect the total permeation through a membrane. Temperature, pressure, composition as well as microstructure are actuating factors for solubility of hydrogen in a membrane. To know the impact these factors have on the solubility, they have to be examined isolated from each other. The reason for solubility measurements performed at constant temperature and equal composition in this work, is based on this argument. Keeping some parameters constant will elucidate other solubility dependencies.

The isotherm for sample E is plotted as an example for the sorption results in figure 5.9. The original isotherm results for the remaining samples can be found in appendix D. The isotherm shows the sorption amounts of atomic hydrogen (μmol/g) versus the square root of the equilibrium pressure (Pa$^{0.5}$). For all temperatures the graph shows an approximately linear slope. This indicates that the linear solubility dependence of the square root equilibrium pressure is maintained. The linear approximations for the data sets, is represented by the two continuous linear graphs. The slope of each graph represents Sieverts' constant. The deviation of the data plot sets at the same temperature differed as can be seen in the appendix D. For

this reason the average of the two slopes were calculated, see table 5.5.
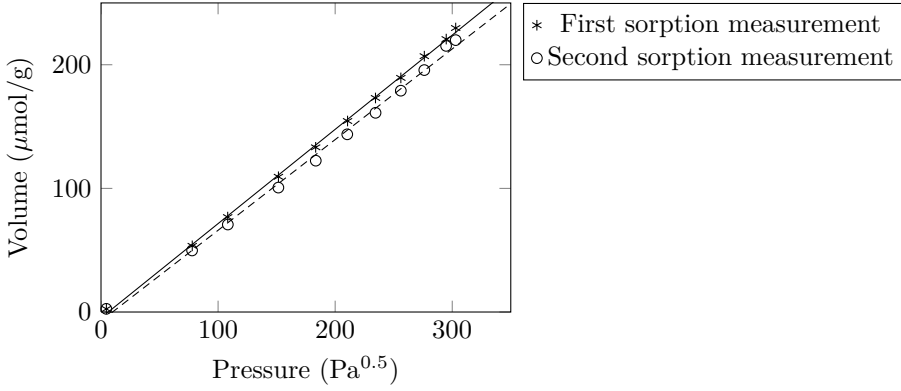
Figure 5.9: Isotherm result for 10μm Pd/Ag23wt.% (Sample A5) at $300\,°$C.

The observation of solubility dependence of thickness is presented in figure 5.10 and quantitative values are given in table 5.5.

Sample	Temperature ($°$C)	K_S (μmol/g.Pa$^{0.5}$)
	300	1.02
A1	350	0.75
	400	0.60
	300	0.94
A2	350	0.75
	400	0.60
	300	0.83
A3	350	0.56
	400	0.43
	300	0.70
A4	350	0.51
	400	0.42
	300	0.75
A5	350	0.56
	400	0.44
	300	0.28
D1	350	0.22
	400	0.16
	300	0.86
D2	350	0.65
	400	0.51

Table 5.5: Sieverts' constants calculated for various palladium alloy membranes on temperatures $300\,°$C, $350\,°$C and $400\,°$C.

One may observe solubility decrease for increasing membrane thickness. The 10 μm Pd/Ag membrane is in divergency with this trend and show a larger Sieverts' constant than the 8 μm Pd/Ag membrane. The slightly solubility dependence of temperature is noticeable for all membrane thicknesses, whereas the highest solubility was measured for the the lowest temperature. As the temperature increased, the solubility decreased. The decreasing solubility as a function of thickness is more pronounced for 300 °C. At 350 °C and 400 °C there is no continuous decreasing trend. Sample A1 and A2 gave similar Sieverts' constants at 350 °C and 400 °C, which sample A3 and A4 also did but at a lower value.
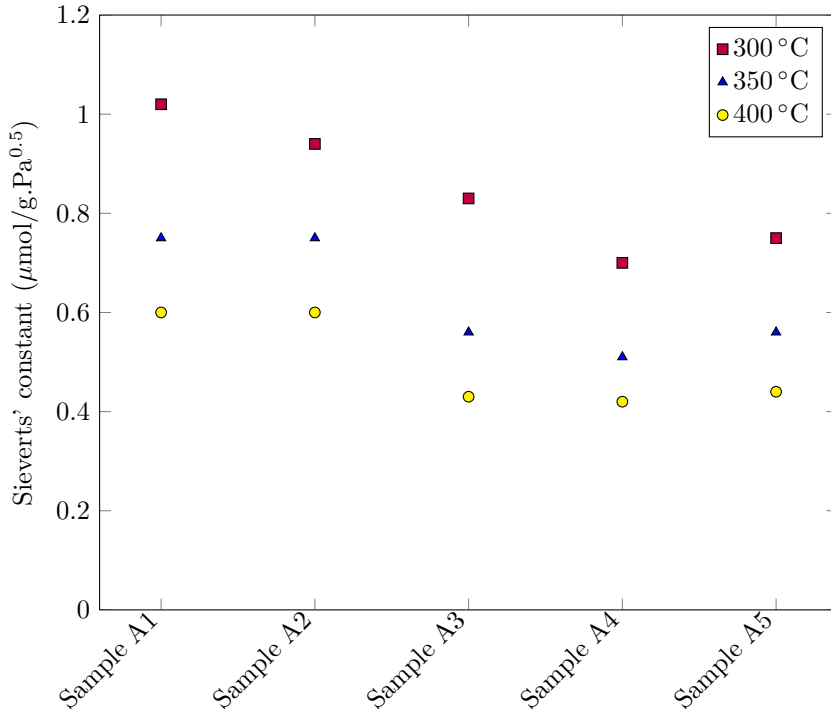
Figure 5.10: Sieverts' constants for Pd/Ag23wt.% membranes of various thicknesses.

The plot of Sieverts' constant for other alloys shown in figure 5.11 shows the highest solubility for the Pd/Ag membrane, succeeded by the Pd/Y membrane and finally the Pd/Au membrane. The thinnest Pd/Ag membrane is included for comparison with the other palladium alloys. These membranes have similar thickness, but as mentioned earlier, the Pd/Au membrane shows abnormal surface structure which needs to be taken into consideration in the discussion. The temperature dependence is also observed for these alloys.
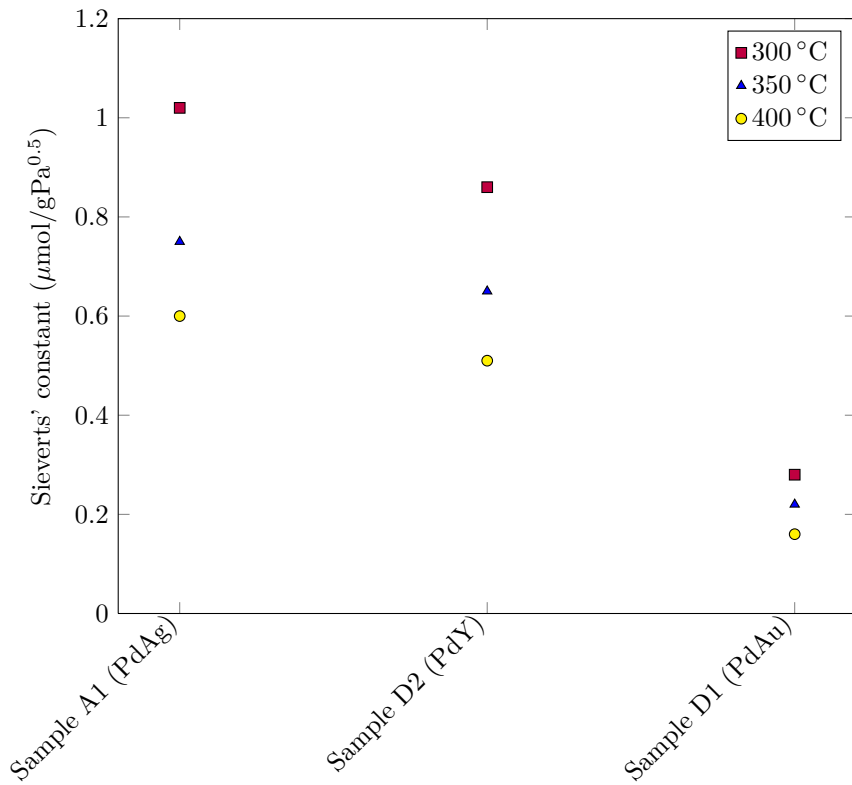
Figure 5.11: Sieverts' constants for palladium alloys of similar thicknesses. Pd/Ag23wt.% (Sample A1) = 2.2 μm, Pd/Au5at.% (Sample D1) $\simeq$ 2 μm and Pd/Y5at.% (Sample D2) $\simeq$ 2 μm.

Chapter 6

Discussion

The discussion is divided into four sections. First are the surface topography results discussed in section 6.1. Section 6.2 begins with discussing main observations of permeation, succeeded by permeation results of HTA. These latter permeation results will also be related to surface topography. In section solubility measurements are discussed both for Pd/Ag membranes and other Pd-based alloys. Also here surface topography results are brought in and related to the solubility results. Finally, sources of error are discussed in section 6.4.

6.1   Surface topography

6.1.1   Pulled-off membranes

There is observed a significant variation in the surface topography for the pulled-off membranes of equal composition and different thickness. The roughness values on growth side correlate with this alteration detected in the images. The images show a higher density of protrusions for the thinnest membranes. As the membranes get thicker, the protrusions increase in height and width and the density decreases. The height variations for protrusions are also larger for thicker membranes. Higher protrusion density for thinner membranes was also discovered by Ramachandran et al. [45]. How the nucleation and growth processes elapse is based on the overall goal to reduce Gibb's free energy. Basic theory on this is given in chapter 2.3.1. Surface/interface area reduction is often a natural result of this driving force to minimize the grains/crystallites. In the grain growth process some grains get larger whereas others get smaller and disappear.

The assumption that grain boundary density correlates with surface roughness and qualitative observations on protrusion size, is drawn. The effect grain boundaries have on solubility will be discussed later. In this regard it is important to explain

the origin for this assumption. It is important to point out that the surface topography investigation performed in this work does not prove the existence of grain boundaries neither the density of them. Their presence and how the grain boundaries evolve with surface roughness, is based on work by others [46, 47]. Thorough microstructural investigations on the same type of Pd/Ag membranes as used in this work, have been performed by Tucho et al. Tiny crystallites, high density of lattice defects and dislocations at and close to the substrate-interface surface of as-grown membranes were found in the work by Tucho et al. In addition, Mekonnen et al. point out observations of dislocations in the lattice. The lateral grain size decreases from top of the growth side toward the substrate-interface surface, where the grains are smaller. They also found that the lateral grain size and surface roughness on growth side tend to increase with increasing film thickness. Findings are assumed valid in this work, since the membrane thin film fabrication was the same (i.e. magnetron sputtering, see section 3.2). Microstructural investigation on the membranes used in this study is still required before any definite conclusions can be drawn concerning grain boundaries and other defects.

The substrate side of the membranes with similar composition and different thickness did not alter from membrane to membrane. AFM images showed the same height range and a very similar appearing surface structure. The roughness values were all estimated to be between 0.21 nm and 0.39 nm indicating that the surfaces were flat. This flat surface on substrate side have earlier been observed on TEM cross-section images [47]. This is in agreement of the growth process described in section 2.3.2.

6.1.2 Heat treated and hydrogen stabilized membranes

Concerning the heat treated membranes, alterations in surface structure on feed/growth side were observed. A lower density of protrusions and lateral grain increase after HTA witnesses grain growth. Both the 4 μm and the 6 μm membrane demonstrated this effect. The substrate/permeate side of the heat treated membranes showed very different surface structure from the substrate side of the pulled-off membranes. There was observed a drastic change in grain structure from being totally flat to estimate roughness values of 9-14 nm on the new altered substrate/permeate surface. This observation indicates that heat treatment in air at 300 °C results in a grain growth process for both growth/feed and substrate/permeate side. The AFM images on substrate side before HTA and after, cannot be directly linked due to difference in image area size. The substrate sides before HTA was too flat to give any informative image results for larger surface areas than 1x1 μm^2.

For the hydrogen stabilized 8 μm membrane, the grain growth was more dominant on feed/growth side than on substrate/permeate side. The roughness increased from 21 nm to 30 nm on growth/feed side (10 x 10 μm^2) and from 0.4 nm to 0.9 nm on the substrate/permeate side (1 x 1 μm^2). The latter change shows that the membrane surface on substrate side remained flat. The AFM image for the

substrate side on this hydrogen stabilized membrane resembles the substrate side for the pulled-off membranes. The hydrogen stabilization leads therefore to a negligible grain growth on substrate/permeate side, whereas it did give an remarkable effect on growth/feed side. In figure 6.1 these changes in roughness on feed and permeate side are pictured and compared to permeability values. The roughness on permeate side is lower than on the feed side, also after the the treatments. Noteworthy is the low roughness on permeate side on sample C1 after HS. Why the protrusions are larger in lateral size after HS than after HTA is not known. However, how hydrogen flow through a membrane will affect the grain growth has not been reported or studied in relation to magnetron sputtered membranes before and is discussed later. Furthermore, the roughness on growth/feed side (10 x 10 μm^2) for sample B2 and C1 are 27.3 nm and 29.9 nm, respectively. This correlates with the image observations.
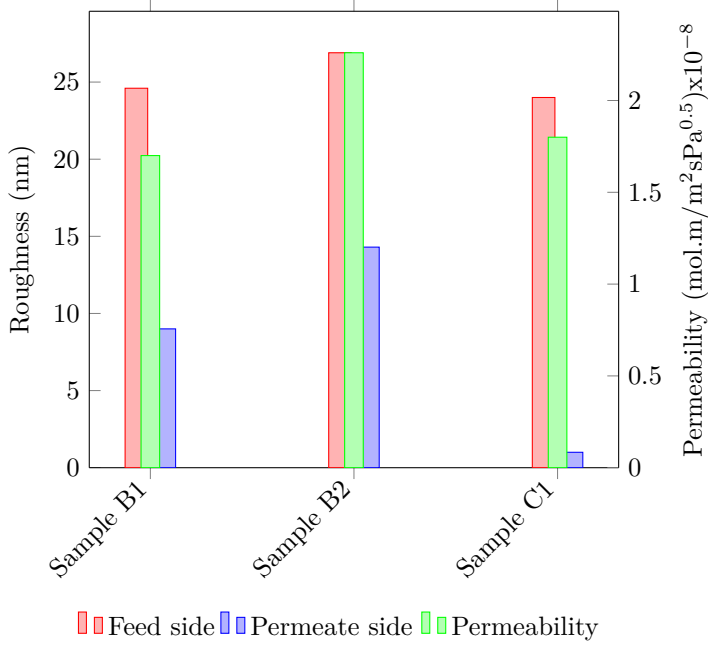
Figure 6.1: Diagram comparing surface roughness on feed and permeate side of a membrane with its permeability. The B samples have been heat treated in air while C1 has been hydrogen stabilized. The roughness values are taken from a 5x5 μm^2 image area size. The feed (red) and permeate (blue) bars belong to the roughness y-axis on the left hand side while the permeability values (green) belong to the y-axis on the right hand side.

AFM images of the Pd/Au membrane deviates remarkably from the 2.2 μm thick Pd/Agwt.23% membrane. The grain structure is much coarser and it is difficult do observe a surface structure in the images. The representation of the surface in the image is odd, which might refer to the irregularities with the tip during

investigation.

6.2 Permeation

The permeation is depending on various parameters. The observations of how these parameters affect the permeation capabilities of a membrane are discussed in the following subsections.

6.2.1 Pressure dependence

Figure 5.8 in chapter 5 shows an evident increase in flux with increasing pressure difference over the membrane. It is important to mention that the permeation measurements are taken over a relative small pressure difference. In this study the flux shows a linear dependence over pressure differences at 2-7 $kPa^{0.5}$, but this is not necessarily the case at higher pressure differences. For instance, Fort et al. reported linear flow rate dependence for a pressure difference up till 37.9 $kPa^{0.5}$, for measurements performed on a Pd/Ag25at.% membrane at 350 °C. Exceeding this pressure, the flow rate increased drastically [15]. How the permeation through the membrane develops for higher pressures is out of the scope of this work, though important to be aware of.

6.2.2 The n-value

To obtain a linear relationship for the flux as a function of difference in pressure (Pa), the correct n-value must be chosen. The n-value varies from whether the permeation process is limited by surface or bulk interactions. As mentioned in theory section 2.1, the n-value is assumed to be 0.5 whenever surface reactions are the rate-limiting step and 1 when bulk diffusion is the rate-limiting step. In order to evaluate the correct n-value, computations can be executed to find the best linear fit. In this study, only the two extremities (n=0.5 and n=1) have been compared. In figure 6.2 both n=1 and n=0.5 are applied for the flux data for the 4 μm thick Pd/Ag23wt.% membrane at 300 °C before heat treatment in air.

A 4 μm thick Pd/Ag23wt.% membrane is a quite thin membrane. When n=1 is used, the plot gives a linear fit for the pressure, whereas n=0.5 gives a slight bow. This indicates that surface effects play an important role as the rate limiting step for this permeation process. In general for the membrane thicknesses in question, small deviations for the two fits indicate that both surface effects and bulk diffusion are rate-limiting steps for the permeation process. The case for the 4 μm thick Pd/Ag23wt.% membrane before HTA in figure 6.2 is where surface effects as the rate-limiting step is the most expectable. This was the thinnest membrane tested in this work and for thin membranes surface effects are more crucial than bulk diffusion. Additionally, the surface effects are believed to play a larger role before
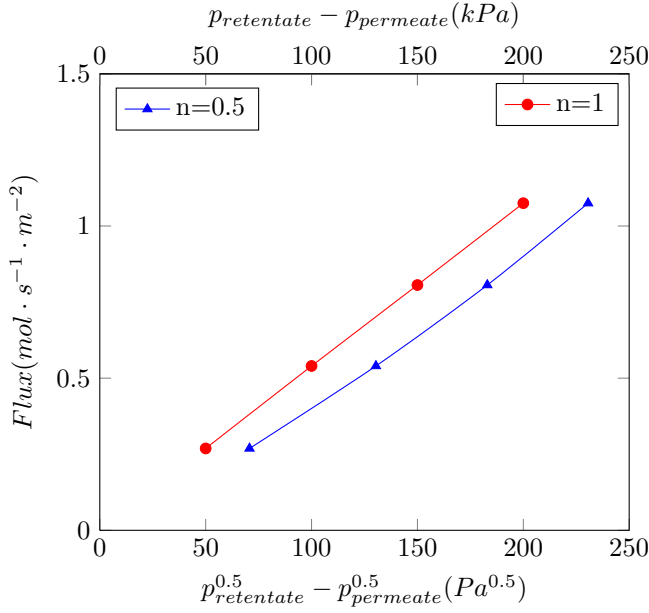
Figure 6.2: Results for 4 μm thick Pd/Ag23wt.% membrane at 300 °C. Both plots are for the flux before HTA. The red graph with circular markers has its reference x-axis on top, while the blue graph with triangular markers belongs to the bottom x-axis.

HTA than after [48]. Conclusively the differences in the plots are expected to decrease for the thicker membranes and for plots after heat treatment in air.

The n-value is important in order to compare permeance and permeability for different membranes. Calculations on these values should be based on the same n-value. The n-value 0.5 was chosen for all membranes, which also can be seen in the units for the calculated permeances and permeabilities, see table 5.3 and 5.4. In literature n=0.5 is commonly used. To be able to compare with previous estimated permeance and permeability results the same value is preferred. The permeance and permeability should be independent of the pressure for the right value of n. The permeance was calculated by taking the average of the fluxes divided by its respective pressure difference. The permeability is the permeance multiplied with the membrane thickness. A deviation from the correct n-value, will lead to deviations also in the permeance and permeability. The 4 μm thick Pd/Ag23wt.% membrane before HTA at 300 °C shown in figure 6.2, the permeability will be $1.7\text{x}10^{-8}$ $(mol.m/m^2 sPa^{0.5})$ for n=0.5 and $2.2\text{x}10^{-11}(mol.m/m^2 sPa)$ for n=1. This shows that the permeability strongly dependent on n and why the choice of a constant n-value would ameliorate the possibilities to compare the resulting permeance and permeability. It is important to have this in mind discussing the resulting permeance and permeability values.

6.2.3 Permeability

The permeability is in theory independent of thickness and considered a material constant. It should not deviate for membranes produced by the same technique. The permeability results in this work show different permeability for the membranes before heat treatment in air. The permeability values for one specific membrane at different temperatures are almost equal. The variation is observed from one membrane to another. A possible explanation is that the microstructure, surface or the composition differed. Comparing the permeance and permeability with values in literature, one observes that the values in this work is found to be both higher and lower than previous findings [48, 45]. This implies that difference in membrane microstructure and surface structure affect the permeation result. It is suggested that permeability of thinner membranes are often not reproducible due to surface effects, leakage through defects, flow of hydrogen across grain boundaries and lattice defects to mention some affecting parameters [49].

The change in permeability, e.g. sample B1, from before HTA to after HTA is clearly a result of alterations in microstructure and surface structure. Sample B2 does not show a striking change in permeability before and after HTA. Since sample B2 is thicker, this might indicate that HTA affects mostly the surface structure. The permeability before HTA for sample B2 is higher than both the permeability for sample B1 and C1 before HTA. All three should be equal in theory. Also, the sample B1 and B2 are from the same batch, so difference in microstructure as a result of production is not expected. One explanation could be that sample B2 had a unexpected change in microstructure or surface structure during hydrogen stabilization.

6.2.4 Thickness dependence

Permeance differences related to membrane thickness were observed. In theory the permeance should be double for a 4 μm thick membrane compared with a 8 μm thick membrane. The highest increase was on 84% which is not too far from the expected value. Comparing the increase with previous research [48], increase in a range of 50-84% is experimentally expected when comparing with membranes of half the thickness. In figure 6.3 the permeance for the two membranes of thickness 8 μm (sample B2 and C1) and the membrane of thickness 4 μm (sample B1) are plotted as a function of inverse thickness. The linear approximation with point of intersection in 0 is also shown. Its calculated R^2-value[1] is 0.82 which implies that the results show a fairly linear tendency. Still, this is reasonable for a very limited dataset.

---

[1] R^2 is always between 0 and 1 and describes how close the calculated values for the trendline are to the true data values. A trendline is more reliable when the R^2 value is close to 1.
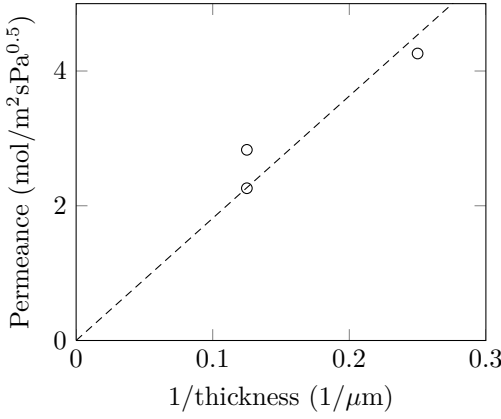
Figure 6.3: Permeance as a function of membrane thickness. Permeance results for sample B1 (4 μm), B2 (8 μm) and C1 (8 μm) before HTA are shown. A linear approximation with point of intersection in 0 is plotted as a dashed line to illustrate the deviations. The R^2 value is 0.82 for this linear fit.

6.2.5 Temperature dependence

The permeance variation with temperature is presented in figure 6.4. It is known
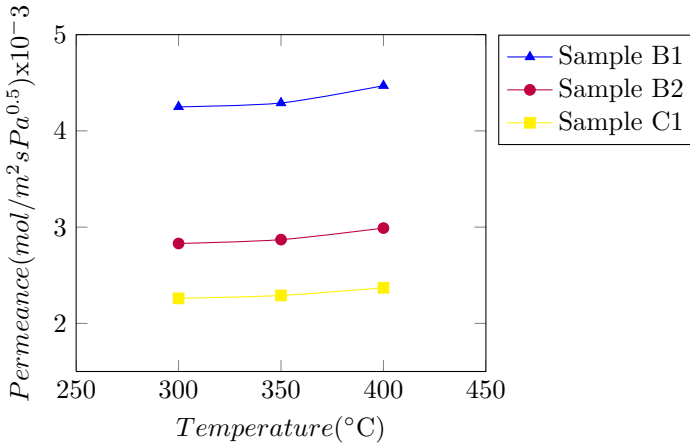
Figure 6.4: Permeance as a function of temperature is shown for 4 and 8 μm thick Pd/Ag23wt.% membranes before HTA.

that hydrogen permeability depends on both solubility and diffusivity, see equation 2.4. Both of these parameters are temperature dependent. The diffusion increase exponentially with temperature which can be seen in equation 2.5, whereas the solubility decrease [23, 50]. The calculated permeabilities for the membranes in

this work show this increase and are displayed in table 5.4. Since the permeance increases with temperature, the diffusion dependence of hydrogen overrule the solubility dependence. As shown in figure 6.4, the flux increased more at higher temperatures. This supports the observation of diffusion as the dominant temperature dependent parameter for the permeation.

6.2.6 Effect of treatments (HTA/HS)

In this section permeation results will be compared with the surface topography characterization of membranes that have been exposed to heat treatment in air or hydrogen stabilization.

The hydrogen permeation behavior after heat treatment in air showed an increase in flux for all membranes. This is also documented in previous research [48]. The extent of increase in permeance varied in these results which also is the case for previous findings [48]. The surface roughness on feed side for the 4 μm Pd/Ag membrane increased from $\sim$ 10 nm to $\sim$ 24 nm, while the relative increase in permeance was $\sim$+27%. For the 8 μm Pd/Ag membrane the roughness on feed side increased from $\sim$ 20 nm to $\sim$ 26 nm, while the relative increase in permeance was $\sim$+6%. This could be interpreted as an observed surface structure dependence for the permeation. The permeability should be a material constant independent of membrane thickness. This applies to membranes of equal composition and microstructure. The permeability for the heat treated membranes, $2.2\text{x}10^{-8}$ and $2.4\text{x}10^{-8}$ (mol.m/m^{2}sPa$^{0.5}$) at 300 °C, correlates with permeability values for membranes with same composition and after same treatment [48]. If the variations in permeability is small, the permeance will mainly vary as a function of thickness. This supports the theory of bulk diffusion as the rate controlling process for heat treated membranes.

Moreover, the AFM investigation showed higher surface roughness on both feed- and permeate side on the membranes after this heat treatment. Roughness reflects the underlying grain structures and an increase in roughness is thus a sign of grain growth within the polycrystalline membrane, which is observed and discussed earlier [47]. This corresponds with the observation in the AFM images. The roughness was higher on feed side than on permeate side after heat treatment in air. Comparing the roughness on these sides before treatment, the relative roughness has increased much more for the permeate side. An explanation of the large grain growth on permeate side is discussed by Tucho et al. [51, 47]. As seen in the Gibbs-Thomas relation, the grain growth process is affected by excess-free grain boundary energy. The substrate side has high density of grain boundaries as a deposition result and will therefore provide more excess-free energy under heating. This leads consequently to higher driving forces towards grain growth.

After the hydrogen stabilization, the roughness had increased vastly on feed side and less on permeate side. Since this experiment has been performed once, further investigations are needed to confirm this observation. However, given that it is

reproducible, an interesting question arise: Why does this hydrogen flux stabilization affect the feed side roughness more than the permeate side roughness? And first of all, why does the grains grow as a result of hydrogen exposure? Di Vece et al. have looked at why palladium nanoclusters grow as a result of hydrogen exposure [52]. Hydrogen absorbed in palladium lattice decreases the sublimation energy of the palladium. This leads to an increased probability for detachment of palladium atoms. Ostwald ripening will occur due to hydrogenation and free palladium atoms will bind to larger clusters. This explanation is based on pure Pd film and therefore not necessarily equivalent for Pd/Ag alloys. Furthermore, the explanation is based on nanocluster size, whereas the grains on our films are expected to be larger. Ramachandran et al. investigated surface roughness on feed and permeate side on membranes after either inert treatment or heat treatment in air [45]. Lack of correlation between roughness and permeability in these data are complicated by possible segregation phenomena occurring under N_2 exposure. The substrate and growth sides may have dissimilar onset temperatures for coarsening which will give unequal grain growth [47], but most observations, as well as thermodynamic relations, indicate that the strongest grain growth should be associated with smaller grains. Furthermore, Tucho et al. suggest that the temperature required for substantial grain growth lies between 400 °C and 450 °C.

Another observation is also interesting regarding the low roughness on permeate side after hydrogen stabilization. After heat treatment in air, only the roughness on permeate side increase remarkably. The roughness on feed side does not increase as much relatively. If the case was that the surface structure on permeate side has stronger influence on the permeance than the surface structure on feed side, this would be an interesting idea which needs more investigation. The objective with AFM investigation on HS membranes was to magnify surface structure alteration before and after HTA, which furthermore will need more exploration.

Permeability found for the hydrogen stabilized membrane, 1.8×10^{-8} (mol.m/m^{2}sPa$^{0.5}$) at 300 °C, is high compared to literature [48]. Larger deviation in the permeability for membranes before heat treatment is observed and whether the permeation is bulk controlled in this case is questionable [48]. The same trend for the permeance-inverse thickness relation cannot be clearly observed. If the permeation is partly surface controlled for thin hydrogen stabilized membranes, the low roughness on permeate side could have an effect on the desorption process of hydrogen.

The surface structure development seen in the images correlates with the roughening of the surface as mentioned earlier. A result of higher roughness, is increased total surface area, which further leads to increased number of sites available for disassociation/association of hydrogen. This may contribute to enhancement of the permeation [48]. Contradictory suggestions have been made on how hydrogen flux is related to grain growth. If there is grain growth on the surface, there is likely grain growth in the bulk as well. Grain growth in the membrane bulk has been reported to hamper the hydrogen flux [53], which is explained by a lower fraction of grain boundaries present. Hydrogen is assumed to diffuse along grain boundaries, so when these disappear, the flux is reduced. Change in grain size in bulk

is not documented in this work and will therefore not be further discussed. Grain growth has also been reported to increase the hydrogen permeance [54]. This is in accordance with observations in this work. The assumption of increased permeance from grain growth will be made, based on previous work and surface roughening.

This study reveals that surface modifications were more dominant on the thin membrane (4 μm) than for the thick one (8 μm). This corresponded with a higher flux increase for the thin membrane. This conclusion was also drawn by Mejdell et al. [48].

It is important to mention the discussed topic of possible palladium segregation to the surface as a result of these treatments. In addition, Zhang et al. discovered significantly enhanced H_2 sorption kinetics as a result of heat treatment in air [55]. However, these hypothesis will not be discussed any further, due to lack of surface composition analysis performed (e.g. X-ray photoelectron spectroscopy) and rate of adsorption analysis, which were out of the scope of this study.

6.3 Solubility

Equilibrium sorption measurements were performed twice at each temperature. The resulting isotherms, see appendix D, showed that reproducible results were obtainable. This fortifies the certainty of the results.

Sieverts' law given in equation 2.3, is true for diluted amounts of hydrogen. A high concentration of hydrogen atoms will result in a non ideal solution due to the attractive forces between the atomic hydrogen [56]. High pressures lead to high concentration. This will further create undiluted conditions which make Sieverts' law no longer valid. Some irregularities are observed in the sorption measurements at high pressures and can be explained with this restriction in Sieverts' law. Apart from this, the solubility showed linear dependence of the square root pressure implying valid conditions for Sieverts' law.

There is a definitive dependence of H_2 solubility on temperature. The solubility decreased as the temperature increased for all tested membranes. Sieverts' constant increased approximately 60-90% lowering the temperature from 400 °C to 300 °C. Such observations are demonstrated also in previous work [23, 57, 58]. When the binding energies of interstitial hydrogen atoms in a material are unfavorable with respect to gaseous H_2, the solubility of hydrogen atoms in this material will be low, even under relatively high pressures [59]. At high temperatures the gaseous state will be more favorable than the interstitial sites in the membrane.

At all temperatures, the graphs show an increase in volume uptake at the last data points. This indicates that K_S may increase with increasing pressure. In addition, lattice volume expansion as a result of large amounts of hydrogen present in the lattice, could explain this increase in hydrogen uptake. This expansion affects the binding energy of each hydrogen atom to an interstitial site [59]. By looking at the

sorption isotherms (see appendix C) in this work, one may observe an increase in hydrogen uptake in the last data points more frequently at $300\,°C$ than at $400\,°C$. The impact of hydrogen induced expansion is lower at higher temperatures, since the amount of hydrogen present in lattice is less compared to lower temperatures. This may be a reason for generally more modest solubility increase observed for the $400\,°C$ isotherms.

6.3.1 Hydrogen solubility in Pd/Ag membranes

In figure 5.10, a tendency of decreasing Sieverts' constants as a function of increasing membrane thickness is presented. The correlation between surface topography results from AFM and solubility results is discussed in this section.

The Sieverts' constants in this work are compared with other Sieverts' constants found in literature based on diffusivity and permeability data. These are listed in table 6.1.

Membrane	Temperature ($°C$)	K_S ($\mu mol/g.Pa^{0.5}$)	Reference
Pd/Ag25wt.%	350	0.51	[22] Zhang et al.
Pd/Ag20wt.%	350	0.58	[27] Holleck et al.
Pd/Ag20wt.%	317	0.55	[5] Grashoff et al.
Pd/Ag20wt.%	418	0.32	[5] Grashoff et al.
Pd/Ag23wt.%	282	0.82	[60] Bhargav et al.
Pd/Ag23wt.%	427	0.37	[60] Bhargav et al.

Table 6.1: Sieverts' constants calculated on palladium-silver membranes for various temperatures.

The K_S' estimated in this work are more similar to the K_S values found for the Pd/Ag23wt.% membrane from the article of Bhargav et al., than for the membranes with higher and lower silver compositions. The tendency for higher solubility at low temperatures is also observed for the K_S' found in literature. When comparing these values with the estimated values in this work, the best situation was if the membranes were of similar thickness in addition to equal composition. Comparing the K_S' calculated in Bhargav's article [60], where also a Pd/Ag23wt.% membrane was investigated, the values in this work are higher. This could be related to difference in thickness of the membranes. Another reason could be the manufacturing technique used in membrane production. In the making of thin palladium-silver membranes, several deposition conditions (e.g., technique, temperature, pressure, kinetic energy of the atoms) will affect the microstructure [61]. Different development in growth processes can give large deviations in the membrane's microstructure. For instance, the temperature on substrate during deposition will have an effect on surface diffusion of atoms condensed on substrate, which further may lead to a distinct grain growth. Such specific information is not given in the referred articles, consequently these uncertainties remains.

Zhang et al. performed sorption experiments on a 25 μm thick Pd/Ag25wt.% membrane. K_S equal to 0.51 μmol/g.Pa$^{0.5}$ was observed at 350 °C which is equal as the lowest Sieverts' constant found in this work at the same temperature. This value was measured for the 8 μm thick Pd/Ag23wt.% membrane. Zhang's membrane deviates in composition from the membranes used in this work. Furthermore, comparing K_S for the 25 μm thick Pd/Ag25wt.% membrane with K_S for a Pd/Ag20wt.% membrane of unknown thickness both at 350 °C, the K_S value is slightly higher for the membrane with lowest weight percent. Since the membrane thickness is unknown for one of the membranes, we have to be careful of what we conclude. However, the values are comparable at this temperature despite unequal composition.

Given ideal crystalline structure and uniform composition in the material, the result of decreasing K_S for thicker membranes is not expected. The roughness on growth side of the membranes increased with thickness, while solubility decreased. Assuming larger grains for higher roughness, supported by the qualitative observation in the images, there is a plausible connection between grain structure and solubility. The thickness dependence was more distinct at the lowest temperature than for the highest. That the membrane exerts better solubility capabilities at lower temperatures might be an explanation for this.

A deviation from the decreasing solubility for thicker membranes trend was noticeable for the 10 μm thick Pd/Ag23wt.% membrane. The resulting Sieverts' constants for this membrane were higher than for the 8 μm thick Pd/Ag23wt.% membrane at all temperatures. In fact, they were higher than the 8 μm thick membrane, yet lower than the 6 μm thick membrane. Topographic investigation on these three membranes showed correlating higher roughness values for the 8 μm thick membrane (20.4 nm) and lower roughness values for the 6 μm thick membrane (10.6 nm), whereas the 10 μm thick membrane showed a value in between (15.4 nm). The roughness values are representing an area of 5x5 μm^2, see table 5.1. If one assumes from these findings that the surface structure of the 10 μm thick membrane is in fact rougher than the 6 μm thick membrane, yet smoother than the 8 μm thick membrane, the "deviating" K_S values for the 10 μm thick membrane can be explained. This observation implies that the membrane structure and solubility trend may still be valid.

There is reason to believe that defects (e.g. grain boundaries, dislocations) as a result of thin film formation may enhance the solubility in the lattice. Enhancement in solubility as an effect of mechanical deformation in pure palladium was first reported by Flanagan et al. [30]. Since then, several papers have been published on the subject, where defects are made either by mechanical processing [62, 63] or by the $\alpha\rightarrow\beta$ phase transition [64]. In this work, such intentional deformation has not been executed. Instead, in the growth process of the membranes island formations will lead to higher density of grain boundaries close to the substrate-interface surface. As the membranes grow the islands will coalesce which leads to reduction of grain boundaries and dislocations. How the fraction of atoms associated with grain boundaries depend on grain size is shown in equation 2.15 in the theory section.

As described in theory section 2.3.2, the grain growth process will after some time create a more or less continuous film. In other words, the reduction in of grain boundaries will be more limited. At which thickness the grain boundary density alteration will be lessened is not unambiguous. Nevertheless, if solubility depends upon grain boundary density, there is reason to believe that there will be a flattening of the decrease in K_S as a function of thickness. That K_S for a 25 μm thick membrane [22] gives equal K_S as a 8 μm thick membrane, can be related to this possible development.

Bucur et al. did solubility measurements on palladium silver alloys with and without lattice defects. They wanted to see if palladium silver alloys showed the same solubility enhancement as pure palladium for the same degree of deformation, which they did [34]. The impact lattice defects have on solubility is mainly explained by the strain field model [32, 31, 65]. This model suggests that it is more favorable for the hydrogen atom to bind to a palladium atom where stresses in the lattice have extended the interstices about the atom core [31, 66]. However, the model does not satisfy for all conditions. At low hydrogen content the model does not give satisfactory calculations for the chemical potential [67] or the temperature dependence at high hydrogen concentration [31]. Bucur et al. suggested this could result from poor correlations with interaction energy values between hydrogen and Pd in vicinity of Pd-core dislocations. This is originally based on linear elasticity relationships. Improvement of the model could be done by deducing specific information on the thermodynamic parameters in interaction between hydrogen and different types of defects. Furthermore, Bucur et al. did deduce a relationship for the solubility isotherm where the concentration of possible traps in the lattice has been included [34]. In addition, research on how hydrogen interact with specific types of dislocations, which are described in theory section 2.3.4, have been published [32].

Other researchers have investigated how hydrogen may detect defects. Mütschele et al. used hydrogen as a probe to determine average grain boundary thickness [68]. In the grain boundaries regions the hydrogen will segregate, which is explained by the difference in site energies for grain boundaries and single crystals [69].

Finally, a verification of the estimated Sieverts' constants would be to use equation 2.4 and compute reasonable values of the diffusivity, D_H, from the obtained solubility and permeation data. The permeability, P [2], for the 4 μm thick membrane before HTA and the 8 μm thick hydrogen stabilized membrane, were divided on their Sieverts' constants found for the as-grown membranes with equal thicknesses. The results are displayed in table 6.2.

These values are comparable with the diffusivity data plotted in the article by Holleck [27]. In this article the data were based on measurements on a 0.11 cm thick Pd/Ag20at.% membrane.

In the calculation of D_H, the units of the Sieverts' constants had to be converted from (μmol/g.Pa$^{0.5}$) to (mol/m^{3}Pa$^{0.5}$), thus the material density (g/m^3) of Pd/Ag

---

[2]P is converted to mole atomic H

	$D_H = P/K_S \ (m^2/s)\mathrm{x}10^{-9}$		
	4 μm	8 μm	0.11 cm [27]
300 °C	3.1	4.4	2.1
350 °C	3.9	6.1	3
400 °C	5.1	7.8	4

Table 6.2: Calculated diffusion coefficients from obtained permeability (P) and solubility (K_S) values at different temperatures. The values are compared to previous research data by Holleck [27].

had to be utilized. As we know, this density depends on both temperature and hydrogen uptake in lattice and cannot be considered as a constant. Still, in this computation the density at room temperature was used which may lead to potential errors.

Influence in a larger context

If the results discussed in section 6.3.1 are correct, the question concerning possible equation modifications will arise. What is interesting to discuss is how the solubility dependence of thickness will affect the total permeation. In equation 2.4 the K_S is given as constant without thickness dependence. In the case of very thin membranes, the n-value is altered resulting in change overall flux. Since K_S also shows thickness dependence, a possible "n"-dependence for K_S will need to be taken into consideration. This could lead to a modification in equation 2.4. The n-value is an empirical exponent which is determined by adsorption/desorption processes on surface, bulk diffusion and the transitions phenomena surface-to-bulk and bulk-to-surface [70]. These elementary permeation steps depend on the feed and permeate hydrogen pressure as well as temperature. The sorption measurements showed that K_S will vary with temperature and thickness in the pressure range used in this study, whereas the temperature dependence was expected. The fact that the solubility shows a linear dependence of the square root of the pressure, supports the validity of Sieverts' law when bulk diffusion is the rate-limiting process. However, the question whether K_S needs to be made thickness dependent, $K_S(t)$, remains. A plausible outcome for such an adjustment could cause an increase in the permeability for thin membranes, which is defined by $P = D_H K_S$.

6.3.2 Hydrogen solubility in other palladium alloys

In figure 5.11 the Sieverts' constants for the three palladium alloys (PdAg, PdY and PdAu) with similar thicknesses are shown. The Pd/Ag23wt.% membrane had the highest solubility, followed by Pd/Y5at.% and then Pd/Au5at.% at the end. Given small variation in thickness, the differences in solubility are anticipated to be a result of alloy element and composition rather than surface structure variations.

Membrane	Temperature ($^\circ$C)	K_S (μmol/g.Pa$^{0.5}$)	Reference
Pd/Au10wt.%	350	0.16	[22] Zhang et al.
Pd/Au10wt.%	313	0.14	[5] Grashoff et al.
Pd/Au10wt.%	416	0.10	[5] Grashoff et al.
Pd/Au9wt.%	300	0.28	This work
Pd/Au9wt.%	350	0.22	This work
Pd/Au9wt.%	400	0.16	This work

Table 6.3: Sieverts' constants calculated on palladium-gold membranes for various temperatures.

Hughes et al. compared the hydrogen concentration for Pd/Y8at.% with Pd/Ag25at.% at 1 atmosphere pressure. This resulted in a higher hydrogen uptake for the Pd/Y alloy than the Pd/Ag alloy at 300 $^\circ$C, 350 $^\circ$C and 400 $^\circ$C, still the difference in uptake was very small [23]. Hughes et al. measured a hydrogen concentration (H/M) in Pd/Y8at% under 1 atm and 300 $^\circ$C to be approximately 0.13. In this work the hydrogen concentration in Pd/Y5at.% under 0.9 atm and 300 $^\circ$C was calculated to be 0.03 (H/M). The lower value is partly due to lower pressure in our measurement, which will lead to lower hydrogen uptake. A higher content of yttrium was used in the membranes investigated by Hughes et al. A higher yttrium content in Pd will improve the solubility (up till 12at.% [71]), hence better solubility for the Pd/Y8at.% membrane is anticipated. Structural variations in the membranes due to different manufacturing procedures are also a possibility.

In order to compare the K_S' for Pd/Au5at% with Pd/Au10wt.% from literature, the corresponding wt.% for the Pd/Au membrane in this work was calculated. This conversion gave Pd/Au9wt.%, which is fairly close to the weight percent for the membranes in literature. Comparison of the K_S values for the palladium-gold membrane with literature gives similar values. For Zhang et al. the resulting Sieverts' constant for a 25 μm thick membrane was 0.16 at 350 $^\circ$C whereas 0.22 was calculated in this work for a much thinner membrane. As mentioned before, the surface structure of this membrane is different compared to other thin palladium alloys, thus the solubility result is not certain. High surface roughness on the growth side of this membrane may resemble roughness measured on surfaces of thicker membranes. The small deviation in Sieverts' constant between this thin membrane and the 25 μm thick membrane could conclusively be an effect of similar surface structure. However, this is a very weak argument due to limited knowledge of the membrane structure for the palladium-gold membrane in this work.

A tendency of higher solubility for the Pd/Ag23wt.% membranes is observed, supporting that Pd/Ag23wt.% possesses good solubility capabilities. Indeed, high hydrogen solubility in palladium-silver compared to palladium-gold is also reported in previous literature [72, 5]. Lower hydrogen uptake in the PdY alloy than the PdAg alloy may be attributed to the non-optimal composition of Y in Pd. The differences in hydrogen uptake for the various palladium alloys can be explained by unequal volume in the lattices. When alloying pure palladium, the lattice constant

will change. For instance, addition of Cu causes cell contraction while the addition of Ag, Au and Y causes expansion of the Pd cell. Solubility increase with increasing alloy additive amount observed in previous research [5], can be explained by the increased size of the interstitial sites in the alloys. PdAg and PdAu exhibit a maximum on 30at.% and 20at.%, respectively [29]. For yttrium the maximum solid solubility in palladium is 12at.% [71]. This maximum indicates that the solubility in general depend on more than lattice size. At high hydrogen concentrations the solubility decrease with increasing silver/gold content. The explanation is believed to be an electronic effect, which will not be discussed any further [73].

6.4 Sources of error

6.4.1 Reliability on quantitative surface topography results

The particle analysis command for AFM gave large standard deviations for the output parameters, see table A.1 and A.2. There can be several sources of error for this. First of all, the command is preferred used on well isolated particles. That is not the case for the samples in this work. The threshold height, as mentioned in section 4.1.2, was set at a z-height where most particles were found. The height histogram shows that some particles may be found below this height and some above. It also shows a larger height span for the particles above the threshold height than below. Having a large standard deviation in the mean height parameter, indicates vast deviation in z-height for particles grown above "standard" particle height. A section of sample A5 demonstrates the origin for large standard deviation in mean area. The threshold height will intersect both the top of lower grains and the lower areas of grains that have partly coalesced. For the lower grain, the software will calculate a very small surface area. For the partly coalesced grains, this will be interpreted as a very large grain. The area of intersection can be referred to as a mask. The area calculated gives the surface area covered by the "mask", for each region in the image. It includes all data that is higher than the threshold value [74]. Since the particles are not well isolated, we might include several grains or just a scalp of a grain in this mask. Such large deviations can explain the large standard deviation for the mean area output parameter. For the following heights above the mask, the large standard deviation might decrease since the mask will cover fewer grains with smaller areas. Overall, the total large standard deviation stays put. Having large standard deviation does not mean the output parameters are wrong, but the values cannot be fully trusted. Awareness of such errors may help understanding the deviations and to what extent the numbers can be trusted.

The RMS values might as well be a satisfactory choice of quantitative approach for grain growth on membranes. The images give a qualitative perception of how the grains grow for increasing membrane thickness. This correlates to the observed increased RMS values. Together, these observations can be used to assume grain growth.

(a) Example of a height histogram.

(b) Example of a section graphic through a surface.
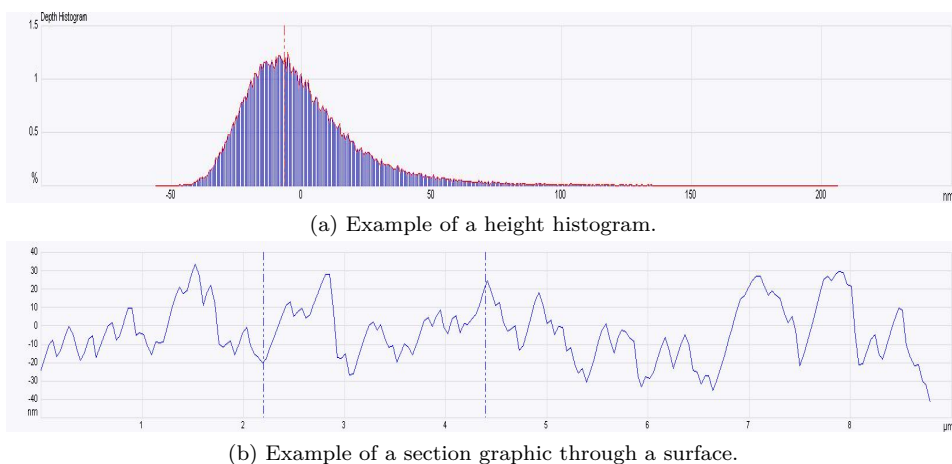
Figure 6.5: The examples are taken from the 10 μm Pd/Ag23wt.% membrane at the same location.

6.4.2 Sources of error for 10 μm Pd/Ag membrane

Deviation in the results for the 10 μm Pd/Ag membrane was observed in several investigation. The roughness estimations, AFM images and the equilibrium sorption measurement gave results for the membrane that did not correlate with the observed trends. After looking into the point of time the Pd/Ag membranes were made, it turns out that the 4, 6 and 8 μm thick membranes were made in January 2012, while the 10 μm was made in August 2011, so it is not from the same batch. This could be a source of error if modifications or servicing have been done on the instrument in this period of time.

6.4.3 Sources of error in equilibrium sorption measurements

Sorption methods of hydrogen are discussed in research literature [75, 76]. Various parameters as temperature, pressure, volume and sample weight may affect the analysis result. In this work a volumetric technique was chosen over a gravimetric technique, in which the latter method measures the change in sample weight due to the gas uptake. Uncertainty in gravimetric measurements can be related to the very light weight of hydrogen atoms. The volumetric technique is therefore preferred, yet this method has its drawbacks. Qajar et al. showed that an error of 0.1% in the measurement of either sample cell or reference cell volume with helium-free space, led to approximately a 3% error in the hydrogen uptake measurement. Still, it is important to point out that in this related study adsorption of hydrogen was measured and not ad-/absorption as done in this work. Equilibrium sorption will lead to higher gas uptake which will reduce this source of error.

The change in sample weight as a result of degassing during sample preparation can lead to uncertainty in the hydrogen uptake. Removal of surface oxide, moisture and possible CO_2 on the sample may lead to weight reduction. The weight was measured for the second time after the sorption measurement at $400\,^{\circ}\text{C}$. Even though the sample was transported from the instrument to the weighing chamber, much of the oxide layer on the sample is expected to be removed. This is because the time for which the sample is exposed to air after measurement is shorter than before. How much of the oxide layer and other compounds that is removed after the first isotherm sorption measurement is not known. The correct sample weight after $300\,^{\circ}\text{C}$ and $350\,^{\circ}\text{C}$ is therefore uncertain. The reduction in sample weight and the total sample weight varied from 2-6x10^{-3}g and ~0.08-0.12 g, respectively. How large error the sample weight might give depends on the total sample weight. A weight error of 3% as proposed by Qajar et al., is plausible also in this work. However, a weight error of this order is negligible compared to a leakage in the system or error in the volume estimation of the hydrogen uptake. What supports the results in this work, is the reproducibility of the equilibrium sorption isotherms.

Chapter 7

Conclusion

Solubility measurements on Pd/Ag23wt.% membranes in a thickness range of 2.2-10 μm showed different hydrogen uptake capabilities. Equilibrium sorption measurements performed at equal conditions for temperature and pressure, resulted in an increase in solubility for the thinner membranes in comparison with the thicker membranes. Larger grains were observed for the thicker membranes when surface topography investigation on growth side of as-grown (and further pulled-off) Pd/Ag23wt.% membranes was performed. Growth of larger grains constituting the surface topography as a result of increased membrane thickness was hence observed. Correlating trends of surface structure and solubility variations, implies that the solubility capabilities of the membrane depend on membrane structure. A possible hypothesis/interpretation, that also has been mentioned in the literature, is that the grain boundaries facilitate hydrogen sorption. This is in accordance with higher density of grain boundaries across the thinner membranes in this study. However, thorough surface- and microstructural investigations have to be carried out for definite conclusions of this dependence. Furthermore, the Sieverts' constants at different temperatures were calculated and compared to literature. The Sieverts' constants for the thicker membranes were comparable with those found in previous work.

A pronounced temperature dependence was observed for all membranes, that is, high solubility at low temperatures and vice versa for high temperatures. This is consistent with previously reported solubility hypothesis and results. Differences in binding energy for the hydrogen atom is assumed to be the cause. At high temperatures it is more favorable for the hydrogen atom to form gaseous H_2 than to bond to the interstitial sites in the material.

Various palladium-based alloy membranes (PdAg, PaAu and PdY) with similar thicknesses, demonstrated different hydrogen uptake capabilities. Also for these membranes, the solubility measurements were performed for equal temperature and pressure conditions. PdAg showed the highest hydrogen uptake closely followed

by the hydrogen uptake measured for PdY. A much lower hydrogen uptake was observed for the PdAu membrane. These solubility results indicate first of all dependence of type of alloying element, but also the amount of alloying element is of significance. The extent of impact these types of alloying elements have on the original Pd lattice, may further be related to solubility properties for the respective alloy.

Membranes of thickness 4 and 8 μm thick Pd/Ag23wt.% were investigated before and after heat treatment in air at $300\,^\circ$C. An increase in flux through the membranes was demonstrated for both membranes after this heat treatment. Surface topography investigations implied grain growth on feed/growth side and permeate/substrate side as a result of the heat treatment for both of the membranes. Furthermore, the study revealed that surface modifications were more dominant on the thin membrane (4 μm) than for the thick one (8 μm), which corresponded with the higher flux increase for the thinner membranes. Surface investigation on a hydrogen stabilized a 8 μm thick Pd/Ag23wt.% membrane showed grain growth on feed/growth side, whereas the surface alteration on permeate/substrate side was almost not detectable. There was no distinctive increase in permeation registered as a result of this grain growth on feed/growth side after hydrogen stabilization.

Sources of error must be considered when interpreting the results. Sorption technique errors, manufacturing errors and making wrong assumptions related to surface structure will affect the result.

Finally, the hydrogen permeation is a complex function of many parameters. In this work parameters such as, hydrogen pressure, temperature, material composition, membrane thickness and surface structure have demonstrated their influence on the membranes solubility and/or permeation abilities.

Chapter 8

Suggestions for further work

Concerning how the hydrogen atoms act in the presence of defects, a model of the hydrogen-defect interaction could provide better knowledge. This interaction between a hydrogen atom and a defect in a Pd/Ag lattice and in pure Pd lattices are of interest. This model could be based on the interaction between hydrogen in grain boundaries and certain dislocations. Also rate of adsorption experiments on membranes of different thickness, or even a single crystal, would be interesting for improved comprehension on the solubility in pure palladium and palladium alloys.

To see if Sieverts' constant has the same thickness dependence for other palladium alloys, sorption measurements on more membrane thicknesses will have to be done. Sorption measurements on pure palladium membranes of different thicknesses are of interest. Since so much research is already done on pure palladium, there exists plenty of research material which can be related to the results and help explain them.

Bibliography

[1] Rune Bredesen, TA Peters, and M Stange. Palladium-based Membranes in Hydrogen Production. *pubs.rsc.org*, 2:40–86, 2011.

[2] Angelo Basile. Hydrogen Production Using Pd-based Membrane Reactors for Fuel Cells. *Topics in Catalysis*, 51(1-4):107–122, October 2008.

[3] Daniel R Palo, Robert A Dagle, and Jamie D Holladay. Methanol steam reforming for hydrogen production. *Chemical reviews*, 107(10):3992–4021, October 2007.

[4] V Goltsov. From hydrogen economy to hydrogen civilization. *International Journal of Hydrogen Energy*, 26(9):909–915, September 2001.

[5] By G J Grashoff, C E Pilkington, and C W Corti. The purification of hydrogen. *Discovery*, 27(4):157–169, 1983.

[6] Ing.Steffen Wieland, Ing.Thomas Melin, and Ing.A. Lamm. Membrane reactors for hydrogen production. *Chemical Engineering Science*, 57(9):1571–1576, May 2002.

[7] A.L. Athayde, R.W. Baker, and P. Nguyen. Metal composite membranes for hydrogen separation. *Journal of Membrane Science*, 94(1):299–311, September 1994.

[8] A.L. Mejdell, D. Chen, T.A. Peters, R. Bredesen, and H.J. Venvik. The effect of heat treatment in air on CO inhibition of a 3μm PdAg (23wt.%) membrane. *Journal of Membrane Science*, 350(1-2):371–377, March 2010.

[9] A.L. Mejdell, M. Jø ndahl, T.A. Peters, R. Bredesen, and H.J. Venvik. Effects of CO and CO2 on hydrogen permeation through a 3μm Pd/Ag 23wt.% membrane employed in a microchannel membrane configuration. *Separation and Purification Technology*, 68(2):178–184, August 2009.

[10] Francesco Scura, Giuseppe Barbieri, and Enrico Drioli. H2 for PEM-FC: effect of CO in the purification by means of Pd-based membranes. *Desalination*, 200(1-3):239–241, November 2006.

[11] H. Klette and R. Bredesen. Sputtering of very thin palladium-alloy hydrogen separation membranes. *Membrane Technology*, 2005(5):7–9, May 2005.

[12] Rune Bredesen and Hallgeir Klette. Method of manufacturing thin metal membranes - US Patent 6086729 Abstract, 2000.

[13] Thomas Graham. On the Absorption and Dialytic Separation of Gases by Colloid Septa. *Phil. Trans. R. Soc (London)*, 156:399, 1866.

[14] F.A. Lewis. *The Palladium hydrogen system*. Academic Press, New York, 1967.

[15] D. Fort, J.P.G. Farr, and I.R. Harris. A comparison of palladium-silver and palladium-yttrium alloys as hydrogen separation membranes. *Journal of the Less Common Metals*, 39(2):293–308, February 1975.

[16] R. Feenstra, D.G. de Groot, R. Griessen, J.P. Burger, and A. Menovski. Absorption of hydrogen in Pd-Co and Pd-U alloys. *Journal of the Less Common Metals*, 130:375–386, March 1987.

[17] A. C. Makrides. Absorption of Hydrogen by Silver–Palladium Alloys. *Journal of Physical Chemistry*, 68(8):2160–2169, August 1964.

[18] A Fazle Kibria. The effect of alloying of palladium with silver and rhodium on the hydrogen solubility, miscibility gap and hysteresis. *International Journal of Hydrogen Energy*, 25(9):853–859, September 2000.

[19] Shigeyuki Uemiya, Takeshi Matsuda, and Eiichi Kikuchi. Hydrogen permeable palladium-silver alloy membrane supported on porous ceramics. *Journal of Membrane Science*, 56(3):315–325, March 1991.

[20] TL Ward and Tien Dao. Model of hydrogen permeation behavior in palladium membranes. *Journal of Membrane Science*, 153(January 1998):211–231, 1999.

[21] Diran Basmadjian. *Mass transfer and separation processes : principles and applications*. 2007.

[22] Ke Zhang, Sabina K. Gade, and J. Douglas Way. Effects of heat treatment in air on hydrogen sorption over PdAg and PdAu membrane surfaces. *Journal of Membrane Science*, 403-404(2010):78–83, June 2012.

[23] DT Hughes and IR Harris. A comparative study of hydrogen permeabilities and solubilities in some palladium solid solution alloys. *Journal of the Less Common Metals*, 61, 1978.

[24] R. P. H. Gasser. *An introduction to chemisorption and catalysis by metals*. Oxford Science Publications, New York, 1985.

[25] C Wagner. Hysteresis phenomena in the system palladium-hydrogen and in rotational transitions. *Zeitschrift fur Physikalische Chemie*, 1944.

[26] G Alefeld and J. Völkl. *Hydrogen in metals 1*. Springer, Berlin, 1978.

[27] G L Holleck. Diffusion and solubility of hydrogen in palladium and palladiumsilver alloys. *Journal of Physical Chemistry*, 74(3):503–511, 1970.

[28] R. H. Fowler. A Theoretical Formula for the Solubility of Hydrogen in Metals. *Proc. R. Soc*, 160:37–47, 1937.

[29] Chandrashekhar G Sonwane, Jennifer Wilcox, and Yi Hua Ma. Solubility of hydrogen in PdAg and PdAu binary alloys using density functional theory. *The journal of physical chemistry. B*, 110(48):24549–58, December 2006.

[30] TB Flanagan and JF Lynch. The effects of lattice defects on hydrogen solubility in palladium I. Experimentally observed solubility enhancements and thermodynamics of absorption*. *. . . the Less Common Metals*, 49:13–24, 1976.

[31] Ted Flanagan and J. F. Lynch. The effects of lattice defects on hydrogen solubility in palladium II. Interpretation of solubility enhancements*. 49:25–35, 1976.

[32] W.G. Wolfer and M.I. Baskes. Interstitial solute trapping by edge dislocations. *Acta Metallurgica*, 33(11):2005–2011, November 1985.

[33] S Kishimoto, N Yoshida, and T Hiratsuka. Dislocation-enhanced hydrogen solubilities in Pd-Ni, Pd-Ag and Pd-Ni-Ag alloys. *Scripta Metallurgica et materiala*, 30(c):643–647, 1994.

[34] RV Bucur, NO Ersson, and XQ Tong. Solubility and diffusivity of hydrogen in palladium and Pd 77 Ag 23 containing lattice defects. *Journal of the Less Common Metals*, 74:748–758, 1991.

[35] Milton Ohring. *The Materials Science of Thin Films.* 1992.

[36] John A. Venables. *Introduction to Surface and thin film processes.* Cambridge University Press, 2000.

[37] John L. Vossen and Werner Kern. *Thin film processes.* Academic Press Inc., 1978.

[38] G. Binnig and C. F. Quate. Atomic Force Microscope. *Physical Review Letters*, 56(9):930–933, March 1986.

[39] Astrid Lervik Mejdell. Thickness dependent behaviour of palladium-silver membranes. Technical report, January 2004.

[40] Marit Sletmoen, Catharina de Lange Davies, and Bjørn T. Stokke. *Biophysical Nanotechnologies.* Biophysics and Medical Technology, Dept. of Physics, NTNU, Trondheim, 2011.

[41] A.L. Mejdell, T.A. Peters, M. Stange, H.J. Venvik, and R. Bredesen. Performance and application of thin Pd-alloy hydrogen separation membranes in different configurations. *Journal of the Taiwan Institute of Chemical Engineers*, 40(3):253–259, May 2009.

[42] NanoScope Software Version 7.2.

[43] A.L. Mejdell, M. Jondahl, T.A. Peters, R. Bredesen, and H.J. Venvik. Experimental investigation of a microchannel membrane configuration with a $1.4\mu m$ Pd/Ag23wt.% membrane. Effects of flow and pressure. *Journal of Membrane Science*, 327(1-2):6–10, February 2009.

[44] F.A. Lewis. The Hydrides of Palladium and Palladium Alloys. (4):132–137, 1960.

[45] A Ramachandran, W.M. Tucho, A.L. Mejdell, M. Stange, H.J. Venvik, J.C. Walmsley, R. Holmestad, R. Bredesen, and A. Borg. Surface characterization of Pd/Ag23wt% membranes after different thermal treatments. *Applied Surface Science*, 256(20):6121–6132, August 2010.

[46] Wakshum Mekonnen, Bjornar Arstad, Hallgeir Klette, John C. Walmsley, Rune Bredesen, Hilde Venvik, and Randi Holmestad. Microstructural characterization of self-supported $1.6\mu m$ Pd/Ag membranes. *Journal of Membrane Science*, 310(1-2):337–348, March 2008.

[47] W. M. Tucho, H. J. Venvik, J. C. Walmsley, M. Stange, A. Ramachandran, R. H. Mathiesen, A. Borg, R. Bredesen, and R. Holmestad. Microstructural studies of self-supported (1.5-10 μm) Pd/23wt%Ag hydrogen separation membranes subjected to different heat treatments. *Journal of Materials Science*, 44(16):4429–4442, June 2009.

[48] A.L. Mejdell, H. Klette, A. Ramachandran, A. Borg, and R. Bredesen. Hydrogen permeation of thin, free-standing Pd/Ag23% membranes before and after heat treatment in air. *Journal of Membrane Science*, 307(1):96–104, January 2008.

[49] N.M. Peachey, R.C. Snow, and R.C. Dye. Composite PdTa metal membranes for hydrogen separation. *Journal of Membrane Science*, 111(1):123–133, March 1996.

[50] F. A. Lewis. Solubility of hydrogen in metals. *Pure and Applied Chemistry*, 62(11):2091–2096, 1990.

[51] C. C. Koch, R. O. Scattergood, K. A. Darling, and J. E. Semones. Stabilization of nanocrystalline grain sizes by solute additions. *Journal of Materials Science*, 43(23-24):7264–7272, July 2008.

[52] M. Di Vece, D. Grandjean, M. Van Bael, C. Romero, X. Wang, S. Decoster, a. Vantomme, and P. Lievens. Hydrogen-Induced Ostwald Ripening at Room Temperature in a Pd Nanocluster Film. *Physical Review Letters*, 100(23):236105, June 2008.

[53] H Natter, B Wettmann, B Heisel, and R Hempelmann. Hydrogen in nanocrystalline palladium. *Journal of Alloys and Compounds*, 253-254:84–86, May 1997.

[54] B. A. Mc Cool and Y.S. Lin. Nanostructured thin palladium-silver membranes: Effects of grain size on gas permeation properties. *Journal of Materials Science*, 36(13):3221–3227, 2001.

[55] Ke Zhang, Sabina K. Gade, Ø yvind Hatlevik, and J. Douglas Way. A sorption rate hypothesis for the increase in H2 permeability of palladium-silver (Pd/Ag) membranes caused by air oxidation. *International Journal of Hydrogen Energy*, 37(1):583–593, January 2012.

[56] Bryan D. Morreale, Michael V. Ciocco, Robert M. Enick, Badi I. Morsi, Bret H. Howard, Anthony V. Cugini, and Kurt S. Rothenberger. The permeability of hydrogen in bulk palladium at elevated temperatures and pressures. *Journal of Membrane Science*, 212(1-2):87–97, February 2003.

[57] H. Wipf. *Hydrogen in metals*. Springer-Verlag, Berlin, 1997.

[58] D. Fort and I.R. Harris. The physical properties of some palladium alloy hydrogen diffusion membrane material. *Journal of the Less Common Metals*, 41(2):313–327, July 1975.

[59] Sunggu Kang, Shiqiang Hao, and DS Sholl. Using First-principles Models to Advance Development of Metal Membranes for High Temperature Hydrogen Purification. . . . *Polymeric and Composite Membranes . . .* , 14:309–331, 2011.

[60] Atul Bhargav and Gregory S. Jackson. Thermokinetic modeling and parameter estimation for hydrogen permeation through Pd0.77Ag0.23 membranes. *International Journal of Hydrogen Energy*, 34(12):5164–5173, June 2009.

[61] Milton Ohring. *The Materials Science of Thin Films*. 1992.

[62] Y Sakamoto, S Hirata, and H Nishikawa. Diffusivity and solubility Pd-Au Alloys. *Journal of the Less-Common Metals*, 88:387–395, 1982.

[63] S Kishimoto and N Yoshida. Solution of hydrogen in cold-worked and annealed Pd-Ag alloys. *Scripta Metallurgica et materiala*, 25:877–881, 1991.

[64] R.V. Bucur and E. Indrea. Influence of the crystalline microstructure on the diffusivity of hydrogen in palladium galvanostatic permeation and X-ray diffraction measurements. *Acta Metallurgica*, 35(6):1325–1332, June 1987.

[65] Ted B. Flanagan, J.F. Lynch, J.D. Clewley, and B. von Turkovich. Hydrogen solubility as a probe for monitoring recovery in palladium. *Scripta Metallurgica*, 9(10):1063–1068, October 1975.

[66] A.H Cottrell. Theory of dislocations. *Progress in Metal Physics*, 1:77–126, January 1949.

[67] R. Kirchheim. Interaction of hydrogen with dislocations in palladium-II. Interpretation of activity results by a fermi-dirac distribution. *Acta Metallurgica*, 29(5):845–853, May 1981.

[68] T Mütschele and R Kirchheim. Hydrogen as a probe for the average thickness of a grain boundary. *Scripta metallurgica*, 21(c):4–7, 1987.

[69] T. Mütschele and R. Kirchheim. Segregation and diffusion of hydrogen in grain boundaries of palladium. *Scripta Metallurgica*, 21(2):135–140, February 1987.

[70] Alessio Caravella, Francesco Scura, Giuseppe Barbieri, and Enrico Drioli. Sieverts law empirical exponent for Pd-based membranes: critical analysis in pure H2 permeation. *The journal of physical chemistry. B*, 114(18):6033–47, May 2010.

[71] I.R. Harris and M. Norman. The electronic state of cerium in some palladium alloys. *Journal of the Less Common Metals*, 15(3):285–298, July 1968.

[72] A. G. Knapton. Palladium Alloys for Hydrogen Diffusion Membranes | Platinum Metals Review. *Platinum Metals Rev*, 21(2):44–50, 1977.

[73] TB Flanagan and WA Oates. The palladium hydrogen system. *Annual Review of Materials Science*, pages 269–304, 1991.

[74] Email correspondence with Chris Gregory. Applications Scientist. Nano Surfaces division in Bruker UK Limited. 2013.

[75] Ali Qajar, Maryam Peer, Ramakrishnan Rajagopalan, and Henry C. Foley. High pressure hydrogen adsorption apparatus: Design and error analysis. *International Journal of Hydrogen Energy*, 37(11):9123–9136, June 2012.

[76] T.P. Blach and E.MacA. Gray. Sieverts apparatus and methodology for accurate determination of hydrogen uptake by light-atom hosts. *Journal of Alloys and Compounds*, 446-447:692–697, October 2007.

Appendix A

Topographic surface results

A.1 AFM image results

A.1.1 Growth/feed side

Sample A1-A5

(a) 1x1 μm^2

(b) 1x1 μm^2

(c) 5x5 μm^2

(d) 5x5 μm^2

(e) 10x10 μm^2

(f) 10x10 μm^2
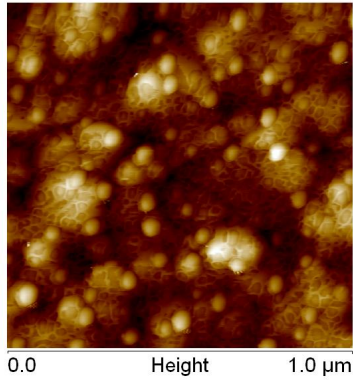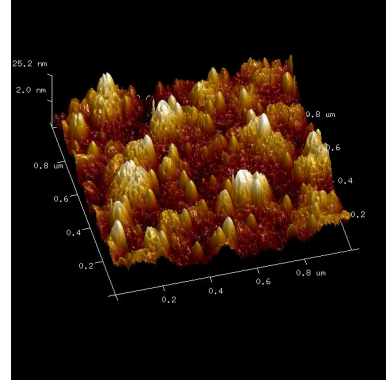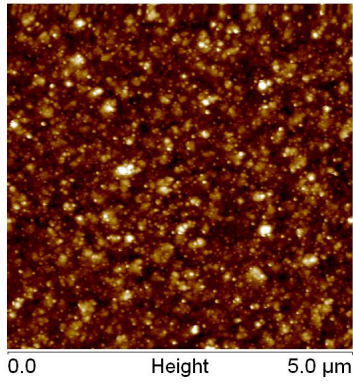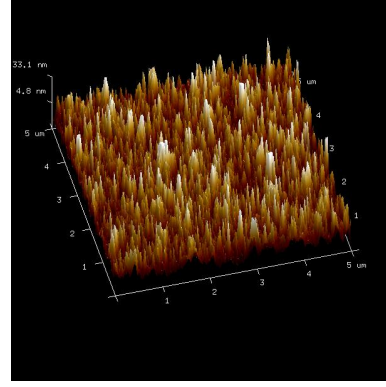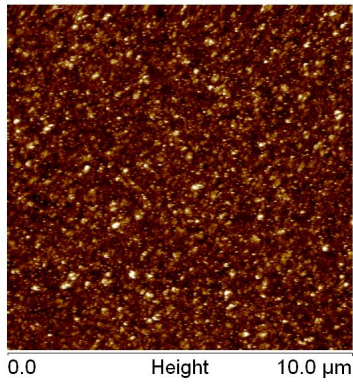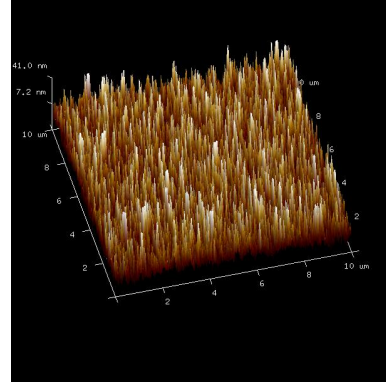
Figure A.1: 2 μm thick Pd23wt.%Ag (Sample A1). AFM images of the feed side in 2D (a, c, e) and in 3D modified images (b, d, f).

(a) 1x1 μm^2

(b) 1x1 μm^2

(c) 5x5 μm^2

(d) 5x5 μm^2

(e) 10x10 μm^2

(f) 10x10 μm^2
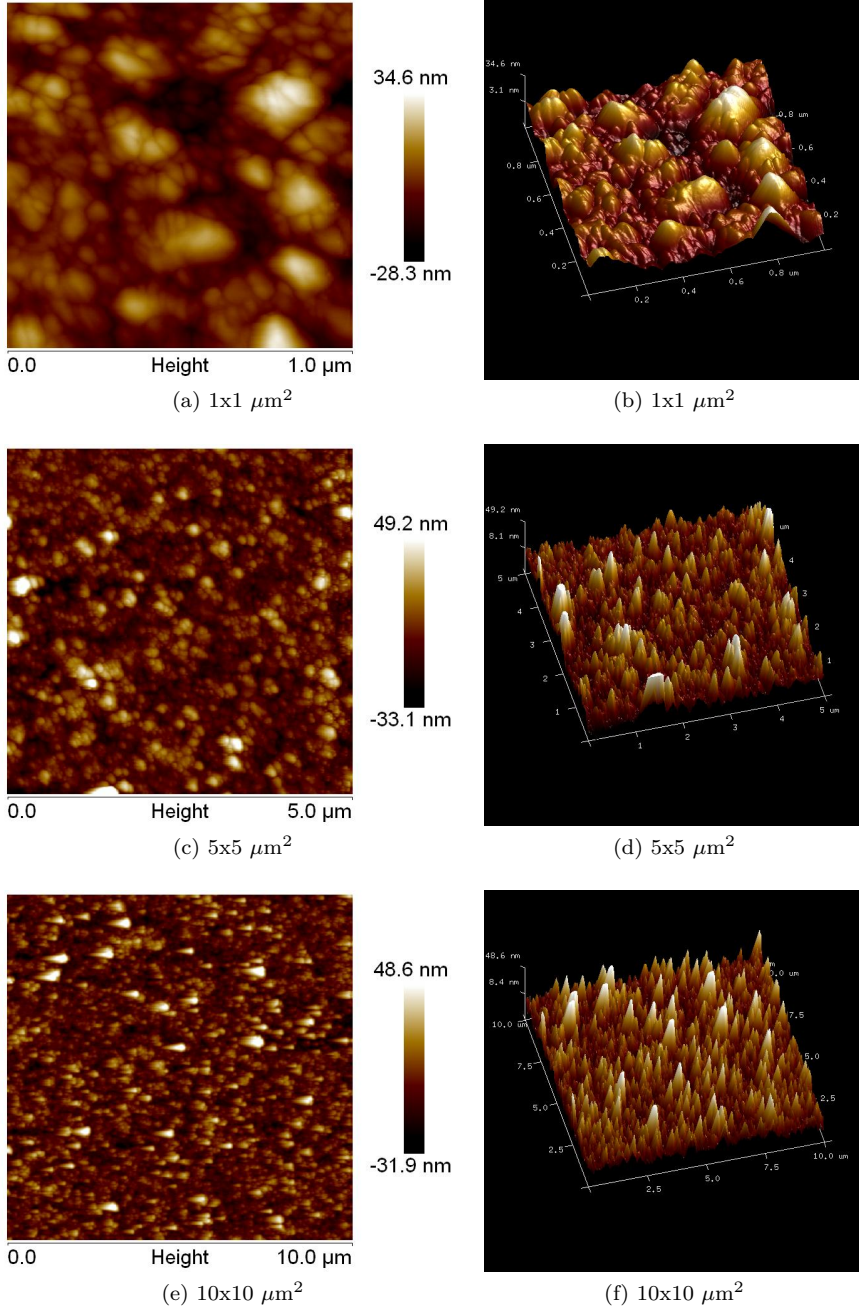
Figure A.2: 4 μm thick Pd23wt.%Ag (Sample A2). AFM images of the feed side in 2D (a, c, e) and in 3D modified images (b, d, f).

(a) 1x1 μm^2

(b) 1x1 μm^2

(c) 5x5 μm^2

(d) 5x5 μm^2

(e) 10x10 μm^2

(f) 10x10 μm^2
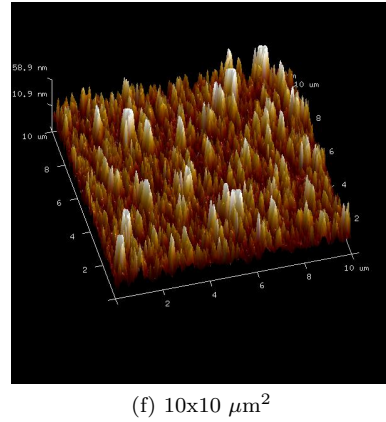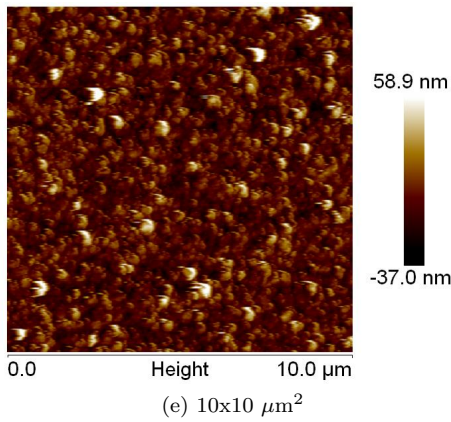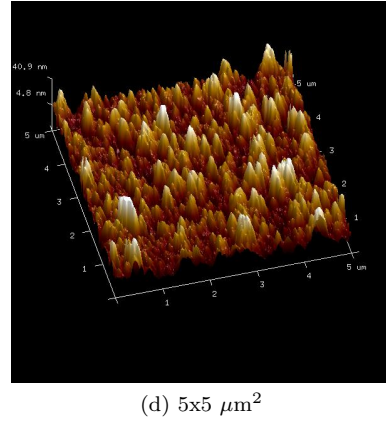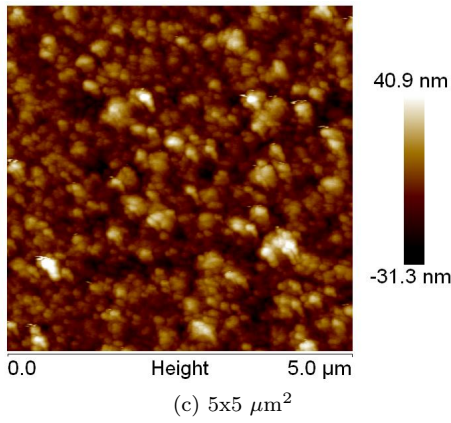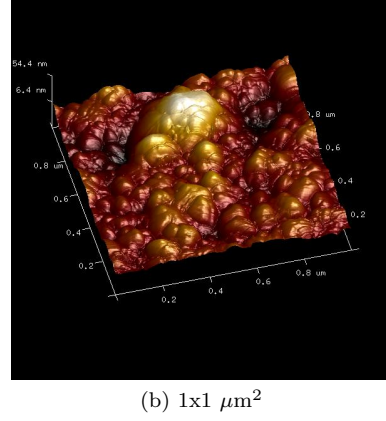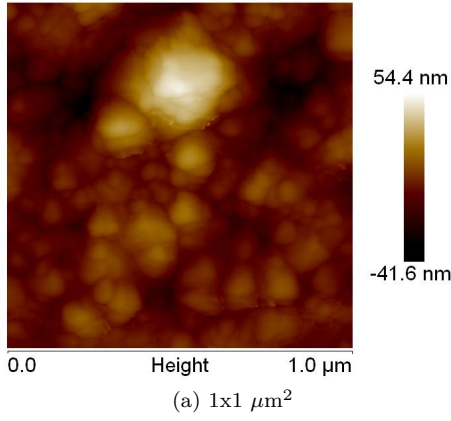
Figure A.3: 6 μm thick Pd23wt.%Ag (Sample A3). AFM images of the feed side in 2D (a, c, e) and in 3D modified images (b, d, f).

(a) 1x1 μm^2

(b) 1x1 μm^2

(c) 5x5 μm^2

(d) 5x5 μm^2

(e) 10x10 μm^2

(f) 10x10 μm^2
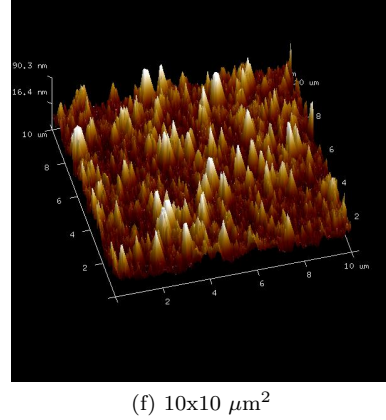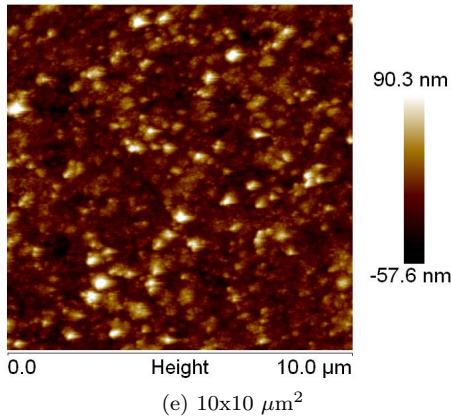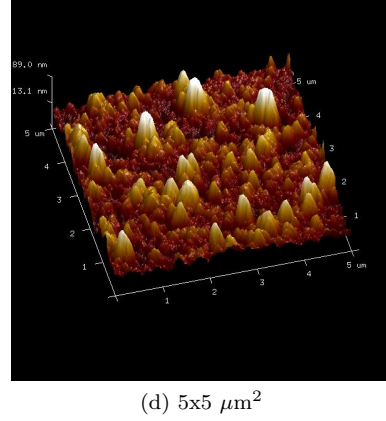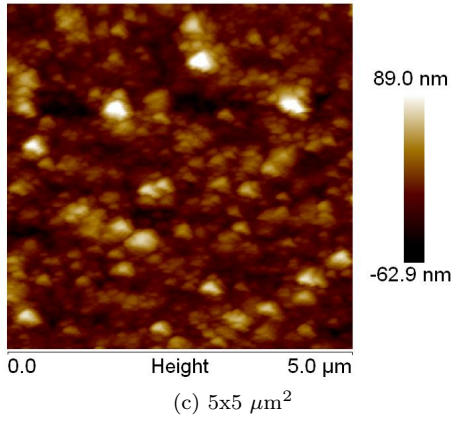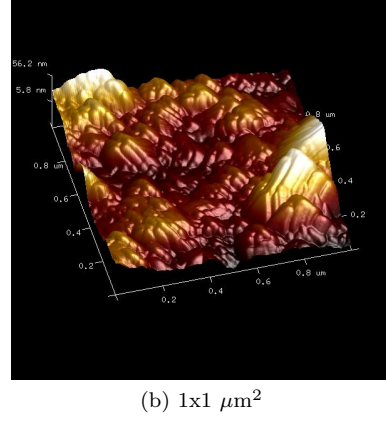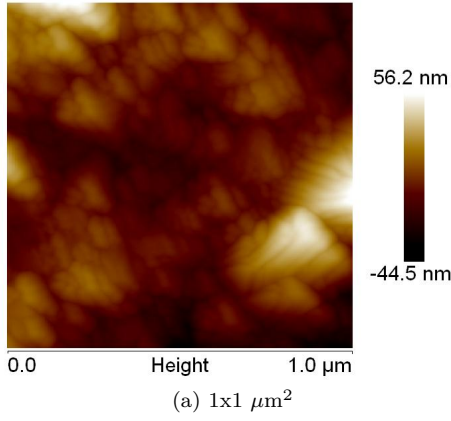
Figure A.4: 8 μm thick Pd23wt.%Ag (Sample A4). AFM images of the feed side in 2D (a, c, e) and in 3D modified images (b, d, f).

(a) 1x1 μm^2

(b) 1x1 μm^2

(c) 5x5 μm^2

(d) 5x5 μm^2

(e) 10x10 μm^2

(f) 10x10 μm^2
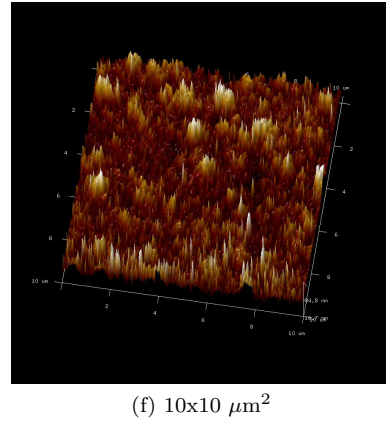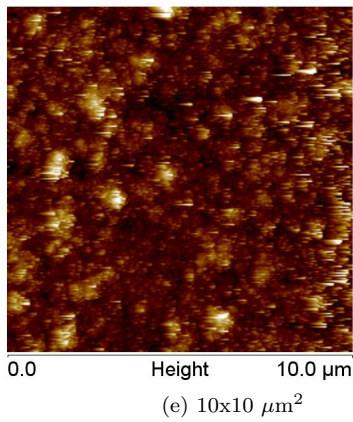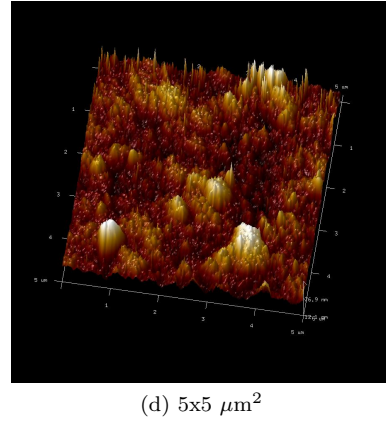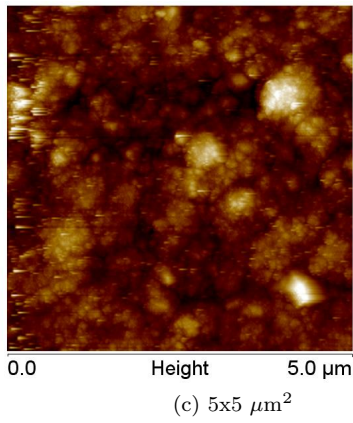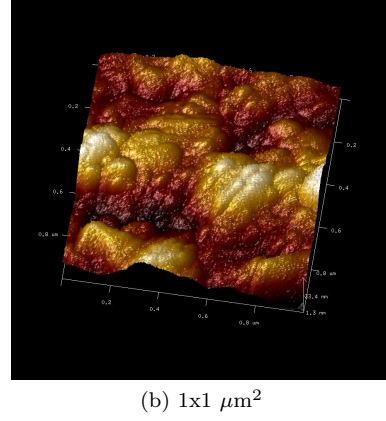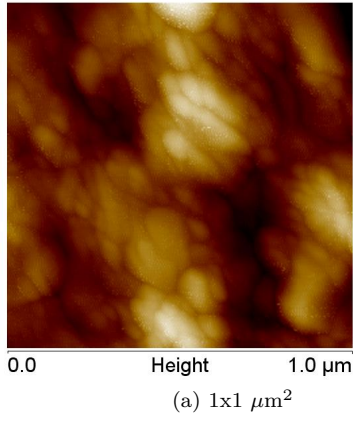
Figure A.5: 10 μm thick Pd23wt.%Ag (Sample A5). AFM images of the growth side in 2D (a, c, e, g) and in 3D modified images (b, d, f, h).

Sample B1
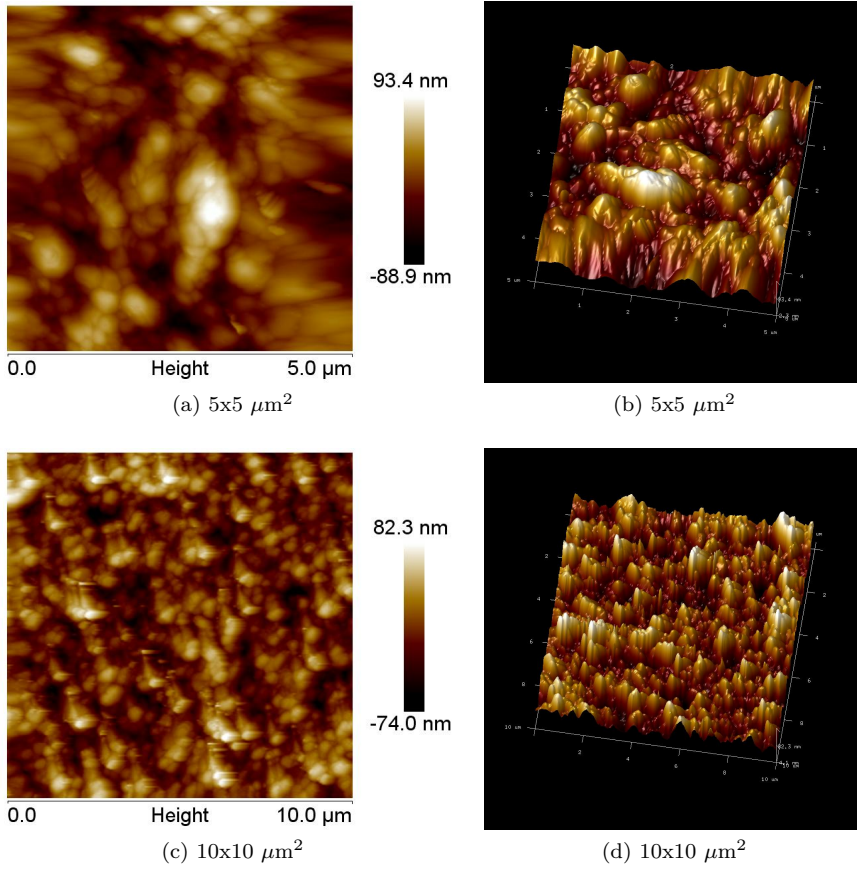
(a) 5x5 μm^2

(b) 5x5 μm^2

(c) 10x10 μm^2

(d) 10x10 μm^2

Figure A.6: 4 μm thick Pd23wt.%Ag after heat treatment in air. AFM images of the growth/feed side in 2D (a, c) and in 3D modified images (b, d).

Sample B2

(a) 5x5 μm^2

(b) 5x5 μm^2

(c) 10x10 μm^2

(d) 10x10 μm^2

Figure A.7: 8 μm thick Pd23wt.%Ag after heat treatment in air. AFM images of the growth/feed side in 2D (a, c) and in 3D modified images (b, d).

Sample C1

(a) 5x5 μm^2

(b) 5x5 μm^2

79.3 nm

-79.3 nm

Height

0.0   5.0 μm

(c) 10x10 μm^2

(d) 10x10 μm^2

104.6 nm

-86.8 nm

Height

0.0   10.0 μm

Figure A.8: 8 μm thick Pd23wt.%Ag after hydrogen stabilization. AFM images of the growth/feed side in 2D (a, c) and in 3D modified images (b, d).

Sample D1

(a) 5x5 μm^2

(b) 5x5 μm^2

(c) 10x10 μm^2

(d) 10x10 μm^2
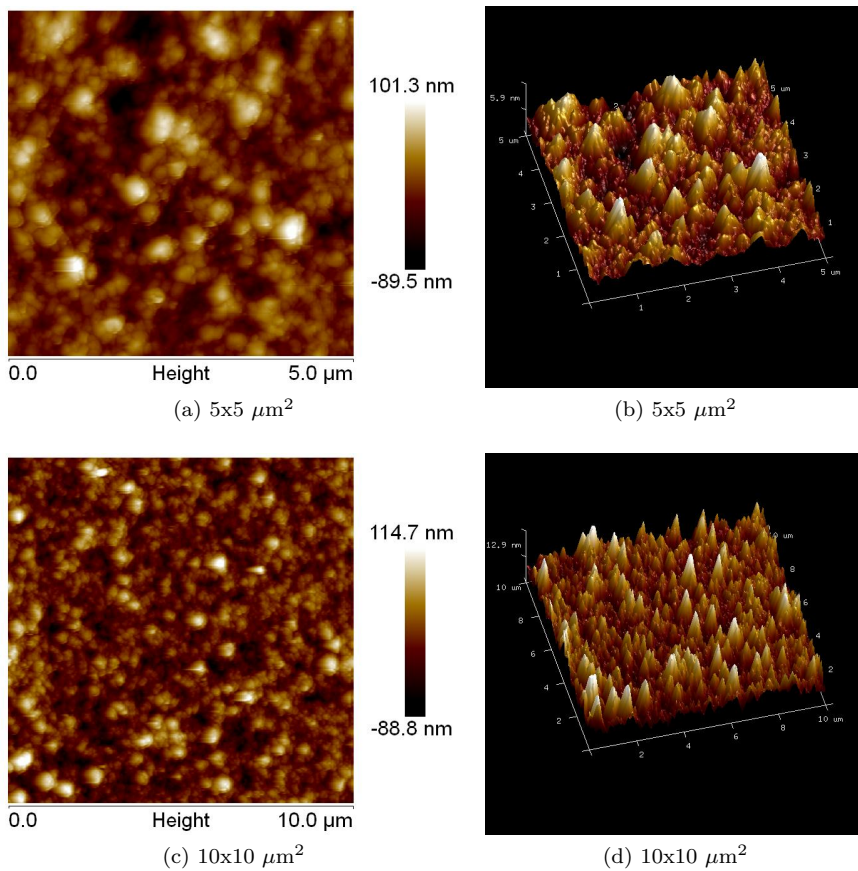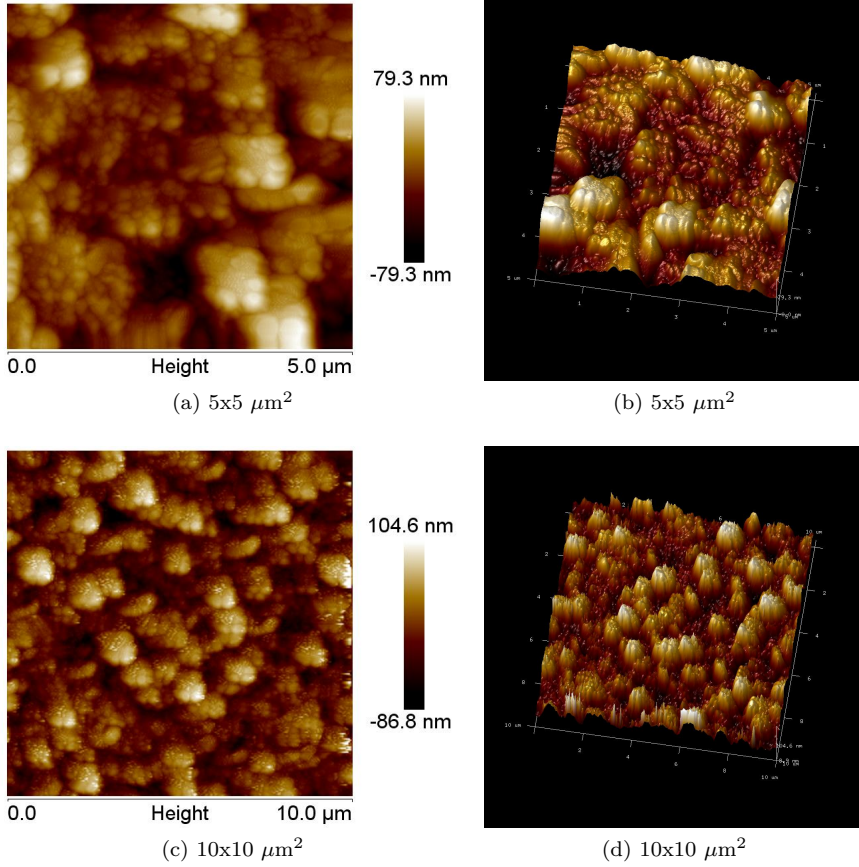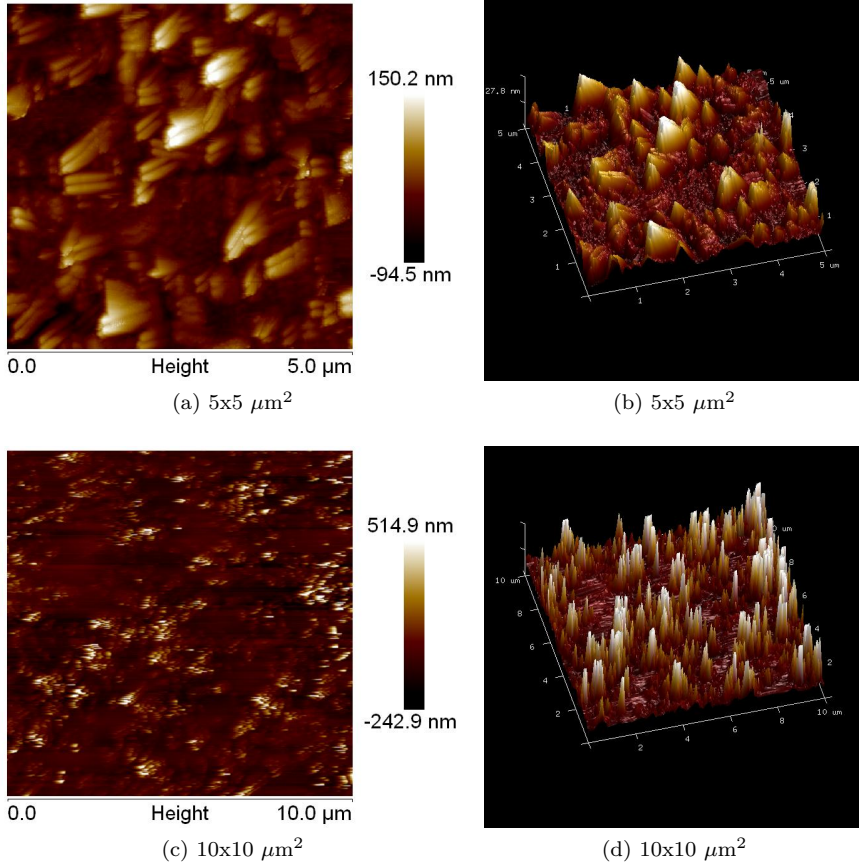
Figure A.9: $\sim$2 μm thick Pd/Au5at.%. AFM images of the growth side in 2D (a, c) and in 3D modified images (b, d).

A.1.2   Substrate/permeate side

Sample A1-A5

(a) 2.2 μm Pd23wt.%Ag (Sample A1). 1x1 μm^2
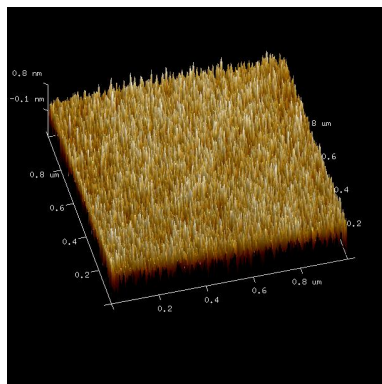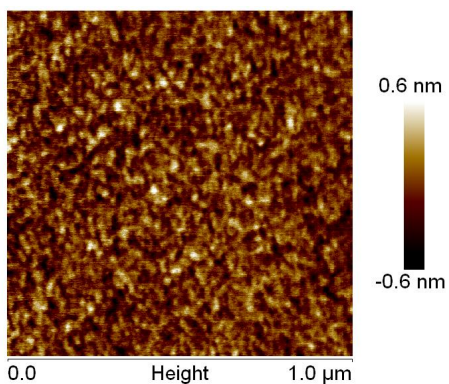
(b) 2.2 μm Pd23wt.%Ag (Sample A1). 1x1 μm^2

(c) 4 μm Pd23wt.%Ag (Sample A2). 1x1 μm^2
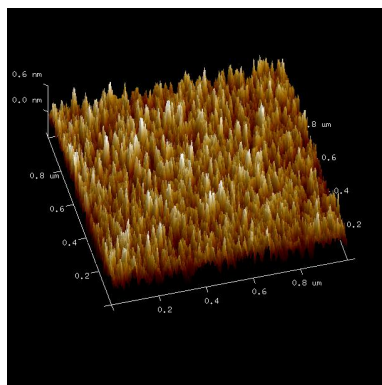
(d) 4 μm Pd23wt.%Ag (Sample A2). 1x1 μm^2
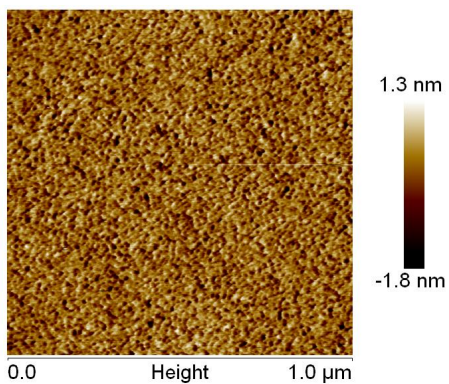
(e) 6 μm Pd23wt.%Ag (Sample A3). 1x1 μm^2
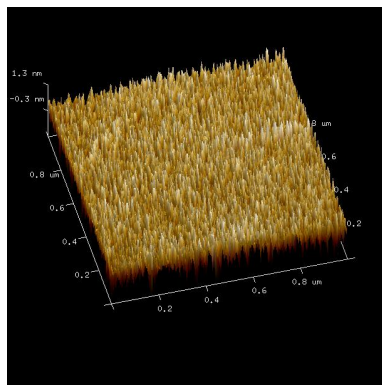
(f) 6 μm Pd23wt.%Ag (Sample A3). 1x1 μm^2
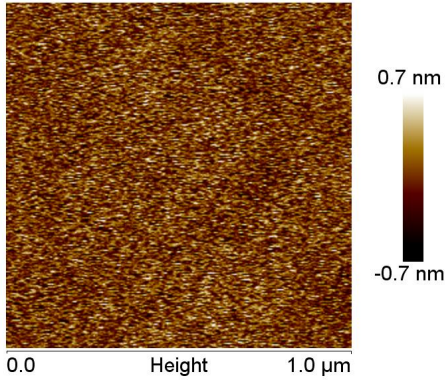
(g) 8 μm Pd23wt.%Ag (Sample A4). 1x1 μm^2
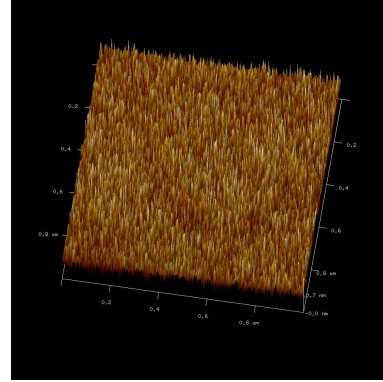
(h) 8 μm Pd23wt.%Ag (Sample A4). 1x1 μm^2
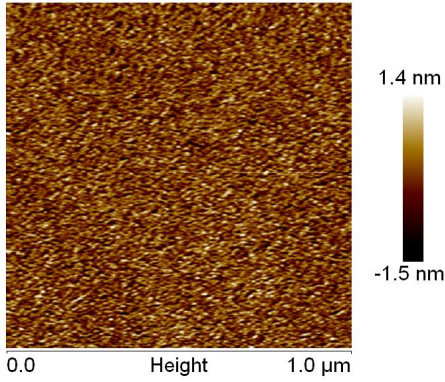
(i) 10 μm Pd23wt.%Ag (Sample A5). 1x1 μm^2
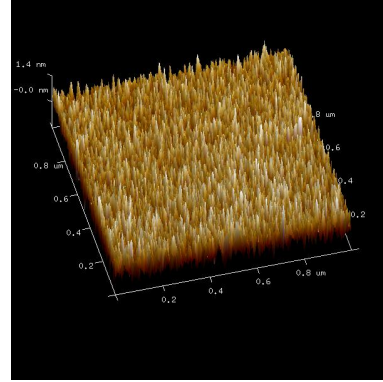
(j) 10 μm Pd23wt.%Ag (Sample A5). 1x1 μm^2

Figure A.9: Images of the substrate side of all PO-membranes of Pd23wt.%Ag. AFM images in 2D (a, c, e, g, i) and in 3D modified images (b, d, f, h, j).

Sample B1
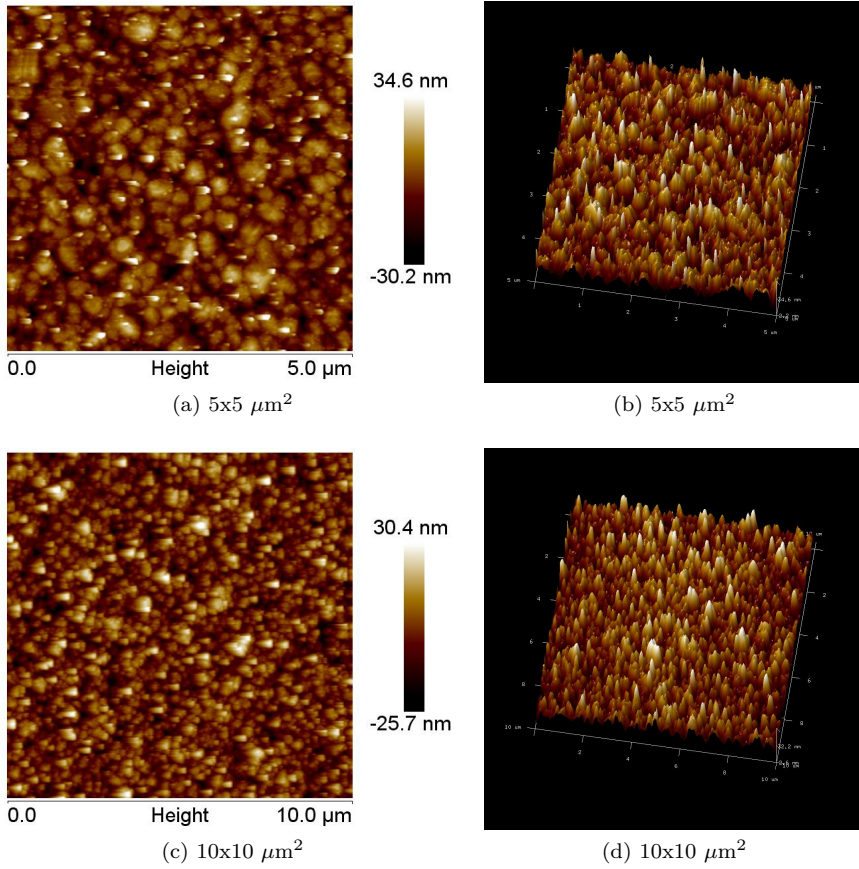
(a) 5x5 μm^2

(b) 5x5 μm^2

(c) 10x10 μm^2

(d) 10x10 μm^2

Figure A.10: 4 μm Pd23wt.%Ag after heat treatment in air. AFM images of the permeate/substrate side in 2D (a, c) and in 3D modified images (b, d).

Sample B2

(a) 5x5 μm^2

(b) 5x5 μm^2

(c) 10x10 μm^2

(d) 10x10 μm^2

Figure A.11: 8 μm Pd23wt.%Ag after heat treatment in air. AFM images of the permeate/substrate side in 2D (a, c) and in 3D modified images (b, d).

Sample C1

(a) 1x1 μm^2

(b) 1x1 μm^2

2.8 nm

-2.8 nm

0.0   Height   1.0 μm

(c) 5x5 μm^2

(d) 5x5 μm^2

3.1 nm

-3.3 nm

0.0   Height   5.2 μm
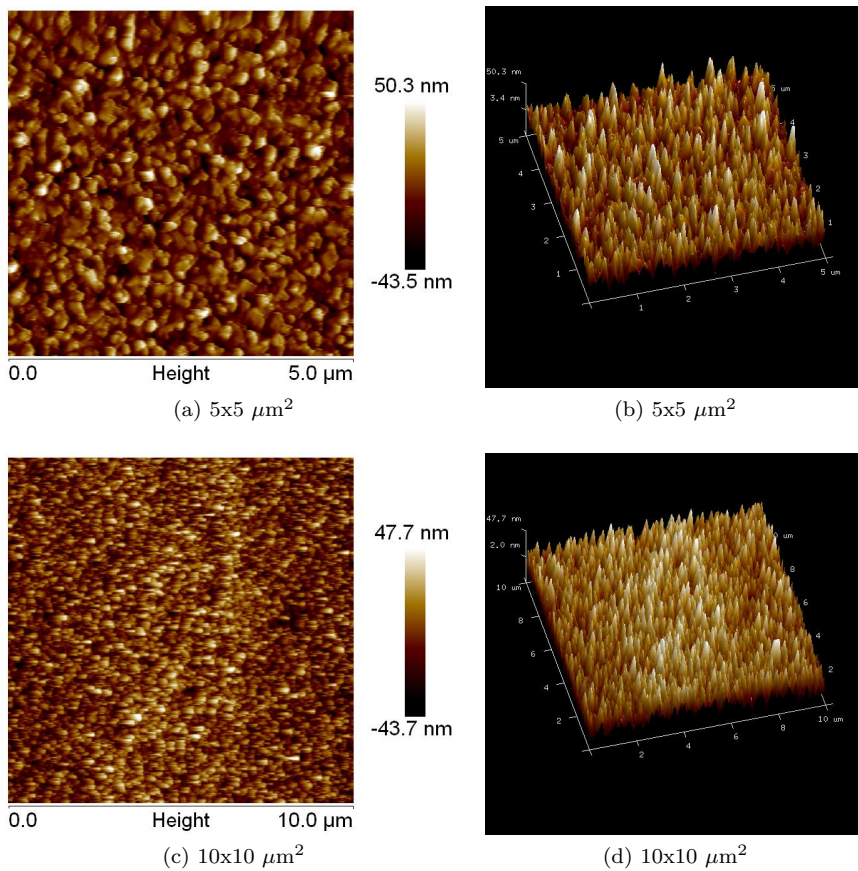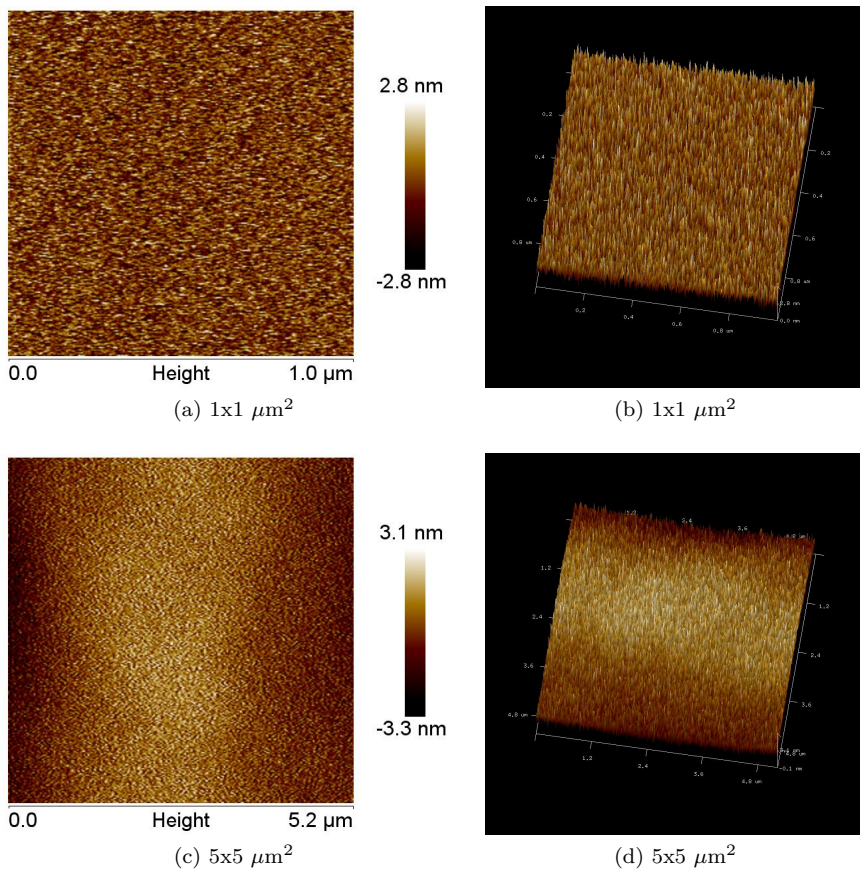
Figure A.12: 8 μm Pd23wt.%Ag after hydrogen stabilization. AFM images of the permeate/substrate side in 2D (a, c) and in 3D modified images (b, d). The 5x5 μm^2 area shows dark areas on each side. This reflects a bow on the sample. Using 2nd flattening order instead of 1st flattening order, would have eliminated this bow in addition to do centering and remove tilt. This was not performed since consistency in image treatment was desired. The convex bow is a natural result caused from the pressure on feed side. This bow is not detected in the 1x1 μm^2 area.

A.2 Particle analysis results

Sample	A1	A2	A3	A4	A5
Side	Growth	Growth	Growth	Growth	Growth
Mean density $(1/\mu m^2)$	4.21	2.36	2.80	1.76	0.90
Mean height (nm)	11.78	10.35	10.43	14.81	21.76
Mean area $(nm^2)x10^{-3}$	21.26	32.94	26.77	32.86	62.6
Mean diamenter (nm)	118.78	143.97	129.91	155.72	213.05
Sigma height (nm)	6.86	8.62	9.22	13.39	12.27
Sigma area $(nm^2)x10^{-3}$	68.31	73.82	77.41	81.24	139.45
Sigma diamenter (nm)	110.78	122.61	121.83	123.14	155.53

Table A.1: Results from the particle analysis command. The values displayed are the average of all measurements taken on the sample with area 5x5μm^2.

Sample	B1		B2		C1	D1
Side	Feed	Perm.	Feed	Perm.	Feed	Growth
Mean density $(1/\mu m^2)$	0.41	2.83	1.08	1.84	0.51	0.65
Mean height (nm)	24.01	18.49	20.52	25.96	18.26	25.70
Mean area $(nm^2)x10^{-3}$	231.71	21.26	69.09	43.94	125.93	37.96
Mean diamenter (nm)	410.57	265.54	210.68	185.80	311.79	170.13
Sigma height (nm)	20.41	10.15	18.41	12.53	13.76	18.64
Sigma area $(nm^2)x10^{-3}$	350.16	156.09	150.59	87.89	181.99	69.39
Sigma diamenter (nm)	332.56	181.58	195.08	132.86	220.73	130.76

Table A.2: Results from the particle analysis command. The values displayed are the average of all measurements taken on the sample with area 5x5μm^2.

Appendix B

Microchannel membrane setup

list 66-16-U-20 030904.jpg

66-16-U-20 SYMBOL LIST
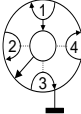
hoke valve	
three-way valve	condensing tank
needle valve	flow indicator (rotameter)
reduction valve	
one-way valve	
relief valve	heated lines (heating tape) with thermocoule
pressure indicator	Voltron effect regulator
gas drier	
oxy-trap	nafion dryer
particle filter	
mass flow controller	micro heat exchanger
liquid flow controller with **S**ensor and **V**alve	T or micro mixer
pressure controller (< 8 bar)	dP-cell

evaporator

oven

4-port valve

Eurotherm

Figure B.1: Symbol list of membrane reactor setup.

94
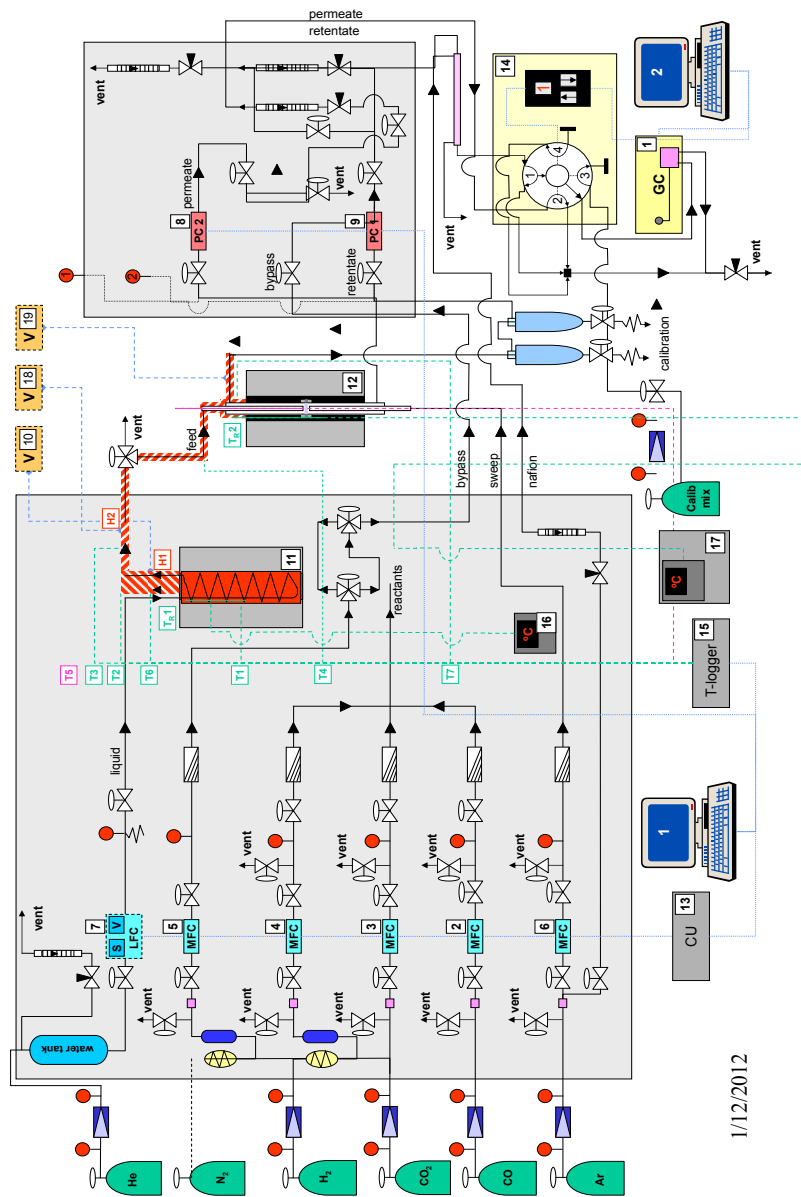
Figure B.2: Schematic presentation of the membrane reactor setup.

Appendix C

Permeation measurement results

C.1   8 μm Pd/Ag23wt.% before and after HTA
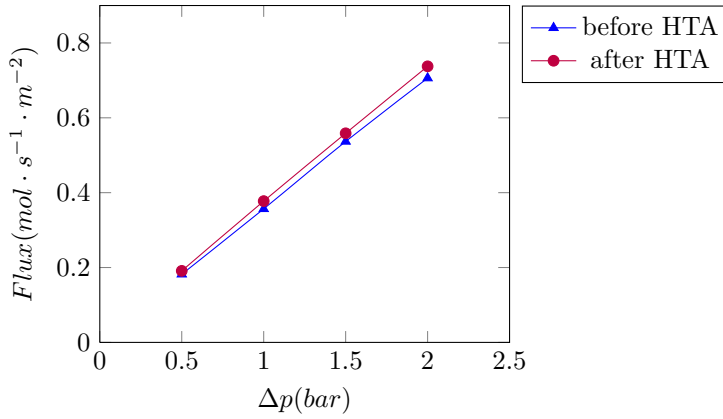
Figure C.1: Results for 8 μm Pd/Ag23wt.% membrane at 300 °C.
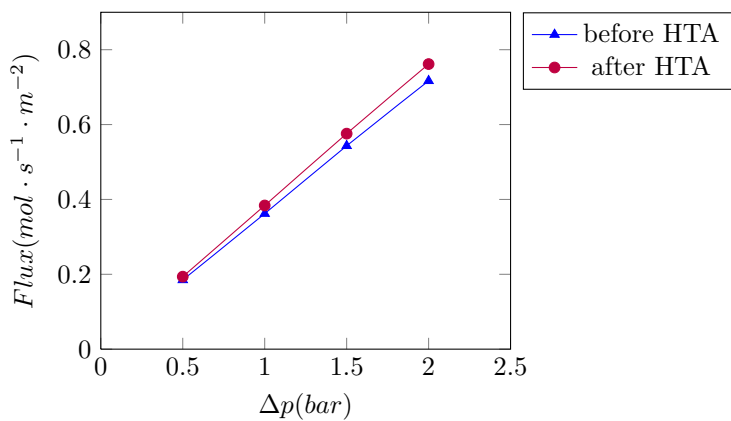
Figure C.2: Results for 8 μm Pd/Ag23wt.% membrane at 350 °C.
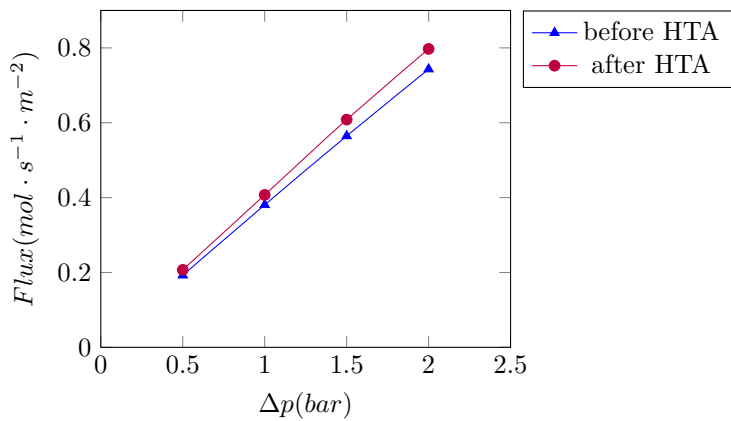
Figure C.3: Results for 8 μm Pd/Ag23wt.% membrane at 400 °C.

C.2   8 μm Pd/Ag23wt.% after HS
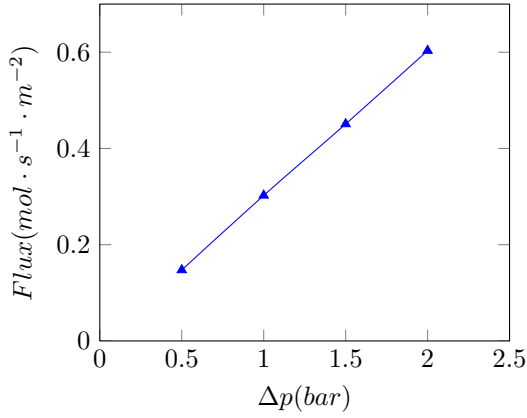
Figure C.4: Results for 8 μm Pd/Ag23wt.% membrane at 300 °C after hydrogen stabilization.
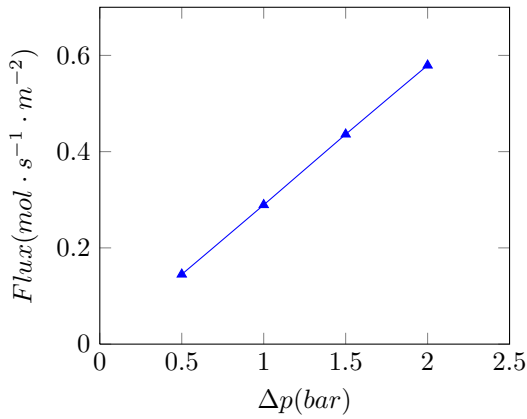
Figure C.5: Results for 8 μm Pd/Ag23wt.% membrane at 350 °C after hydrogen stabilization.
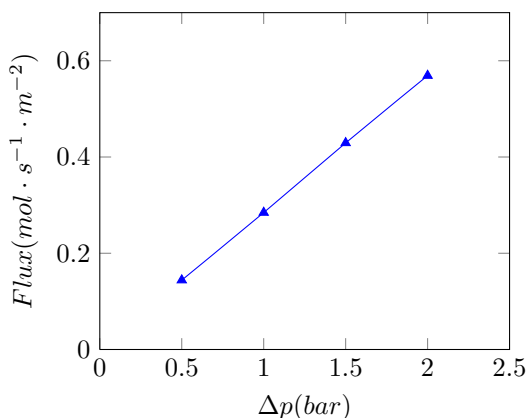
Figure C.6: Results for 8 μm Pd/Ag23wt.% membrane at 400 °C after hydrogen stabilization.

C.3   10 μm Pd/Ag23wt.% before and after HTA

After permeation measurements on the 10 μm thick membrane, it was discovered a leakage in the system. Therefore the presented values for permeance is not reliable. A higher flux is expected since the leakage was found at retentate side. The leakage on this side lead to a lower feed flow than the intentional flow of 100 ml/min. Even though the effect of heat treatment is detected, the alteration in flux increase can not be trusted since it is unknown when this leakage occurred. A surface topography investigation was not performed on this membrane after HTA, so the permeation results cannot be related to surface structure. Since the results are uncertain and surface topographic results are missing, it will not be discussed any further. Still, the permeation results are included to support the theory of permeation improvement as an effect of heat treatment in air.
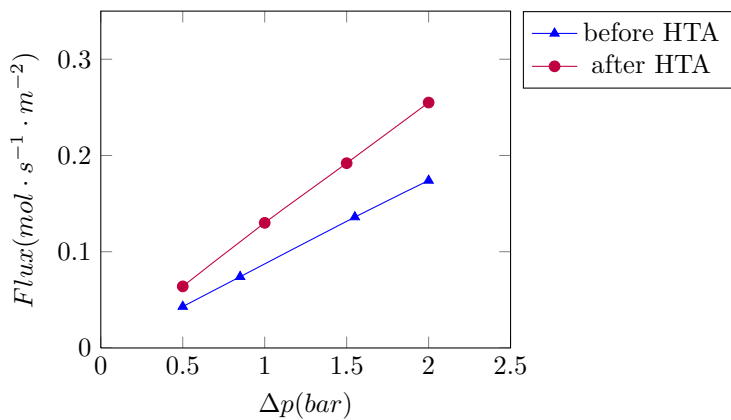
Figure C.7: Results for 10 μm thick Pd/Ag23wt.% membrane at 300 °C.
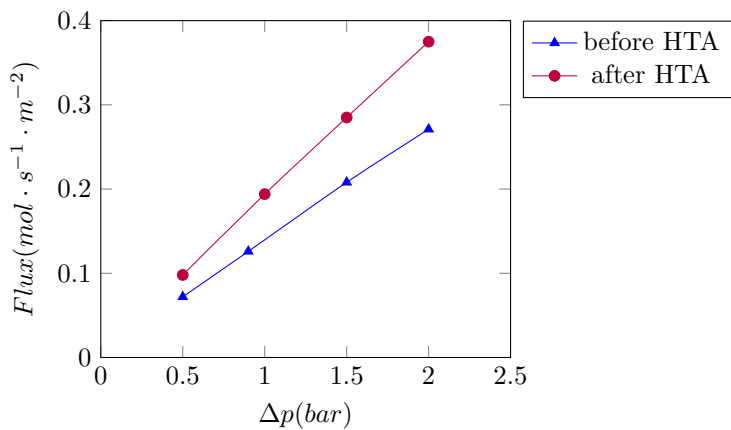
Figure C.8: Results for 10 μm thick Pd/Ag23wt.% membrane at 350 °C.
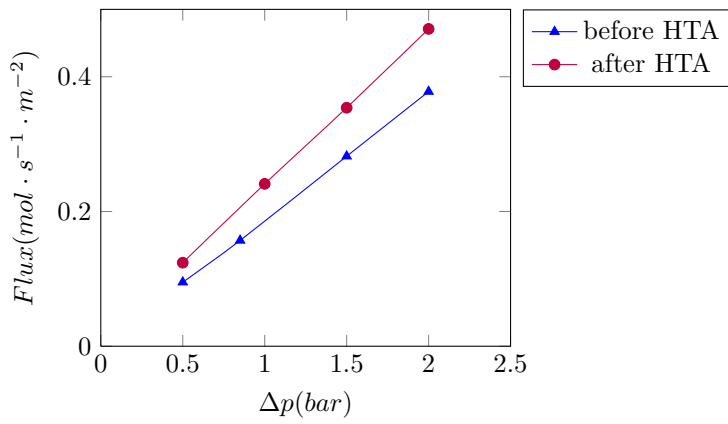
Figure C.9: Results for 10 μm thick Pd/Ag23wt.% membrane at $400\,^{\circ}$C.

Appendix D

Isotherm sorption results

D.1 Isotherm result for 2.2μm Pd/Ag23wt.% (Sample A1)
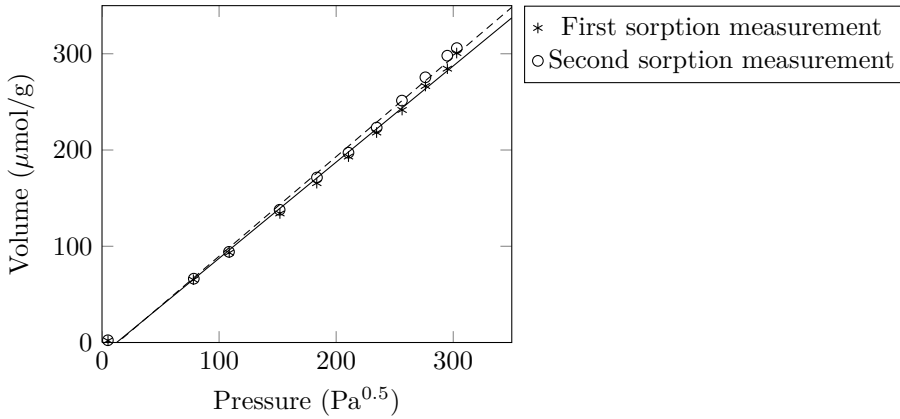
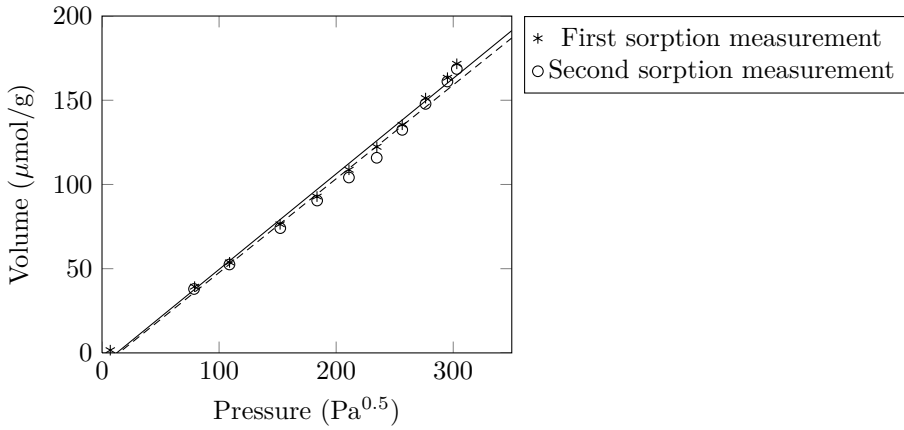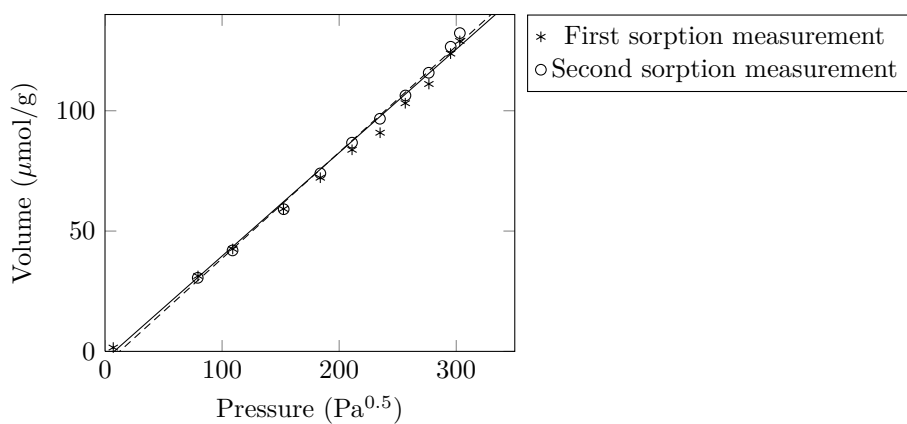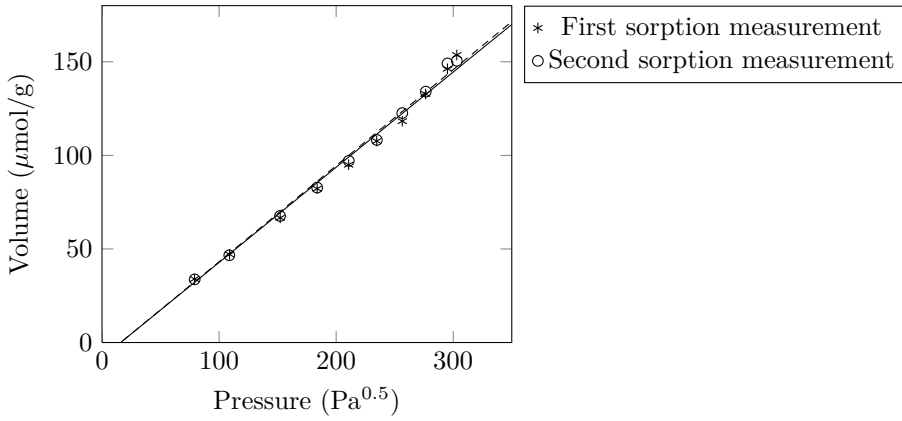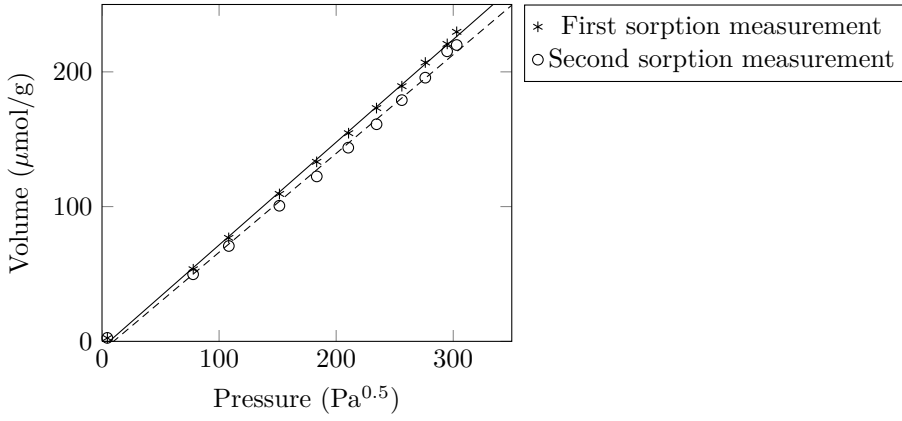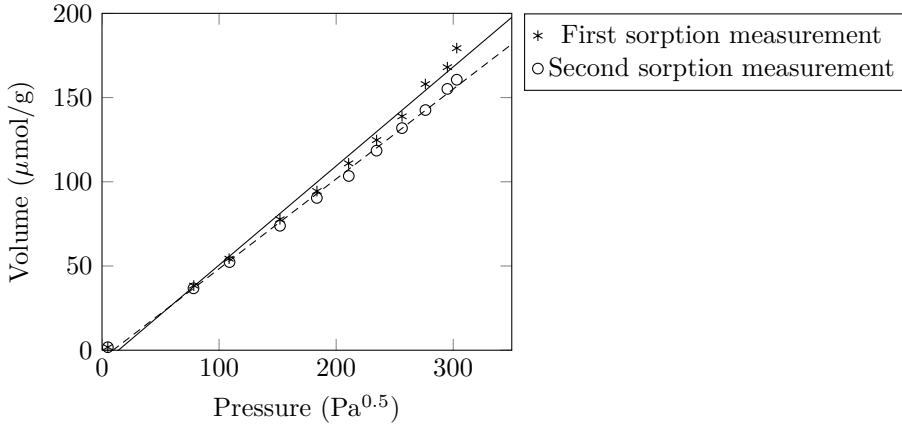Figure D.1: Isotherm result for 2.2μm Pd/Ag23wt.% (Sample A1) at 300 °C.
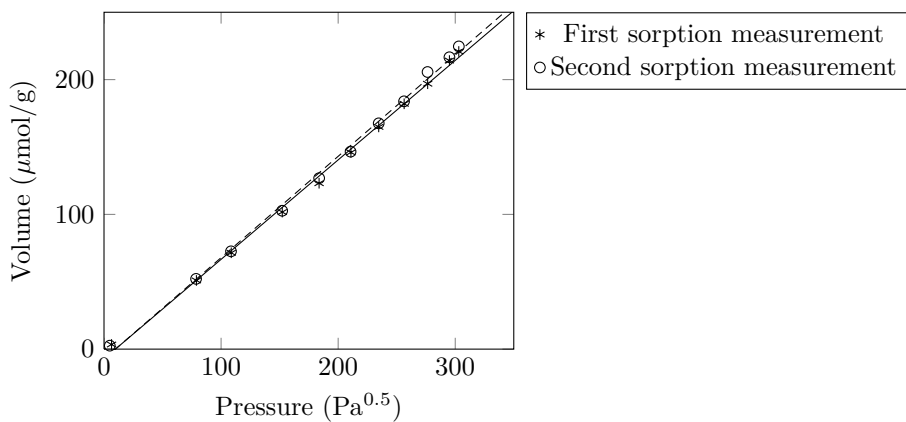
Figure D.2: Isotherm result for 2.2μm Pd/Ag23wt.% (Sample A1) at 350 °C.
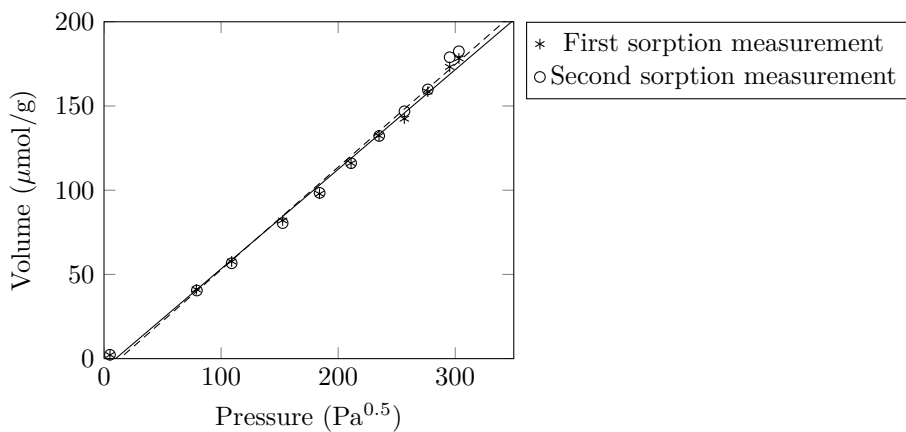
Figure D.3: Isotherm result for 2.2μm Pd/Ag23wt.% (Sample A1) at 400 °C.

D.2 Isotherm result for 4μm Pd/Ag23wt.% (Sample A2)
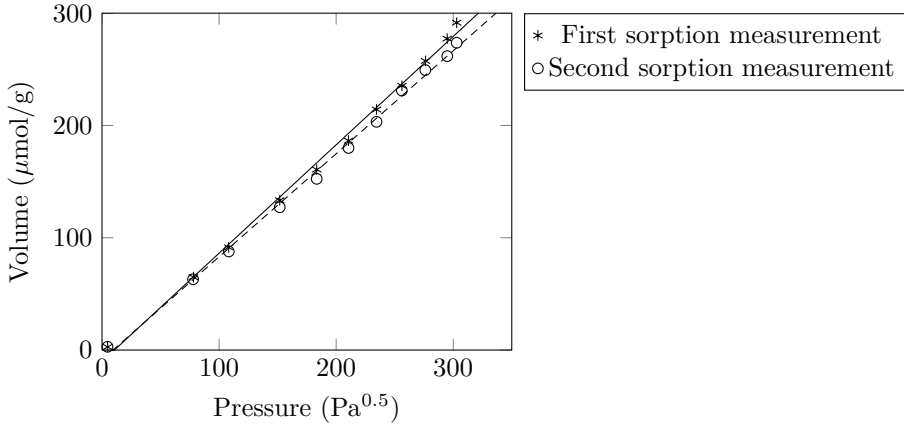
Figure D.4: Isotherm result for 4μm Pd/Ag23wt.% (Sample A2) at 300 °C.
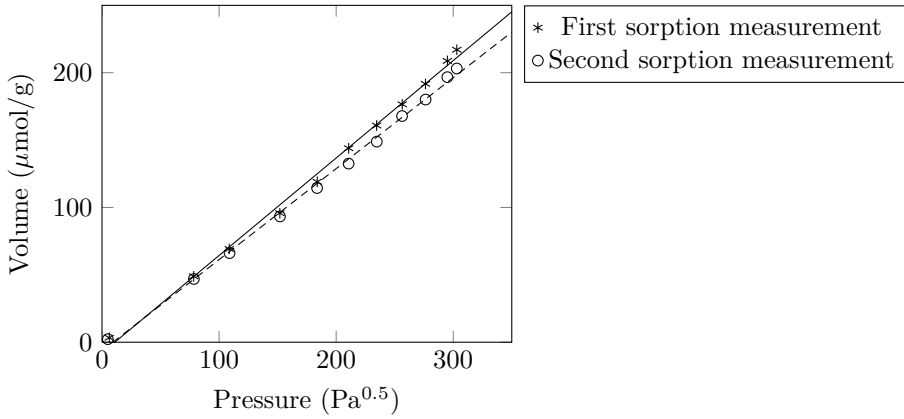
Figure D.5: Isotherm result for 4μm Pd/Ag23wt.% (Sample A2) at 350 °C.
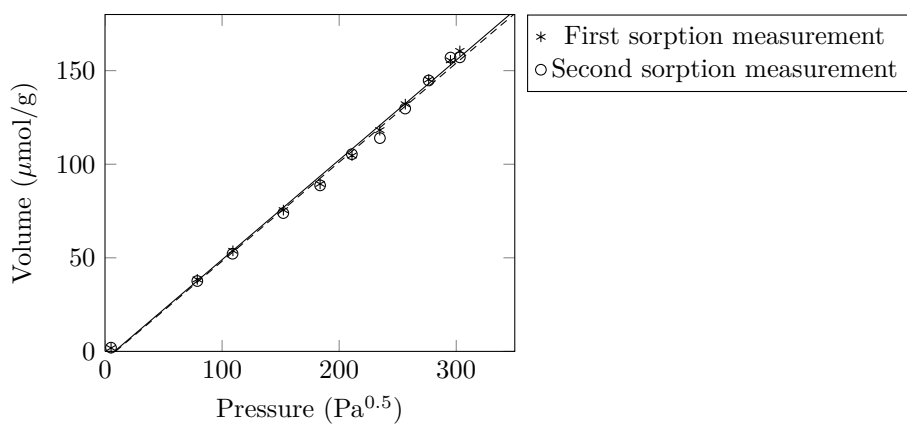
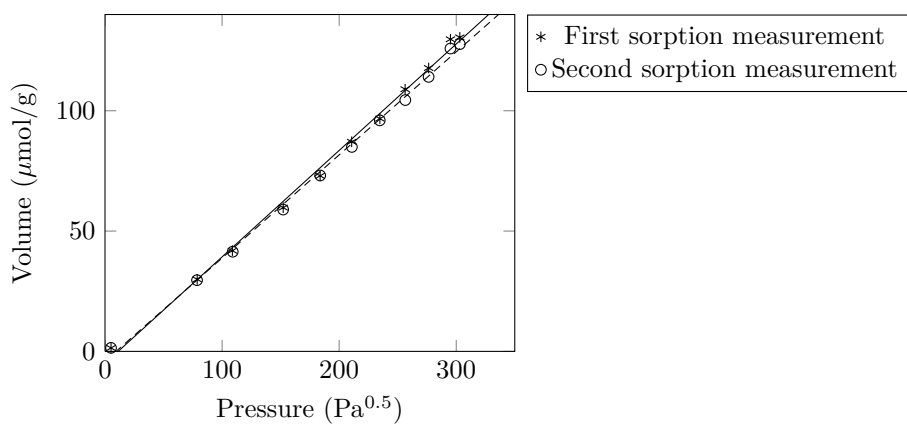Figure D.6: Isotherm result for 4μm Pd/Ag23wt.% (Sample A2) at 400 °C.

D.3 Isotherm result for 6µm Pd/Ag23wt.% (Sample A3)
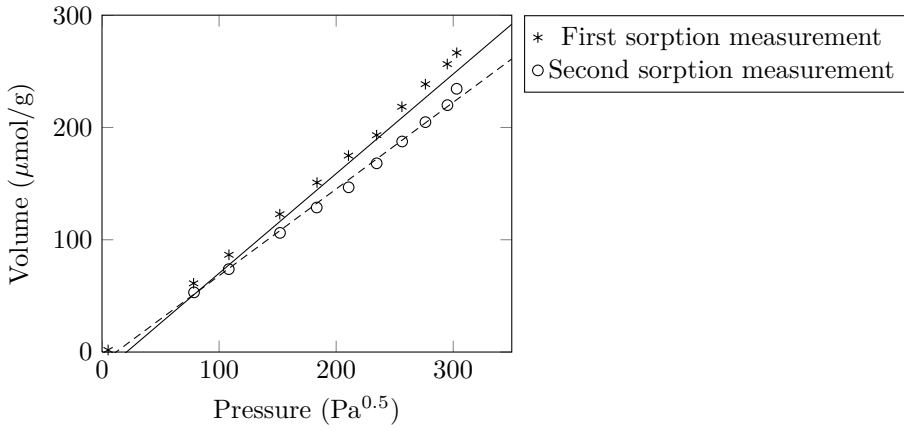
Figure D.7: Isotherm result for 6µm Pd/Ag23wt.% (Sample A3) at 300 °C.

Figure D.8: Isotherm result for 6µm Pd/Ag23wt.% (Sample A3) at 350 °C.

Figure D.9: Isotherm result for 6μm Pd/Ag23wt.% (Sample A3) at 400 °C.

D.4 Isotherm result for 8μm Pd/Ag23wt.% (Sample A4)
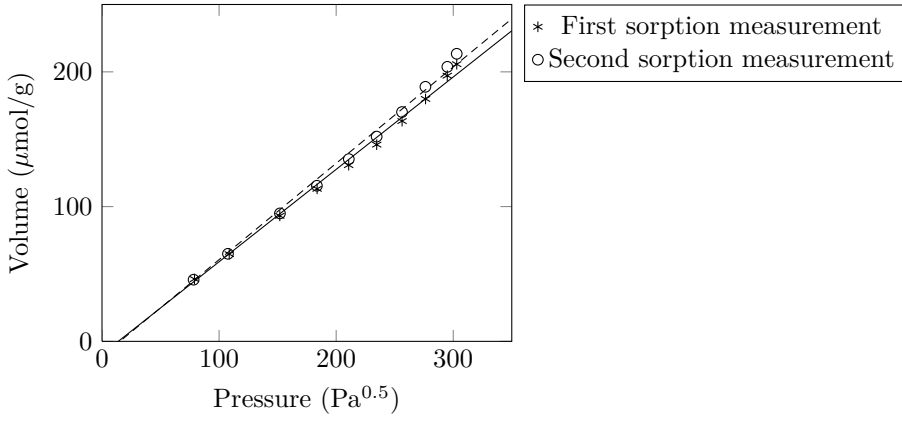
Figure D.10: Isotherm result for 8μm Pd/Ag23wt.% (Sample A4) at $300\,^{\circ}$C.

Figure D.11: Isotherm result for 8μm Pd/Ag23wt.% (Sample A4) at $350\,^{\circ}$C.
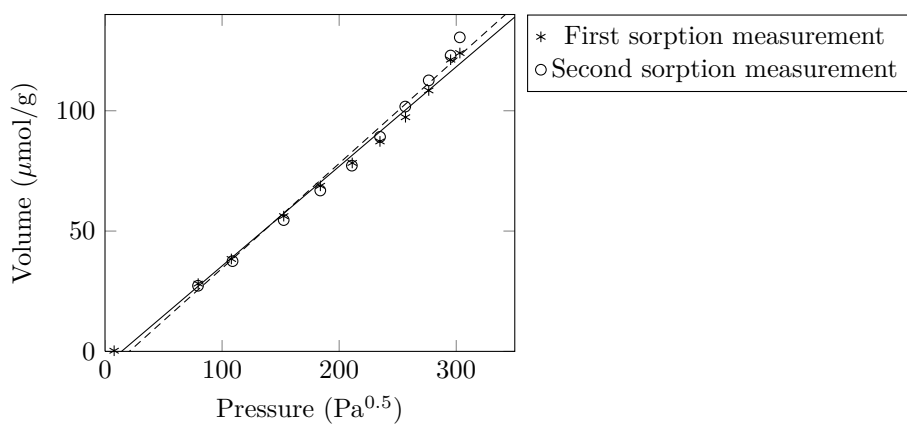
Figure D.12: Isotherm result for 8μm Pd/Ag23wt.% (Sample A4) at $400\,^{\circ}$C.

D.5 Isotherm result for 10μm Pd/Ag23wt.% (Sample A5)

Figure D.13: Isotherm result for 10μm Pd/Ag23wt.% (Sample A5) at $300\,^{\circ}$C.

Figure D.14: Isotherm result for 10μm Pd/Ag23wt.% (Sample A5) at $350\,^{\circ}$C.

Figure D.15: Isotherm result for 10μm Pd/Ag23wt.% (Sample A5) at 400 °C.

D.6 Isotherm result for ∼2 μm Pd/Au5at.% (Sample D1)
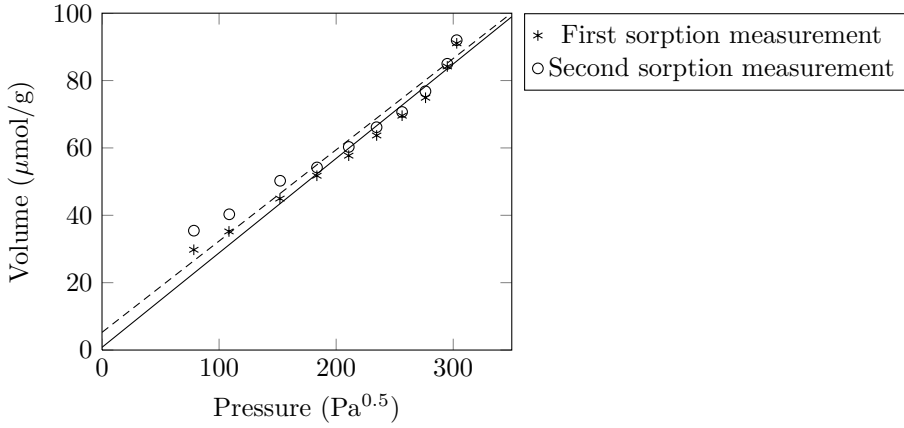
Figure D.16: Isotherm result for∼2 μm Pd/Au5at.% (Sample D1) at 300 °C.
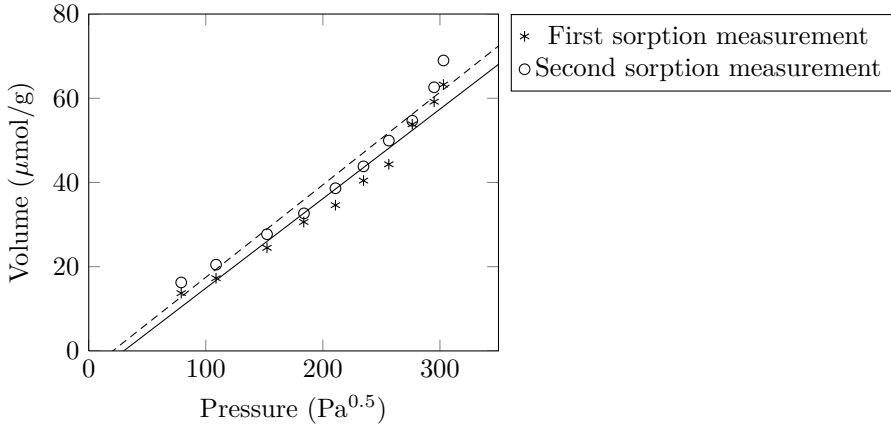
Figure D.17: Isotherm result for ∼2 μm Pd/Au5at.% (Sample D1) at 350 °C.
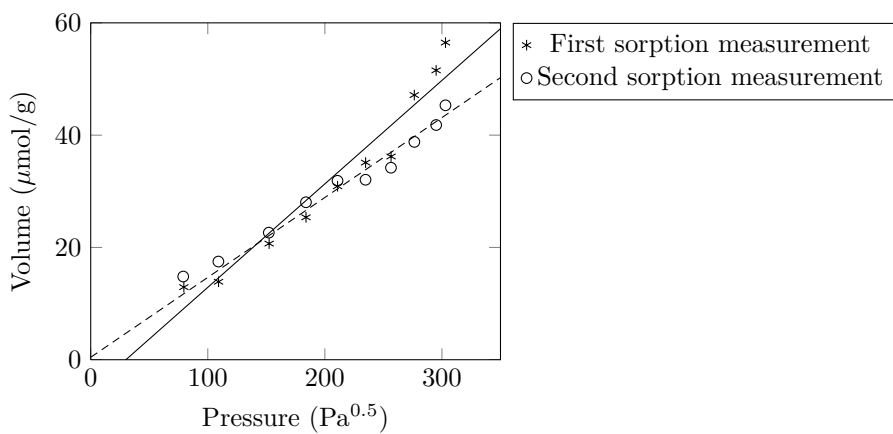
Figure D.18: Isotherm result for $\sim$2 μm Pd/Au5at.% (Sample D1) at 400 °C.

D.7 Isotherm result for ~2 μm Pd/Y5at.% (Sample D2)
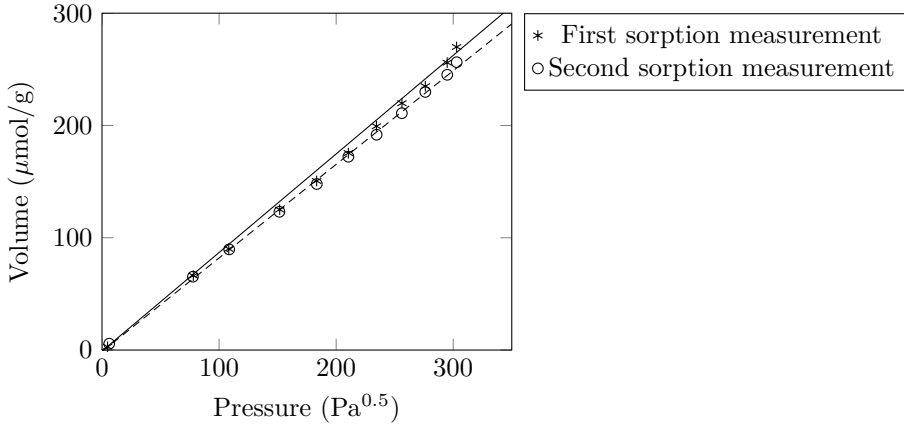
Figure D.19: Isotherm result for~2 μm Pd/Y5at.% (Sample D2) at 300 °C.
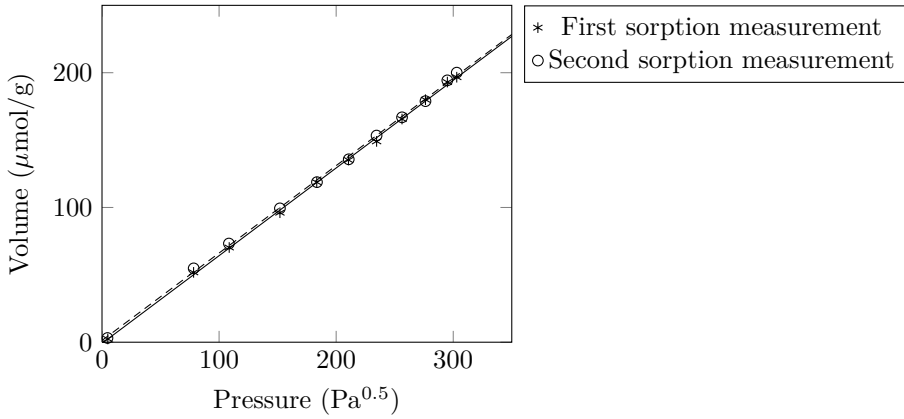
Figure D.20: Isotherm result for ~2 μm Pd/Y5at.% (Sample D2) at 350 °C.
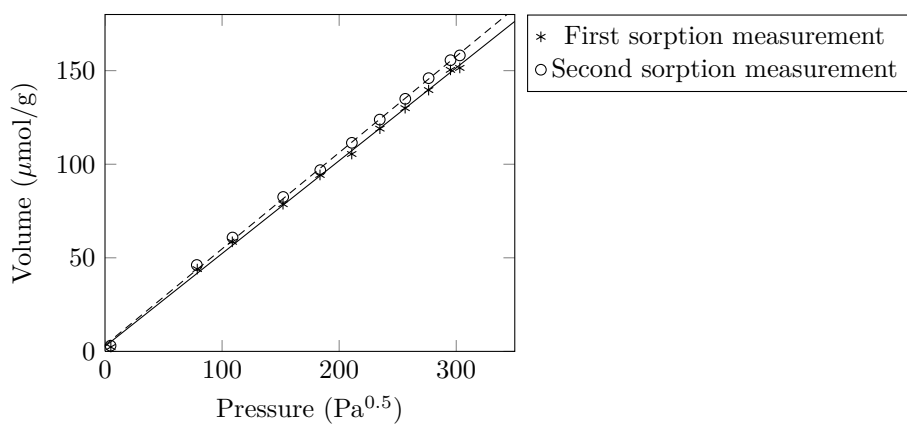
Figure D.21: Isotherm result for $\sim$2 μm Pd/Y5at.% (Sample D2) at 400 °C.